LOCAL CHARACTERIZATION OF RESISTANCE SWITCHING PHENOMENA IN TRANSITION METAL OXIDES

A Dissertation

by

HEIDI ANYA CLARKE

Submitted to the Office of Graduate and Professional Studies of
Texas A&M University
in partial fulfillment of the requirements for the degree of

DOCTOR OF PHILOSOPHY

Chair of Committee,	Patrick J. Shamberger
Committee Members,	Sarbajit Banerjee
	Miladin Radovic
	Christi Madsen
Head of Department,	Ibrahim Karaman

May 2019

Major Subject: Materials Science and Engineering

ABSTRACT

The development of neuromorphic computing systems that emulate the analog charge states and plasticity of the brain's neuron-synapse architecture has been a major driver of resistance switching materials exploration. Materials that demonstrate changes in conductance with tunable ratios and volatility of resistance states within a single layer are highly desirable. Although excellent resistance switching device performance has been demonstrated in a range of transition metal oxides, a lack of understanding of the fundamental microscale evolution of a material during resistance switching presents a key limitation to controlling switching parameters. Here, we examine the role of materials defects on local resistance switching structures in two representative transition metal oxide materials: HfO_2 thin films and hydrothermally synthesized VO_2 single crystals. In each material, we seek to clarify the structure of resistance switching domains and the kinetics of domain formation resulting from intentional defect introduction.

This thesis is therefore divided into two main parts concerning (1) the introduction of planar defects in HfO_2 filamentary resistance switching devices, and (2) the impact of introduction of point defects on the metal-insulator transition in VO_2 single crystals. Part I (Sections 2 – 3) details investigation of Cu ion migration rates in Cu/HfO_2/p+Si and Cu/HfO_2/TiN devices in which oxide microstructure varies between amorphous, polycrystalline, and oriented polycrystalline. Ion migration across the oxide layer is shown to be rate limiting and faster in polycrystalline layers than in amorphous HfO_2 layers at equivalent electric field. Moreover, the 3D shape of conductive filaments is investigated by a scribing atomic force microscopy experiment in Cu/HfO_2/p+Si devices and reveals a broad range of filament shapes under identical electrical stress conditions. Thermal dissipation is interpreted as the principal determinant of filament area, while oxide

microstructure is shown to direct the location of filaments within the device. In part II (Sections 4 – 5), the hysteresis of the metal-insulator transition (switching volatility) in VO_2 is shown to intrinsically derive from nucleation limited transformations in individual particles. Here, hysteresis is a strong function of particle size, but may be increased or decreased by synthesis techniques that affect the concentration and potency of intrinsic point defects. Upon chemical doping with boron at interstitial lattice sites, a unique kinetic effect on the hysteresis of the current driven metal-insulator transition in two terminal B_xVO_2 devices is observed. Dependence of the critical switching current on thermal relaxation time and temperature is characterized and recommendations for further kinetic testing are made. Finally, a few experimental extensions of the work presented in this thesis are made in Section 6.

DEDICATION

To Marnie

ACKNOWLEDGEMENTS

I would like to acknowledge my advisor Dr. Patrick Shamberger for his continual support and encouragement during research efforts and during the writing of this thesis. His integrity, commitment to high quality research, as well as interest in the development of analytical skills in his students has provided an excellent model towards which to strive. I would also like to thank Dr. Banerjee for extensive collaboration with his group on the work in the VO_2 system, as well as the rest of my committee, Dr. Radovic and Dr. Madsen, for their time in evaluating this thesis.

Many of my peers also helped me develop the experiments and analyses presented in this thesis and I would like to acknowledge them for their contributions. The lion's share of those thanks belong to Tim Brown. His clarity of thought and absolute joy in talking through mathematical theory was a critical source of aid when I needed someone with whom to talk through ideas. I'd also like to thank the other members of my lab group for their excellent company and time: Yijia Zhang, Adelaide Bradicich, Aliya Yano, Alison Hoe, and Michael Deckard. There were also several excellent undergraduate students contributing to the work presented in this thesis including Joseph Anderson, Laura Deremo, Bill Caraway, and Sarah Hammock. Finally, I'd like to thank the staff of Aggiefab and the MCF for their expertise, training, and help during device fabrication and materials characterization.

The pursuit of this degree would not in any way have been possible without the support and sacrifice of my family and there aren't words for how much I appreciate them.

CONTRIBUTORS AND FUNDING SOURCES

Contributors

This work was supervised by a dissertation committee consisting of Dr. Patrick Shamberger (chair), Dr. Sarbajit Banerjee, and Dr. Miladin Radovic of the Department of Materials Science and Engineering and Dr. Christi Madsen of the Department of Electrical Engineering.

Thin film deposition of 30 nm HfO_2 on p+Si and TiN substrates accompanied by powder x-ray crystallographic characterization and atomic force microscopy characterization was completed by Tim Brown in conjunction with Dr. Amber Reed at the Air Force Research Laboratories, Wright Patterson Air Force Base, OH. These data are analyzed and discussed in Section 1. High resolution transmission electron microscopy images of HfO_2 deposited on SiO_2/Si substrates was completed by Dr. JianJun Hu at AFRL and interpreted in Section 1. Data analyses of 2D conductive atomic force microscopy by alignment in Section 2 was accomplished with the aid of Joseph Anderson and Laura Deremo. A portion of tested device data was collected by Joseph Anderson, Laura Deremo, and Sarah Hammock. Syntheses and doping of VO_2 particles along with powder x-ray diffraction and some differential scanning calorimetry data were carried out in collaboration with Dr. Sarbajit Banerjee's lab by Erick J. Braham, Theodore Alivio, and Diane G. Sellers. Optical imaging and counting statistics of undoped VO_2 transitions explored in Section 4 was carried out with the assistance of Bill Caraway. All other work conducted for the dissertation was completed by the student independently.

Funding Sources

Graduate study was supported by a graduate research assistantship from Texas A&M University. This work was made possible in part by AFOSR LRIR 14RX13COR. Its contents are solely the responsibility of the authors and do not necessarily represent the official views of the Air Force Office of Scientific Research.

TABLE OF CONTENTS

Page

LIST OF FIGURES

Page

LIST OF TABLES

Page

1. INTRODUCTION AND LITERATURE REVIEW

1.1 Overview

Exploration of non-volatile resistance switching memories has a rich history of investigation, dating back to the 1960's and even earlier. The materials that exhibit resistance switching do so by a wide variety of mechanisms ranging from phase changes in correlated-electron oxides to mechanically actuated nano-gap switches [1]. Among the many candidates for exploration, transition metal oxides represent systems in which both technologically promising devices have been fabricated and systems which offer a space to answer the quintessential materials science questions of how introduction of defects (e.g., grain boundaries in polycrystalline thin films, point defects and defect clusters in doped oxides) change macroscopic conductance properties. In particular, this thesis addresses two very different resistance switching phenomena and examines the potential in each for using a variety of characterization techniques to determine relevant conductive or insulating domain shapes, the kinetics of how those domain shapes are formed, and the impact of extended defects (grain-boundaries) or point defects (dopants) in altering both domain shape and resistance switching kinetics. Finally, device fabrication and electrical characterization is used to relate intentional alterations of microscopic properties of the oxide material to changes in pertinent resistance switching characteristics (on/off states and driving voltages).

The central premise of this thesis is that *knowledge of the microscale evolution of a material is necessary to fully understand resistance switching phenomena*. We demonstrate this premise using the following two model systems:

(1) In two-terminal programmable metallization cells (PMCs), application of high electric fields drive arrested dielectric breakdown, in which ions from the device redox-active electrode are driven across the oxide layer to form a conductive filament. This conductive filament shorts the device to create a low resistance ON state. Application of voltage then drives current through the filament, which causes joule-heating and diffusion of ions away from the filament ("breaking the filament") returning the device to high resistance OFF state. Here, we study resistance switching in metal-insulator-metal devices based on a HfO_2 switching layer with a reactive Cu electrode. The size/shape of the filament within the oxide matrix is relatively unknown, but is of paramount importance in directing thermal and electric fields to determine subsequent switching voltages. Moreover, while many study the impacts of electrode geometry and roughness [2, 3], the opportunity to control filament size/shape may stem instead from the impact of HfO_2 microstructure on Cu ion migration kinetics. Therefore, the major topic of investigation in this system concerns the impact of oxide microstructure on filament forming kinetics, filament size, and filament shape.

(2) Resistance switching also occurs as a result of phase transitions in electron-correlated oxides, with the metal-insulator-transition (MIT) in VO_2 near 67 ^oC being the iconic material in this class[4]. This material undergoes a several order of magnitude change in resistance across its phase transition between the low temperature monoclinic (M1) phase to a high temperature rutile (R) phase. Doping of VO_2 with several isovalent and aliovant species has been demonstrated, and the impacts on transition temperature, hysteresis width, and phase coexistence well noted. However, the direct mechanisms by which dopant incorporation would lead to explicit control over these technologically important parameters are lacking, and are the subject of these investigations. Specifically, doping of hydrothermally synthesized VO_2 particles with W and B dopants has shown

depression of the transition temperature [5, 6] and most interestingly, kinetic hysteresis effects (some based on past cycling history) during thermal differential scanning calorimetry (DSC) characterization of bulk powders [7]. Extended metallic and insulating phase-coexistance regime under TEM is also observed in $W_xV_{1-x}O_2$ particles [8]. Although strong evidence points to varying nucleation mediated origins for hysteresis in these doped particles, confirmation of these effects on a single particle basis is required to separate the variety of distributions in particle size, defect concentration, and hysteresis-loop behavior inherently sampled in bulk powders, solidifying support for proposed nucleation based models. Additionally, the scaling of VO_2 volumes to sub-micron length scales is shown to strongly impact nucleation-based thermal hysteresis[9], and should be de-convoluted from dopant incorporation effects. Lastly, in an effort to connect understanding of microscopic origins of hysteresis in doped VO_2 particles to macroscopic resistance switching behavior, a set of lateral two terminal Au/Ni/B_xVO_2/Ni/Au switches will be fabricated and electrically characterized.

The results of these studies are expected to provide direct-microscopic characterization of metallic or insulating domains, and therefore insight into the microscopic mechanisms that control resistance switching in filamentary resistance switching in HfO_2 based devices, as well as in VO_2 single crystal particles and devices. The structure of this thesis is as follows:

Section 1 gives a detailed background of the pertinent resistance switching mechanisms in each HfO_2 devices and VO_2, as well as including a review on the literature on which the following work is based.

Section 2 details the study of the impact of oxide microstructure on conductive filament formation in Cu/HfO_2/p+Si and Cu/HfO_2/TiN devices. With the goal of reducing device variability between cycles and between devices, previous experiments on PMC devices utilize a variety of

metal oxide layers materials and focus on switching in amorphous layers or single crystalline layers, which may not necessarily offer superior switching characteristics [10]. Here, devices are fabricated on a suite of HfO_2 films which range from amorphous to textured polycrystalline, and the time to which breakdown is achieved under constant voltage bias is used as an indication of Cu ion migration rates. Results show that, regardless of bias polarity or electrode metal, filament formation times are at least one order of magnitude shorter in polycrystalline than in amorphous films, attributed to the presence of fast ion migration along grain boundaries. Therefore, the kinetics of filament forming are shown to be highly dependent on HfO_2 microstructure, with possible implications for the inter-device variability of subsequent switching cycles. This Section is based on the journal article "Microstructure dependent filament forming kinetics in HfO_2 programmable metallization cells", in Nanotechnology, 27(42), 2016.

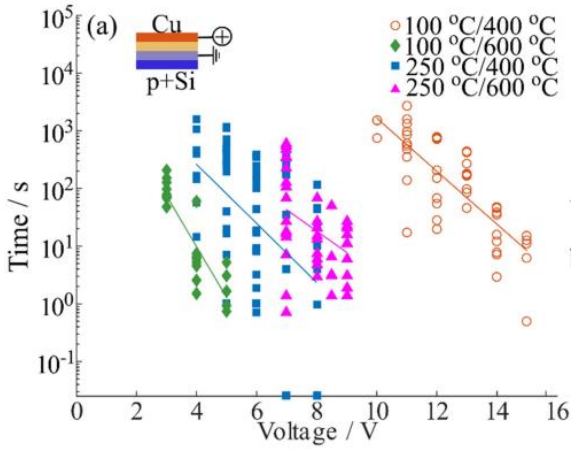

Figure 1.1 Device forming times as a function of applied V for p+Si/HfO_2/Cu devices.

Section 3 details the development of an experimental workflow and conductive atomic force microscopy based "scratch-through" technique used to reveal the 3D structure of conductive filaments formed within p+Si/HfO_2/Cu devices. Devices are based on varying thicknesses (10 – 30 nm) of polycrystalline HfO_2 thin films. Here, unambiguous characterization of conductive filament shape within resistance switching oxide thin films is motivated by the large role shape plays in creating electric and thermal gradients that drive ion migration during filament reforming or breaking. Previous studies have focused either on 2D scans of filament intersections with oxide surfaces[11], or thin TEM slices through the filament[12], leaving significant ambiguity as to the size and shape of the filament through the oxide layer. Based on the work of Celano et al [13], we have developed a technique using a hard doped-diamond tip to simultaneously scribe through the HfO_2 layer of a formed device while measuring local conductivity. 2D scans are later modified by topographic data, aligned to correct for drift, and compiled into a 3D tomogram. Results are not able to be conclusively related to film thickness or microstructure, but reveal a range of filament shapes that deviate from the inverted cone predicted by the leading electrochemical phenomenological model. The role of joule heating from observations of the increasing range of damage caused by compliance current overshoot along a spectrum of forming voltages is implicated in broadening of the shape of filaments.

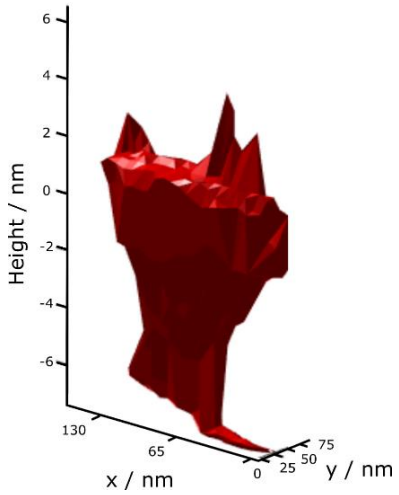

Figure 1.2 Tomogram of conductive filament in 10 nm thick polycrystalline HfO_2 film.

Section 4 concerns the hysteresis of the MIT in undoped, unstrained VO_2 hydrothermally synthesized particles as a basis by which to compare nucleation in doped VO_2 particles. Optical microscopy is utilized to track transition temperatures in an ensemble of particles (N = 347), that show a wide range in particle volume (~0.5 - 7 μm^3). Transformation is generally complete, and occurs in < 0.2 ^oC, indicating nucleation-limited kinetics of both heating and cooling transitions. Results indicate that due to the volume dispersed nature of potent nucleation defects in VO_2 particles, hysteresis increases as volume decreases. Additionally, potent nucleation densities are extracted from data fitting and are demonstrably different than those in VO_2 particles synthesized by alternative routes. This works lays the foundation for describing nucleation statistics in doped particles, and forms the basis of the journal article "Nucleation controlled hysteresis in unstrained hydrothermal VO_2 particles", accepted for publication in Physical Review Materials, 2, 2018.

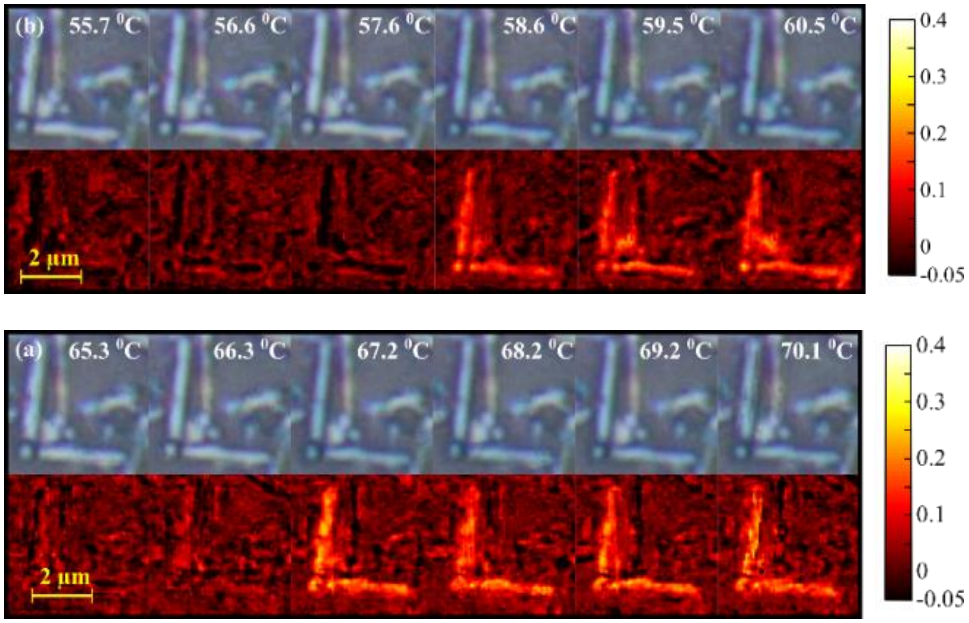

Figure 1.3 Abrupt blue-shift indicating the phase transition in a single VO_2 particle under unpolarized reflected white light and the associated red-difference plots during (a) a heating cycle performed at 1 °C increments (b) the subsequent cooling cycle at 1 °C increments. Difference plots were created by extracting normalized red pixel values, and calculating the difference between a low temperature reference image and high temperature image at each pixel. Reference temperatures were 39.3 ^oC during heating, and 54.7 ^oC during cooling.

Section 5 describes the fabrication and electrical characterization of two terminal devices from boron doped VO_2 particles. DSC characterization of bulk powders shows kinetic changes in heating transition temperatures based on time spent in a low temperature annealing regime, providing yet another potential facet by which device hysteresis might be altered [6]. Because dopants are widely expected to alter the electronic structure of the M1 (insulating) phase, and because domain volumes do not necessarily directly determine resistance or even material resistivity in correlated-oxide materials [14], the fabrication and electrical characterization of lateral two-terminal devices based on B-doped VO_2 particles was proposed. Comparison of thermally driven and current driven switching in devices demonstrates that the unique modulation

of critical switching current with relaxation time is related to thermally driven diffusion of boron within the M1 lattice, rather than any other electric field driven changes in the oxide. Consistent device resistance switching is demonstrated, albeit at the expense of a lowered on/off ratio.

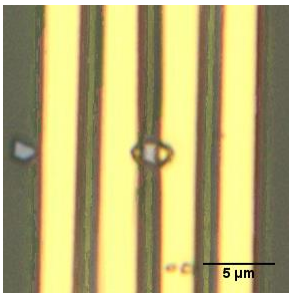

Figure 1.4 A single two terminal B_xVO_2 device.

1.2 Resistance Switching Phenomena

1.1.1 Neuromorphic Applications

A large emphasis has recently been placed on developing alternative memory/programmable bit elements for use in neural networks to meet challenges from transistor scaling, but also to address efficiency limitations inherent in Von Neumann computing architectures. As example, even advanced architectures such as IBM's TrueNorth chip are comparatively inefficient due to reliance on CMOS transistors, which uses 5.4 billion transistors to mimic one million neurons [15]. In contrast, neuromorphic computing schemes consist of a parallel connection of high density low power programming elements (neurons) and reprogrammable, preferably multi-state resistance, non-volatile memory elements (synapses) in order to emulate the analog computing functionality of the human brain. Hardware requirements

include the volatile programming switches (neurons), a dense "cross-bar array of addressable non-volatile memory elements (synapses), selection devices to be incorporated into the "cross-bar" arrays, and peripheral circuitry to support access to these arrays. Given the limitations of conventional transistors, the lower-power, high-density, and large range of memory state (multistate resistance) requirements of neuromorphic architectures requires consideration of the selection and engineering of novel materials.

Possible computing schemes include the biologically inspired spike-timing-dependent-plasticity or spiking neural networks (SNN) and artificial back-propagation learning in deep neural networks (DNNs; Fig. 1.5) . In biological inspired spiking neural networks, timed, asynchronous spikes are measured in two connected neurons. The level of the spike is modulated by the weight, i.e. resistance state of the synapse (NVM element) through which the spike travels. Information is thus encoded in the timing and frequency of the weighted current spikes. Here, one edge of the cross-bar array represents a bank of pre-synaptic neurons, and those addressed by the perpendicular line, a bank of post-synaptic neurons. In contrast to the more developed DNNs, SNNs are still local learning demonstrations, and a fully computational demonstration has not yet been given [16].

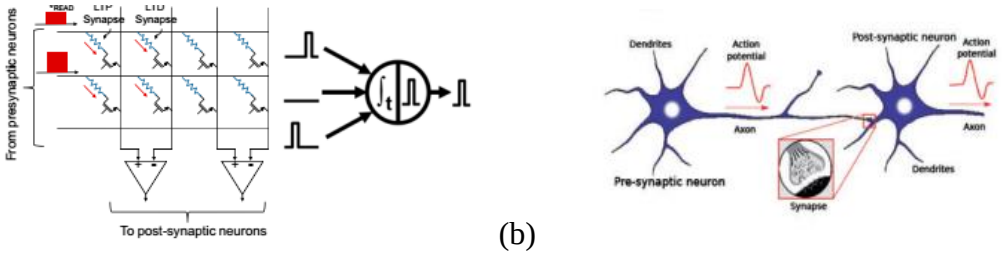

(a) (b)

Figure 1.5. Summary of SNN computing schemes with (a) a SNN cross-bar array showing banks of pre and "post-synaptic" elements, biologically inspired by (b) the method in which neurons connect in parallel with up to 1000 other neurons via a synaptic pathway in which ionic potential/concentration gradients are modulated. Adapted from [16].

Device performance metrics for neuromorphic applications are similar to those of advanced memory systems and consist of high on/off rations, fast write speed, low energy consumption, high endurance, long retention times, high density, and low cost. A summary of current and competitor memory performance is given in Table 1.1. The bench-mark requirements for neuromorphic computing, and memory vary slightly in terms of reliability, as it is thought that device failures can be circumvented by reprogram algorithms and some tolerance is made for reliability. RRAM 1's and 0's are stored as passive resistance states, and require short voltage pulses (1-5 V) to program after the initial forming step. Prototypical device power consumption is currently demonstrated to be between 0.1 and 3 pJ/bit due to the large voltages needed for electro-forming. The process of electron tunneling from the gate oxide to the floating gates occurs on the order of 100 µs, whereas in RRAM the formation/rupture of a filament is in the 10 ns regime. Moreover, large crossbar circuits that can improve density by a factor of 100 have been reported [17]. Therefore, CBRAM stands to improve upon current memory technologies in all areas of electric performance.

Table 1.1 Comparison in Memory Performance of Prototypical RRAM devices

	Memristor	**SRAM**	**DRAM**	**Flash(NAND)**
Density (F^2)	< 4	140	6 – 12	1 – 4
Energy/bit (pJ)	0.1 - 3	0.0005	0.0005	0.00002
Read time (ns)	< 10	0.1 – 0.3	0.005	100,000
Write time (ns)	< 10	0.1 – 0.3	10	100,000
Retention	years	volatile	<< 1s	years
Endurance (cycles)	10^9	> 10^{16}	> 10^{16}	10^4

* adapted from [17]

1.2.2 Survey of Resistance Switching Materials & Motivation of Microscopic Investigation

In general, resistance switching transitions occur by a wide variety of mechanisms in transition metal oxides (Fig. 1.6). Technically, electronic transport in insulators becomes metallic as a function of increased temperature or increased pressure. However, this change is gradual or linear over a large range of temperature. In stark contrast, resistance switching referenced here is a hysteretic, sudden change in state, not-necessarily related to changes in electronic band structure or phase. Instead, mechanisms include ferroelectric tunneling in ferroelectric tunnel junctions and magnetic tunnel junction devices ($BaTiO_3$) [18-20], amorphous to crystalline transitions (GeSbTe) [21], filamentary resistance switching (HfO_2, TiO_2, Al_2O_3, NiO) [22], electrostatic charge accumulation at the interface of the oxide and metal electrode ($SrTiO_3$) [23], as well as the more traditional metal-insulator phase changes (VO_2, NbO_2) [24, 25]. Additionally, within each switching type, delineations based on the active type of ionic migration or function can be made and will be further discussed within the classes of filamentary resistance switching.

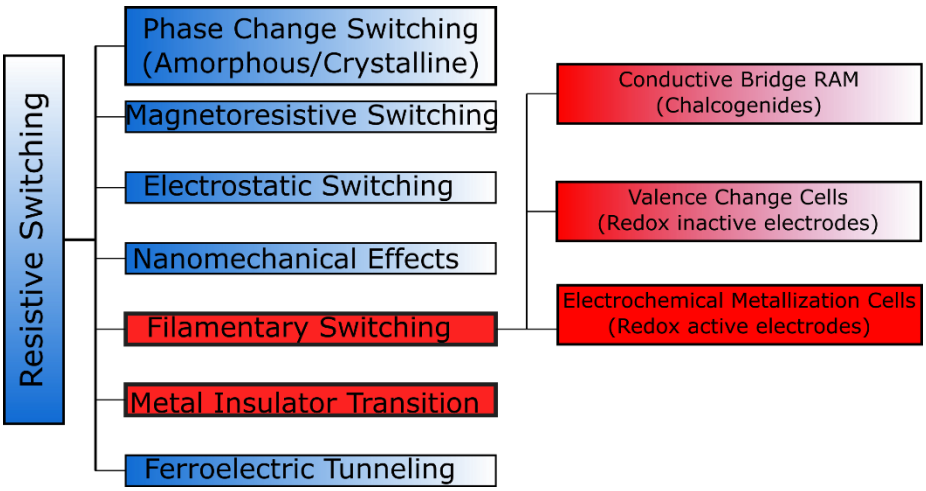

Figure 1.6. Classification of resistance switching phenomena. Filamentary resistance switching and metal insulator transitions are highlighted in red as the topic of this thesis.

Among the many types of resistance switching oxides, or adaptive oxides, two types of switching phenomena offer the potential for excellent device performance, as well as a well-defined space from which to study the kinetics two very different resistance switching behaviors. Namely, these are filamentary resistance switching in HfO_2 thin films, and the metal-insulator transition (MIT) in hydrothermally grown VO_2 particles. In both cases, device level performance is well characterized, however, the microscopic origins of resistance switching that would allow deterministic control of device behavior is not well understood. In terms of device behavior, filamentary resistance switches are plagued by concerns with device variability, while control over hysteresis width in VO_2 is desirable for tuning device volatility. Basic questions as to the size and shape of low/high resistance domains within the switching layer are often made difficult to answer by the nm length scales of thin film layers, or even of VO_2 particles. Conventional characterization techniques such as SEM, XPS, SIMS do not possess the sensitivity to expose changes in domain size, shape, or composition as the state of the device evolves under voltage bias. As a result, explicit confirmation of kinetic models are also difficult to obtain, and leave most models with a

host of questionable assumptions. Therefore, it is necessary to explore techniques that are able to provide direct characterization of conductive filament or metallic/insulating domain geometry.

1.3 Filamentary Resistance Switching in HfO_2

1.3.1 HfO_2 PMC Devices

While many combinations of electrode metals, and solid dielectric insulating layers have been investigated, cells based on HfO_2 dielectric layers are especially promising due to the widespread integration of HfO_2 into semiconductor fabrication plants. In HfO_2, non-volatile resistance switching has been reported to result from field driven migration of either anionic oxygen-vacancies or cationic metallic species (e.g., Cu, Ag); the former is typically referred to as valence change metallization (VCM) cells, and the latter as programmable metallization cells (PMC). Both architectures have demonstrated adequate cycling endurance ($>10^7$ cycles reported) [26, 27], sub nano-second switching time (~300 ps reported) [28], and excellent scalability (10 nm reported) [29]. Because HfO_2 has a high anionic conductivity at higher temperatures, studies on VCM structures predominate in the literature. However, the PMC architecture offers some advantages over a typical VCM cell that make cationic switching salient; high forming voltages, which pose problems for circuit design and device endurance, are typically lowered for cationic switches[30], and the danger of physical damage to the top contact by gas evolution is reduced [31].

Other materials considerations include chemical stability on metal electrodes and Si substrates. In use as a gate oxide in the microelectronics industry, HfO_2 has shown excellent stability with a positive free energy of formation for Hf-Si at temperatures up to 900-1000 ^oC, used in the doping drive in step. Moreover, the HfO_2 system shows predominately the monoclinic phase

under a wide range of temperatures and pressures, reducing the amount of second phase particles forming in the material [32]. It should be noted however, that in thin films grown by ion beam assisted deposition stabilized tetragonal grains and HfO_{2-x} regions have been reported [33].

1.3.2 Working Model of Filamentary Resistance Switching

Both metal-insulator-metal (MIM) and metal-insulator-semiconductor (MIS) stacks are possible configurations. An insulating layer is sandwiched between an electrochemically active metal electrode (Cu, Ag) and a conductive, yet chemically inert counter-electrode is (Pt, W, or p-doped Si). As example, a $Cu/HfO_2/Pt$ cell resistance state is programmed and erased in the following steps (Fig. 7).

1. **FORMING:**

   A positive over-voltage is applied to the active electrode (anode). This drives dissolution of the Cu according to the half-reaction:

   Oxidation $\quad Cu \rightarrow Cu^+ + e^-$

   Copper cations then drift toward the cathode through the oxide in the electric field and are recrystallized at the inert counter-electrode by the half-reaction:

   Reduction $\quad Cu^+ + e^- \rightarrow Cu$

   In the above reaction, the source of the electrons are free electrons generated at the anode. It is generally agreed that certain locations in the oxide are defect rich and more conductive of cations. The filament crystallizes preferentially at these sites and grows from cathode to

anode as the average local electric field increases in strength as distance across the oxide decreases. Once a complete filament ‘short circuits’ the oxide layer, the measured resistance of the device is orders of magnitude lower than the initial insulating state.

2. **RESET:**

A negative voltage is applied to the active electrode, driving an electrochemical dissolution of the metal filament as Cu in the filament is oxidized and drifts back towards the active electrode. Thermal dissipations from joule heating are also thought to play a large role in diffusion of cations away from the filament.

3. **SET:**

A positive voltage is applied at the active electrode, reconnecting the filament, either along the same channel that was previously formed, or forming an entirely new filament along defect paths in the oxide created during the initial forming step.

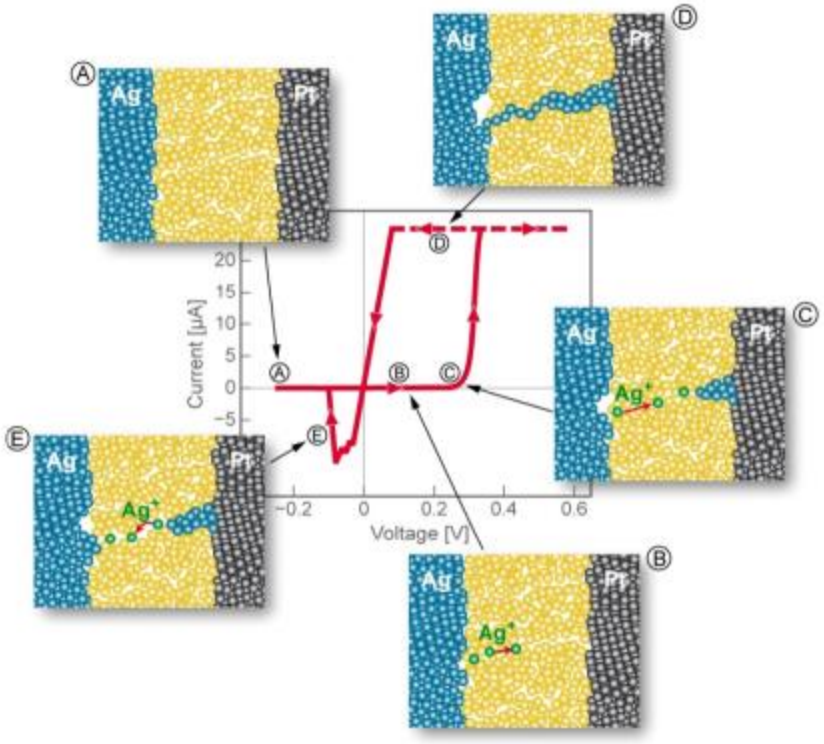

Figure 1.7. Summary of operation of an Ag/Mox/Pt cell. Adapted from [34].

The cyclic application of voltages of opposite polarity is termed bipolar switching, while unipolar switching refers to voltage application of the same polarity. Forming voltages are on the scale of >10V, depending on a variety of factors including oxide thickness, and Set and Reset voltages are substantially lower (1 -4V). HfO_2 based PMC cells have demonstrated both modes of switching, depending on the polarity of the initial forming voltage bias and on electrode material [35]. This peculiarity it understood through the consideration of oxygen anion migration and oxygen vacancy formation. The half-reaction under a positive bias at the anode is given by:

Oxidation $\quad O_O \rightarrow V_O^{\cdot\cdot} + 2e^- + \frac{1}{2} O_2$

The formation of percolation paths of oxygen vacancies, or a filament of conductive oxygen poor HfO_{2-x} phase is the basis of another type of resistance switching memory (ReRAM), which will not be addressed here.

It has been proposed that a single filament provides the primary conduction pathway once formed, although several incomplete or "weaker" filaments may be simultaneously formed. This is evidenced by a lack of dependence of resistance on device area [34].

1.3.3 Applicable Models for Ionic & Electronic Transport

In order for this device reliability to be realized, one would expect an extremely homogeneous environment in the insulating layer, coupled with smooth metal/insulator interfaces to lead to homogeneous local electric fields through the device, as well as equivalent diffusion paths for cation migration. Based purely on this logic, one might expect to find amorphous solids to be the most successful switching layers. Experimentally, this is not the case. A large range of both amorphous electrolytes (Ge-Se) and crystalline insulating (HfO_2) materials have shown to be successful switching layers. This is inherently due to the nano-scale of the system, and its impact on the mixed ionic and electronic conduction within the switching layer

For materials in which the charge transfer step at the electrodes is rate limiting e.g. Ge_xS_y, Ge_xSe_y, Ge-Te, GST, As-S, Ag_2S, Cu_2S, the Butler-Volmer equation which was developed for ion conduction through a liquid electrolyte in traditional electrochemical can be applied. In these materials, the active electrode material, most commonly Cu or Ag, is either already chemically dissolved within the matrix, or is soluble in the matrix and rapidly transported through the materials. This leads to small forming potentials on the order of hundreds of millivolts to complete filament formation. These materials are often implemented in the amorphous state and are often incompatible with back-end-of the-line processing temperatures. Although devices based on these

materials have been demonstrated with high cycle endurance, resistance state retention is often limited at room temperature, and read voltages or thermal fluctuations can reprogram the cell.

Conversely, in oxides, a much higher driving force for diffusion/migration of charged species is required. In HfO_2, the low resistance state is modeled to persist at room temperature for years and is only converted back to the high resistance state by baking at 130 C for 10^4 seconds [36]. For this reason, oxides with high crystallizing temperatures such as HfO_2 have been explored as the switching layer. In these materials, the migration of positive cations from anode to cathode is charge compensated by an opposite migration of counter-ions from the anode to the cathode, and is the rate limiting step. This migration is complicated by nano-size effects and the high volume density of grain boundaries/interfaces in the thin film. At grain sizes approaching 50 nm, interfacial effects can dominate the transport of ions through the medium [37]. It is well known that oxygen vacancies, other point defects, and precipitates often preferentially segregate to grain boundaries, giving rise to the possibility of creating interfaces with either a positive or negative charge to control ion transport along these interfaces. Therefore, control over the ratio of ionic and electronic conduction can also be achieved by aliovalent doping and addition of second phase particles [38].

Additionally, space charge layers are built at the electrode-insulator interface when excess surface charge in the electrode is compensated by a countercharge in the insulator. The electric potential therefore decreases linearly from the interface for one lattice spacing (Helmholtz layer), and then decreases with a shallow exponential decay to the bulk value (Gouy-Chapman) over a space of up to 100 nm. It is therefore evident, that with a total thickness of ~10 to 50 nm, overlap of these space charge layers can occur and can impact ion transport through the bulk of the film.

Several possible models have been proposed for electronic conduction through the insulating layer. These include electron hopping between the potential wells of positively charged defect traps (Frenkel- Poole conduction), tunneling, Schottky interface dominated conduction, and space-charge layer dominated conduction [39]. In studies on HfO_2 dielectric films thicker than 5 nm, the Frenkel-Poole model has been given particular attention, with several sources producing a reasonable fit to experimental data. Fitting I-V data obtained over a range of temperatures is useful not only in determining the conduction mechanism, but also in extracting materials parameters, such as the electron mobility and optical dielectric constant. Physically, a system may show conduction by simultaneous operation of several of these conduction mechanisms. Experimentally it is extremely difficult to separate the fraction of ionic current to electronic current or obtain a good fit to a single model. Impedance spectroscopy has been utilized to study the conduction in Set in Reset states in HfO_2 with some success in this regard [40].

1.3.4 Microscopic Investigations of HfO_2

The key hindrance to industrial application of filamentary resistance switching technologies is the large intra-device and intra-cycle variability in switching voltages and achieved resistance states. However, high repeatability in resistance state cannot be directly translated to the filament diameter as composition and filament location in every cycle and in every different device must be accounted for. As example, energy dispersive spectroscopy (EDS) experiments show that the failure in the set state of $Cu/HfO_2/Pt$ stacks was found to be copper enrichment of the nano-filament. This lead to a permanently set mode in which the connection could no longer be dissolved [41]. Despite these significant gains, an experimentally verified concept that links device variability and filament properties (shape, metal concentration, multiplicity) is lacking, principally due to the challenging nature of studying nanometer scaled phenomena in micro-scale devices. To

this end, several techniques have been applied and elucidated different, and as yet, disconnected understanding of the physical basis of filamentary resistance switching.

Studies utilizing both in-situ TEM and TEM cross-sections following $TiN/Al_2O_3/Cu$ device failure have confirmed that conductive filaments in PMC systems are indeed composed of copper (although the ionization state is unknown), and the conductive area seems to be enriched in copper as the device approaches failure [41, 42]. However, in the *in-situ* studies, the exposure of the device area may introduce artificial electric field distributions as well as artificial defect concentrations associated with the exposed surface. Likewise, moisture has been shown to be an important element in resistive switching [43], and is by nature excluded from TEM experiments. A particularly interesting aspect of filament growth has been generated by high-resolution TEM work that shows build-up of metallic clusters nucleated within the dielectric layer [44]. The first observation of these Ag or Cu clusters, and the associated growth mode in which the filament grows from anode to cathode, opposes the theoretical frame-work of field-driven ion migration followed by electro-chemical reduction at the device cathode [42]. This work has generated some debate as to whether metal ions can in fact be reduced within the bulk of the dielectric, versus nucleating and growing a filament only once reaching the cathode [45]. Thus, TEM has been used to reveal previously unpredicted growth modes of conductive filaments that may be explained by slow dynamics of ion migration through the oxide dielectric layer, as well as show a build-up of copper within failed filaments. However, these studies have been successfully applied to amorphous oxide layers only, excluding a wide range of the oxide materials in which ion migration is accelerated along grain boundaries.

Conductive atomic force microscopy (c-AFM) studies have proven to be especially promising by virtue of combining a high sensitivity circuit and the capability of tracking

microscale features with nanometer scale resolution. These studies include work in which the top electrode of a device has been removed post programming, and a 2D scan of the surface used to reveal conductive pathways (composed of either oxygen vacancies or metal atoms) through the insulating oxide matrix [46-50]. Testing between amorphous and polycrystalline materials shows that conductive spots are preferentially localized at grain boundaries, and are indeed more readily set/reset than their larger, randomly dispersed filaments in amorphous films[48, 51]. While these studies yield interesting information, they present only a snap shot after each programming step has been executed. To gain an understanding of the evolution over operation sequence, the tip has been used as a mobile 100 nm^2 electrode, as a voltage is applied as the tip scans over the surface of the oxide [31, 52-55]. However, these experiments often involve artificially concentrated electric fields around the relatively sharp AFM tip, as well as read voltages high enough to influence filament forming/rupturing and program voltages < 10 V, which may be too low to influence forming in some cases. Therefore, although significant progress has been made towards the microscopic understanding of filament shape evolution over the course of device cycling, a complete link between 3D filament shape and the properties of the oxide matrix is largely absent. This is especially pressing, considering filament forming is controlled by ion migration rates through the oxide, a strong function of oxide microstructure.

1.3.6 Film Processing

Thin films of HfO_2 can be fabricated by a number of techniques which most commonly include atomic layer deposition (ALD) and sputter deposition. Furthermore, the microstructure of the resulting film can be altered by post-deposition annealing. Several different Hf-halogen and Hf-organic ligand precursors have been used in combination with H_2O or a strong oxidant, O_3 for ALD growth. Although an extremely conformal deposition is expected, steric repulsions between

precursor adsorbates, incomplete desorption of reaction by-products, and incomplete desorption of reactants can make finding the correct deposition parameters difficult. 30 nm HfO_2 films deposited below about 350C are mainly amorphous, while those of closely related compound ZrO_2 are partially crystalline at these temperatures. ALD HfO_2 films have been commercially incorporated as gate dielectrics for advanced transistors due to their excellent uniformity, and interfacial smoothness, and low leakage currents are measured in C-V stress modes [56]. ALD films of HfO_2 have also shown excellent switching properties. For films in the 10 – 30 nm range, HfO_2 is deposited as an amorphous film at temperatures below 350C, although the presence of nano-crystallites is possible [56].

Alternatively, magnetron sputtering can be employed in which three target options are available for HfO_2 deposition: a pure HfO_2 target, an Hf target can be used in a reactive sputtering chamber filled with oxygen as well as the sputtering gas, or a pure Hf target with subsequent annealing in O_2. The last method results in films with a variable degree of crystallinity and risks oxidation of the underlying electrode or silicide formation if deposited on Si. Sputtering results in films that are uniform in thickness, with excellent adhesion to the substrate, and retaining the stoichiometry of the target. However, sputtering although more effective at step coverage than evaporation, is inferior to ALD in this respect. HfO_2 films deposited by sputtering are also amorphous in nature and less uniform given the physical creation variable cluster sizes of target material in the resulting ‘cloud’. However, sputtering has the advantage of being a much faster deposition method than ALD.

A post-deposition annealing step is often essential in controlling the microstructure of the resulting HfO_2 film, and therefore the switching behavior of the device. Amorphous HfO_2 films are found to suffer from irreversible breakdown and therefore cannot be reset [37]. Conversely,

grain boundaries may serve as fast diffusion paths for Cu through the insulating layer, while simultaneously serving for sinks of oxygen vacancies. This primes grain boundaries to be a site for localized dielectric breakdown, which has been confirmed by experimental observation of conductive spots at grain boundaries using c-AFM [51]. Additionally, annealing in an oxygen ambient may lead to oxidation of the bottom electrode in species with a large negative free energy of oxide formation e.g. TiN, W. This serves to introduce an unexpected interface which can generate a contact resistance or alter the conduction of charged species so that a failure mode arises in which the low resistance state becomes indistinguishable from the high resistance state [40]. Therefore, the impact of this processing step cannot be underestimated.

1.3.7 Conclusions

Resistance switching in HfO_2 MIM stacks by means of conductive filament formation and dissolution has been described. An applied voltage bias induces redox reactions that dissolve mobile cations at an electrochemically active electrode and deposit them on an inert counter electrode. The rate limiting step in this filament formation is thought to be cation conduction through the oxide layer. This conduction can be described by a variety of mechanisms, with the interface structure (grain structure, and electrode/oxide interface) being highly influential in all cases. Experimental evidence from c-AFM and spectroscopic studies support a view of dopant cation and oxygen vacancy migration localized along grain boundaries. Processing of HfO_2 films is primarily through ALD or sputtering techniques, with excellent devices demonstrated using either technique. However, a higher quality film in terms of uniformity can be created with ALD. A post-deposition thermal anneal is essential in many cases to crystallize the oxide layer, and the impact of this step on electrical performance cannot be underestimated. Although other PMC systems have been commercialized in niche markets, research in filamentary resistance switches

is an ongoing process that seeks to minimize switching variability and to broaden its application in computing memory.

1.4 Resistance Switching in VO_2

1.4.1 Fundamentals of Metal-Insulator in VO_2

Beyond band-type insulators (SiO_2, HfO_2), several transition metal oxides can be classed as correlated-electron materials in which electron-electron interactions and electron-phonon interactions cause electronic transitions not predicted by band theory. Such materials are functionally insulators under weak applied electric field, yet contain only partially filled lower valence bands (indicative of metallic conduction in band-gap type insulators), and undergo technologically important metal-insulator transitions as a function of applied pressure [57], temperature [58, 59], voltage [25, 60, 61] or optical exposure [62] (Table 1.2). These materials are further classified by transformation mechanism, and VO_2 behaves as both a Peierls insulators and Mott insulators [63]. In Peierls type insulators (e.g. NbO_2), the structural distortion which accompanies a crystallographic phase change causes a break in the degeneracy of electronic states, and the formation of a band-gap in the fermi surface. The opening of this band gap lowers the total energy of the system by minimizing electronic contribution to the free energy. This phenomenon is similar to the degeneracy breaking Jahn-Teller distortion in transition metal oxide molecules. In arguments based on crystal-field theory, Goodenough developed a model in which the electronic transition stems from the structural distortion of the crystal lattice[64]. In the rutile state, the density of states at the fermi level is formed from a mixture of the d∥ orbitals and anti-bonding π^* orbitals. Upon symmetry breaking and formation of a monoclinic lattice, the d∥ band splits into filled bonding and empty antibonding states. Meanwhile, the π^* orbitals move to higher energies,

and form a band gap between this band and the lowest occupied d‖ states. However, discrepancies with this model lie in arguments that the another polymorph M2 phase retains a bandgap, despite a lack of VO_2 chain dimerization [65-67], as well as the fs time scale of optically induced transitions far outpacing the time scales of atomic motion (ps) [62].

In Mott type insulators, screened coulombic interactions give rise to two competing energy terms: U, the kinetic energy gained from delocalized electrons, and W, the coulombic repulsion energy from localized electrons. In the limit U < W, a band-gap arises as energy minimization favors electron localization. However, at high enough carrier concentrations, shielding effects can cause bound states to become unstable, resulting in delocalized metallic electron conduction. Therefore, metal-insulator transitions are accomplished by altering charge density, rather than through a structural distortion. A combination of experimental evidence and DFT calculations show logical holes in accepting one mechanism over the other, and point instead to a more cooperative picture between both a Peierls and Mott-Hubbard mechanism [68].

Table 1.2 Several Materials which show a Metal-Insulator Transition and Transition Temperature

Material	**T_{MIT}**	**Mechanism**
VO_2	340 K	Peierls-Mott
NbO_2	1081 K	Peierls
$SmNiO_3$	403 K	disproportionation
$NdNiO_3$	201 K	disproportionation

Regardless of the precise details, the electronic metal-insulator transition is strongly coupled to the crystallographic transition from the low temperature monoclinic, M1 ($P2_1/c$) phase, to the high temperature rutile ($P4_2/mnm$) phase (Fig. 1.8). During the cooling R to M1 phase

transition, the unit cell is almost doubled in volume, and the symmetry of the V – O chains is broken in a martensitic-like transition. The R unit cell maps onto the M1 cell by preserving the b-axis vector, while the β angle changes from 90^{o} to 122.6^{o}.The unit cell grows by ~1 % (with reference to the R c-axis), leading to cracking upon repeated cycling in large single crystals. The slight shifting of the Vanadium atoms from R to M1 is described as a dimerization along the c-axis, as Vanadium atoms shift in position about the c-axis, with V-V bond lengths changing from 2.83 Å in the rutile phase, to alternating 2.75 Å and 2.93 Å in the monoclinic phase.

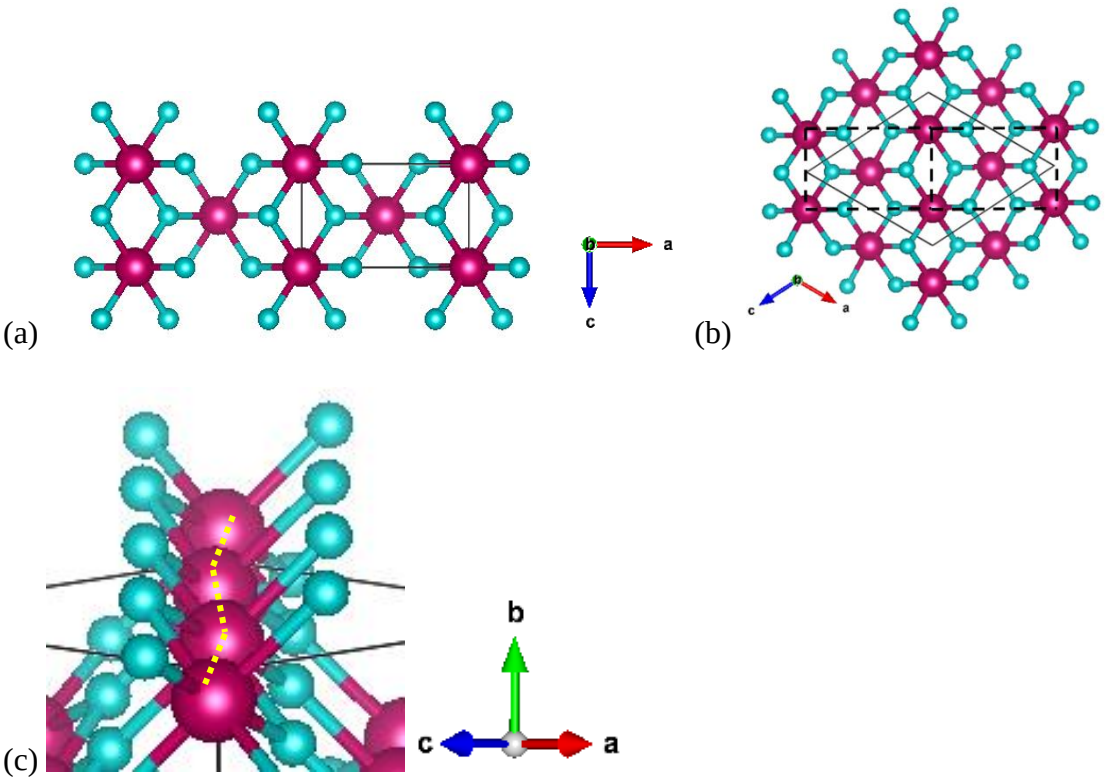

Figure 1.8. (a) Rutile ($P4_2/mnm$) unit cell of the high temperature VO_2 phase (b) M1 ($P2_1/c$) unit cell with orientation relationship to Rutile unit cell shown with dashed black lines. Vanadium atoms are denoted by purple spheres and Oxygen atoms by blue spheres, and the b axis points out of the page. (c) Dimerization of V-V bond lengths along the Rutile c-axis in the M1 phase.

1.4.2 Device Performance of two-terminal VO_2 devices

In addition to thermal or optical driving forces, the near room temperature ~ 67 ^oC metal-insulator transition in VO_2 can be driven by application of a current or bias pulse [25, 69-72], enabling at least two electronically accessible states, i.e. a high resistance insulating (monoclinic) or low-resistance metallic (rutile) state for binary device incorporation. It has been proposed that the transition is driven primarily driven by joule heating, and this is supported by the ability to drive the switch with only current application and by the scaling of the resistance state with electrode area. However, because the relative contributions of the structural phase change and electron occupancy contributions to the phase transition is unresolved, it is still possible that introduction of electric field induced defects (electronic carriers) into the oxide layer may be involved when switching is driven by high electric fields [73]. Once bias application is removed, the VO_2 volume generally cools to room temperature and transitions back to the monoclinic phase, so that resistance state is considered "volatile". However, by engineering a large degree of hysteresis, in which chip operational temperature lies within the hysteretic region, kinetic barriers can prevent the reversal of the phase change once the voltage bias is removed. Then, device resistance state (Ron/Roff) can be considered operationally "non-volatile" and can be read with a low voltage electrical pulse.

An examination of the metrics relevant to memory bit function shows that two-terminal VO_2 switches show competitive performance with other prototypical resistance switching elements (Table 1.3). Excellent endurance in thin film VO_2 devices is demonstrated (10^9 cycles) [74], especially in comparison to bulk crystals in which accumulated defects result in crystal fracturing. In comparison to filamentary RRAM, variability in attained Ron/Roff states is superior, with < 1% deviation in resistance over 4000 cycles [68]. However, the voltage required to drive the phase

transition increases over cycle life as the device approaches failure [72]. A major hurdle towards implementation as a memory element (as well as a selector element) remains the rather limited resistance state ratios between the final metallic and insulating states of VO_2 thin films (Ron/Roff ~ $10^2 – 10^3$), which is much less than in single crystal nanoparticles. It is worth noting that devices based on another correlated transition metal oxide, NbO_2, which undergoes an MIT around 808 ^oC, have also been extensively studied in the context of NVM application. Although NbO_2 is extremely sensitive to oxygen partial pressure and the attainable resistance change between tetragonal and rutile phases is much smaller (10 – 100X), similar performance in switching speed, endurance, variability, and scaling is demonstrated [24]. In VO_2 and especially in NbO_2, significant processing challenges remain for fabrication of devices with suitable memory function for NVM cross-bar elements.

Table 1.3 Memory Element Performance Metrics

	VO_2	**NbO_2**	**PMC**	**SSRAM**
Density (F^2)	4	4	4-16	140
Energy	0.4 fJ [68]	10 fJ	2-25 pJ	0.5 fJ
Ron/Roff Ratio M_T	10^2-10^3 [72, 75]	$10^1 – 10^2$		
Switching Speed	$10^{-1} – 10^1$ ns [72]	2 -20 ns [24, 76]	50-500 ns	0.1-0.3 ns
Endurance	10^9 cycles[74]	10^9 [24]	10^9	10^{16}
Reliability	< 1% change [68]			

Here, it is evident that the application space of neuromorphic devices requires external control of the phase transition properties that determine the resistance state of the VO_2 layer. In

particular, the hysteresis of the MIT is an important parameter to engineer in order to enable either "synapse" or "neuristor" functionality. In addition, the span over driving force of phase coexistence within a device might determine switching voltage/currents and is also worth investigation. As is typical with many prototypical ReRAM devices, the precise mechanisms operating at the device scale are unclear and motivate microscopic investigation of sources of hysteresis.

1.4.3 Origins of Hysteresis & Hysteresis Modulation of the MIT in VO_2

The microscopic origins of hysteresis have been well studied in metallic thermos-elastic martensitic systems, most notably magnetic shape memory alloys [77-83]. Studies of single domain scaled systems have been explained by several energetic terms that result in a nucleation barrier, [78]

$$G = \left[\Delta G_{ch} + \gamma_i A_i + \Delta\gamma_{sf} A_{sf} + E_{el}\right] + E_{fr} - \sigma\varepsilon \qquad (1.1).$$

In addition to the familiar change in chemical free energy between the austenite and martensite phases (ΔG_{ch}) and the difference in surface energy of the A and M phases ($\Delta\gamma_{sf}A_{sf}$) from classical nucleation theory, additional terms are included for the interfacial energy of the A/M interface ($\gamma_i A_i$), elastic energy density of the transformation (E_{el}), and an irreversible friction term (E_{fr}), and finally applied stress/strain ($\sigma\varepsilon$) which is applicable during tensile testing or in samples chemically clamped to a substrate. Despite many experimental works and theoretical thermodynamic modeling studying crystallographic orientation relationships that might minimize lattice mismatch energy, many questions as to the universality of the theory remain unanswered [82].

The origins of hysteresis are much less well investigated in correlated-oxide systems, due in large part to the additional complication added by electron-electron correlations, stabilization

of metastable polymorphs under certain conditions, as well as characterization at the small length scales of crystals required in order to avoid complications encountered in bulk systems (grain boundaries, etc). The majority of kinetic studies make use of techniques require large sample volumes (XRD, DSC, Raman Spectroscopy, etc). In bulk powders, hysteresis could stem from (i) variable nucleation temperature between particles, or (ii) variable transformation rates among domains within a particle, adding the additional convolution of particle size distributions, dopant concentration distributions, etc. Within individual VO_2 volumes, hysteresis could stem from either (1) nucleation limited transformation kinetics on each the heating and cooling transformation (2) nucleation limited transformation accompanied by extended phase coexistence, or (3) growth limited kinetics stemming from friction of the propagating phase front. By studying individual VO_2 volumes at microscopic length-scales, we can begin to answer the basic questions of whether transformation kinetics are nucleation dominated or growth dominated, and how dopant inclusion might change defect populations and the limiting step of either process.

1.4.4 Impact of External Strain

Thus far, microscopic phase coexistence of M1, M2, and R phases, i.e. inhomogeneous transformation, in undoped VO_2 has been observed most rigorously in externally strained single crystalline micro/nano-particles or epitaxial/polycrystalline thin films. Observations are made by a number of techniques in individual particles, including optical light microscopy [84-87], AFM based scanning optical or microwave microscopy [86, 88-91], STM, and TEM [92]. In the majority of these studies, VO_2 is grown by a chemical vapor deposition (CVD) process on SiO_2 substrates at high temperatures (900 – 1100 ^oC), resulting in single phase particles clamped to the substrate, experiencing uniform compressive stress at room temperature. Upon the heating transition between the thermodynamically stable monoclinic phase (M1) to high temperature rutile (R)

phase, c-axis elongation is opposed by the substrate clamping, adding an external strain energy term to the total thermodynamic free energy which serves to stabilize the M1 above bulk T_{cr} temperatures [66, 84, 85, 87]. Energy minimization of this external strain energy is achieved by formation of M1/R interfaces, at the cost of adding interfacial energy to the system, and the balance of these two energy terms results in the formation of periodic M1/R domains along the c-axis of the VO_2 wires. Intentional variation of stress on VO_2 particles has also been achieved both by growth methods [85], bending with a probe-tip [84], and by loading into a mechanical manipulator within a TEM [93] , allowing for the proposed mapping of a VO_2 stress-temperature phase diagram [4]. Importantly, it has been shown that under high strain (>2.2%), insulating domains are composed of the twinned M2 phase that transitions between M1 and R by varying temperature and stress. Stabilization of the M2 phase through strain has allowed for more methodical characterization of M2 resistivity and optical properties than previously possible. In summary, at the individual particle level, observations have shown that phase coexistence regimes in strained particles lead to broad phase transitions, modifications to thermodynamic driving forces which change Tc, and variable ΔT_c. Meanwhile, phase transitions in free-standing VO_2 are sharp and no microscopic domains have been observed.

Previous kinetic studies in individual un-doped free-standing VO_2 particles show that nucleation of M1 (R) embryos upon cooling (heating) is rate-limiting, while the growth of M1 or R phases is too fast to be observed by most techniques [94]. Heterogeneous nucleation is also posited, as calculations using classical nucleation theory yield a homogeneous nucleation barrier of ~ 10^4 kT, ruling out homogeneous nucleation as a mechanism at experimentally observed transition temperatures [9]. Furthermore, a few studies have sought to identify heterogeneous nucleation sites in nano-scaled systems. Oxygen vacancies located at grain boundaries are

implicated by plasmonic resonance spectroscopy as heterogeneous nucleation sites [95]. By contrast, in elastically clamped individual VO_2 particles, nucleation sites have been associated with twin walls during the heating transition, and with point defects introduced by α-particle irradiation [96]. In strained (due to substrate-film lattice-mismatching) epitaxial thin films, nucleation has also been statistically linked to domain boundary sites [88, 89]. Therefore, in both free-standing and elastically clamped individual particles, heterogeneous nucleation is rate-limiting and associated with crystallographic defects which serve to lower the energy barrier for phase transition.

1.4.5 Dopant Addition Impacts on the MIT

In addition to strain engineering [97, 98], control over MIT parameters such as metastable phase stabilization, transition temperature, transition width, and hysteresis have been demonstrated by introduction of chemical doping (Al^{3+} [99, 100], Cr^{3+}[101-103], Mo^{4+}[104], Ti^{4+} [105-107], $W^{4+,6+}$[5, 8, 70]). Additionally, dopant introduction also adds the possibility of introducing phase coexistence or stabilization of metastable phases (M2, M3, Triclinic (T)). Therefore, chemical doping offers the possibility of tuning transition temperature either above or below that of undoped VO_2, as well as increasing or decreasing hysteresis width.

Chemical doping has been demonstrated to change relative phase stabilities of M1 and R phases, depressing (W, Mo, Al) or raising transition temperatures (Cr, Ti), as well as stabilize M2 polymorphs by introducing inhomogeneous lattice strain in substitutional positions, with doping with Al3+ and Cr3+ constituting the bulk of experimental evidence[100]. Most recently, doping with W6+ has also been shown to stabilize domains of M2 with nm length scales alongside M1[8]. In particular, doping with W^{6+} and Mo^{4+} is demonstrated to reduce both M1 and R transition temperatures by reducing the free energy of the R phase due to added lattice strain upon

substitution of V atoms with the larger radii W or Mo atoms. This lattice strain breaks the dimerization of the V-V pairs in the M1 phase, increasing the local symmetry of the octahedron around the W atom. Simultaneously, the W ion donates its two electrons in each site, increasing local charge density and energy for the M1 phase.

In terms of hysteresis, W incorporation has been alternately associated with increased hysteresis width in bulk powder samples [5, 108], as well as relatively narrow hysteresis in W-doped thin films[109]. At a mechanistic level, substitutional dopants, and in particular W, introduce inhomogeneous strain into the system, facilitating the stabilization of metastable phases (M2) or M1 twins which might serve as nucleation points [7, 8]. Whereas dopants might change the nucleation barrier landscape by stabilizing a host of different nucleation sites, dopants might also play a role in growth limited kinetic terms, as well as changing electronic density, orbital occupancy, and therefore energetics of correlated states. So while there is a large body of literature addressing the impact of chemical dopants on transition temperature and phase-co-existence, the mechanisms by which dopants might control hysteresis are not well established.

1.4.6 Conclusions

In conclusion, the metal-insulation transition accompanying the crystallographic phase transition in VO_2 promises technologically important resistance switching application. The degree of hysteresis associated with the phase transition provides an avenue through which to tune the volatility of VO_2's resistance switching behavior. However, the microscopic origins of this hysteresis are complicated by the presence of metastable phase stabilization, phase coexistence, particle size effects, and the crystallographic strain imparted by dopant inclusion. The deconvolution of these several coexisting contributions to phase transition hysteresis requires microscopic imaging of the phase transition which is attempted in this thesis.

1.5 References

[1] Loh O Y and Espinosa H D 2012 Nanoelectromechanical contact switches *Nature nanotechnology* **7** 283

[2] Chang S, Chae S, Lee S, Liu C, Noh T, Lee J, Kahng B, Jang J, Kim M and Kim D-W 2008 Effects of heat dissipation on unipolar resistance switching in Pt/NiO/Pt capacitors *Applied Physics Letters* **92** 183507

[3] Haemori M, Nagata T and Chikyow T 2009 Impact of Cu electrode on switching behavior in a Cu/HfO2/Pt structure and resultant Cu ion diffusion *Applied Physics Express* **2** 061401

[4] Morin F 1959 Oxides which show a metal-to-insulator transition at the Neel temperature *Physical review letters* **3** 34

[5] Whittaker L, Wu T-L, Patridge C J, Sambandamurthy G and Banerjee S 2011 Distinctive finite size effects on the phase diagram and metal–insulator transitions of tungsten-doped vanadium (iv) oxide *Journal of Materials Chemistry* **21** 5580-92

[6] Alivio T E, Sellers D G, Asayesh-Ardakani H, Braham E J, Horrocks G A, Pelcher K E, Villareal R, Zuin L, Shamberger P J and Arroyave R 2017 A Post-Synthetic Route for Modifying the Metal—Insulator Transition of VO2 by Interstitial Dopant Incorporation *Chemistry of Materials* **29** 5401-12

[7] Braham E J, Sellers D, Emmons E, Villarreal R, Asayesh-Ardakani H, Fleer N A, Farley K E, Shahbazian-Yassar R, Arròyave R and Shamberger P J 2017 Modulating the Hysteresis of an Electronic Transition: Launching Alternative Transformation Pathways in the Metal—Insulator Transition of Vanadium (IV) Oxide *Chemistry of Materials* **30** 214-24

[8] Asayesh-Ardakani H, Yao W, Nie A, Marley P M, Braham E, Klie R F, Banerjee S and Shahbazian-Yassar R 2017 Direct evidence of M2 phase during the monoclinic-tetragonal (rutile) phase transition of W-doped VO2 nanowires *Applied Physics Letters* **110** 053107

[9] Lopez R, Haynes T, Boatner L, Feldman L and Haglund Jr R 2002 Size effects in the structural phase transition of VO 2 nanoparticles *Physical Review B* **65** 224113

[10] Rahaman S Z, Maikap S, Ray S K, Lee H-Y, Chen W-S, Chen F T, Kao M-J and Tsai M-J 2012 Record resistance ratio and bipolar/unipolar resistive switching characteristics of memory device using germanium oxide solid electrolyte *Japanese Journal of Applied Physics* **51** 04DD11

[11] Claramunt S, Wu Q, Maestro M, Porti M, Gonzalez M, Martin-Martinez J, Campabadal F and Nafría M 2015 Non-homogeneous conduction of conductive filaments in Ni/HfO2/Si resistive switching structures observed with CAFM *Microelectronic engineering* **147** 335-8

[12] Kwon D-H, Kim K M, Jang J H, Jeon J M, Lee M H, Kim G H, Li X-S, Park G-S, Lee B and Han S 2010 Atomic structure of conducting nanofilaments in TiO 2 resistive switching memory *Nature nanotechnology* **5** 148

[13] Celano U, Goux L, Belmonte A, Opsomer K, Franquet A, Schulze A, Detavernier C, Richard O, Bender H and Jurczak M 2014 Three-dimensional observation of the conductive filament in nanoscaled resistive memory devices *Nano letters* **14** 2401-6

[14] Wei J, Wang Z, Chen W and Cobden D H 2009 New aspects of the metal–insulator transition in single-domain vanadium dioxide nanobeams *Nature nanotechnology* **4** 420

[15] Akopyan F, Sawada J, Cassidy A, Alvarez-Icaza R, Arthur J, Merolla P, Imam N, Nakamura Y, Datta P and Nam G-J 2015 Truenorth: Design and tool flow of a 65 mw 1

million neuron programmable neurosynaptic chip *IEEE Transactions on Computer-Aided Design of Integrated Circuits and Systems* **34** 1537-57

[16] Burr G W, Shelby R M, Sebastian A, Kim S, Kim S, Sidler S, Virwani K, Ishii M, Narayanan P and Fumarola A 2017 Neuromorphic computing using non-volatile memory *Advances in Physics: X* **2** 89-124

[17] Yang J J, Strukov D B and Stewart D R 2013 Memristive devices for computing *Nature nanotechnology* **8** 13-24

[18] Zhuravlev M Y, Sabirianov R F, Jaswal S and Tsymbal E Y 2005 Giant electroresistance in ferroelectric tunnel junctions *Physical Review Letters* **94** 246802

[19] Gruverman A, Wu D, Lu H, Wang Y, Jang H, Folkman C, Zhuravlev M Y, Felker D, Rzchowski M and Eom C-B 2009 Tunneling electroresistance effect in ferroelectric tunnel junctions at the nanoscale *Nano letters* **9** 3539-43

[20] Garcia V and Bibes M 2014 Ferroelectric tunnel junctions for information storage and processing *Nature communications* **5** 4289

[21] Lai S 2003 Current status of the phase change memory and its future: IEEE) p 10.1. 1-.1. 4

[22] Waser R and Aono M 2007 Nanoionics-based resistive switching memories *Nature materials* **6** 833

[23] Sun J, Jia C, Li G and Zhang W 2012 Control of normal and abnormal bipolar resistive switching by interface junction on In/Nb: SrTiO3 interface *Applied Physics Letters* **101** 133506

[24] Pickett M D and Williams R S 2012 Sub-100 fJ and sub-nanosecond thermally driven threshold switching in niobium oxide crosspoint nanodevices *Nanotechnology* **23** 215202

[25] Stefanovich G, Pergament A and Stefanovich D 2000 Electrical switching and Mott transition in VO2 *Journal of Physics: Condensed Matter* **12** 8837

[26] Lien C, Chen Y, Lee H, Chen P, Chen F and Tsai M-J 2010 The highly scalable and reliable hafnium oxide ReRAM and its future challenges: IEEE) p 1084-7

[27] Walczyk C, Wenger C, Sohal R, Lukosius M, Fox A, DaPhookbrowski J, Wolansky D, Tillack B, Mussig H and Schroeder T 2009 Pulse-induced low-power resistive switching in HfO2 metal-insulator-metal diodes for nonvolatile memory applications *Journal of Applied Physics* **105** 114103

[28] Chen Y Y, Govoreanu B, Goux L, Degraeve R, Fantini A, Kar G S, Wouters D J, Groeseneken G, Kittl J and Jurczak M 2012 Balancing SET/RESET pulse for endurance in 1T1R bipolar RRAM *Electron Devices, IEEE Transactions on* **59** 3243-9

[29] Govoreanu B, Kar G, Chen Y, Paraschiv V, Kubicek S, Fantini A, Radu I, Goux L, Clima S and Degraeve R 2011 10× 10nm 2 Hf/HfO x crossbar resistive RAM with excellent performance, reliability and low-energy operation: IEEE) p 31.6. 1-.6. 4

[30] Tsuruoka T, Terabe K, Hasegawa T and Aono M 2010 Forming and switching mechanisms of a cation-migration-based oxide resistive memory *Nanotechnology* **21** 425205

[31] Bersuker G, Gilmer D, Veksler D, Kirsch P, Vandelli L, Padovani A, Larcher L, McKenna K, Shluger A and Iglesias V 2011 Metal oxide resistive memory switching mechanism based on conductive filament properties *Journal of Applied Physics* **110** 124518

[32] Ohtaka O, Fukui H, Kunisada T, Fujisawa T, Funakoshi K, Utsumi W, Irifune T, Kuroda K and Kikegawa T 2001 Phase relations and volume changes of hafnia under high pressure and high temperature *Journal of the American Ceramic Society* **84** 1369-73

[33] Manory R R, Mori T, Shimizu I, Miyake S and Kimmel G 2002 Growth and structure control of HfO2− x films with cubic and tetragonal structures obtained by ion beam assisted deposition *Journal of Vacuum Science & Technology A* **20** 549-54

[34] Valov I, Waser R, Jameson J R and Kozicki M N 2011 Electrochemical metallization memories—fundamentals, applications, prospects *Nanotechnology* **22** 254003

[35] Lin K-L, Hou T-H, Shieh J, Lin J-H, Chou C-T and Lee Y-J 2011 Electrode dependence of filament formation in HfO2 resistive-switching memory *Journal of Applied Physics* **109** 084104

[36] Chen Y Y, Goux L, Clima S, Govoreanu B, Degraeve R, Kar G S, Fantini A, Groeseneken G, Wouters D J and Jurczak M 2013 Endurance/Retention trade-off on cap 1T1R bipolar RRAM *Electron Devices, IEEE Transactions on* **60** 1114-21

[37] Lanza M 2014 A review on resistive switching in high-k dielectrics: A nanoscale point of view using conductive atomic force microscope *Materials* **7** 2155-82

[38] Maier J 2005 Nanoionics: ion transport and electrochemical storage in confined systems *Nature materials* **4** 805-15

[39] Chiu F-C 2014 A review on conduction mechanisms in dielectric films *Advances in Materials Science and Engineering* **2014**

[40] Yoon J-W, Yoon J H, Lee J-H and Hwang C S 2014 Impedance spectroscopic analysis on effects of partial oxidation of TiN bottom electrode and microstructure of amorphous and crystalline HfO 2 thin films on their bipolar resistive switching *Nanoscale* **6** 6668-78

[41] Lv H, Xu X, Liu H, Liu R, Liu Q, Banerjee W, Sun H, Long S, Li L and Liu M 2015 Evolution of conductive filament and its impact on reliability issues in oxide-electrolyte based resistive random access memory *Scientific reports* **5**

[42] Liu Q, Sun J, Lv H, Long S, Yin K, Wan N, Li Y, Sun L and Liu M 2012 Real-Time Observation on Dynamic Growth/Dissolution of Conductive Filaments in Oxide-Electrolyte-Based ReRAM *Advanced Materials* **24** 1844-9

[43] Tappertzhofen S, Valov I, Tsuruoka T, Hasegawa T, Waser R and Aono M 2013 Generic relevance of counter charges for cation-based nanoscale resistive switching memories *ACS nano* **7** 6396-402

[44] Yang Y, Gao P, Li L, Pan X, Tappertzhofen S, Choi S, Waser R, Valov I and Lu W D 2014 Electrochemical dynamics of nanoscale metallic inclusions in dielectrics *Nature communications* **5**

[45] Valov I and Waser R 2013 Comment on Real-Time Observation on Dynamic Growth/Dissolution of Conductive Filaments in Oxide-Electrolyte-Based ReRAM *Advanced Materials* **25** 162-4

[46] Claramunt S, Wu Q, Maestro M, Porti M, Gonzalez M, Martin-Martinez J, Campabadal F and Nafría M 2015 Non-homogeneous conduction of conductive filaments in Ni/HfO 2/Si resistive switching structures observed with CAFM *Microelectronic Engineering* **147** 335-8

[47] Choi B, Jeong D, Kim S, Rohde C, Choi S, Oh J, Kim H, Hwang C, Szot K and Waser R 2005 Resistive switching mechanism of TiO2 thin films grown by atomic-layer deposition *Journal of Applied Physics* **98** 033715

[48] Son J and Shin Y-H 2008 Direct observation of conducting filaments on resistive switching of NiO thin films *Applied Physics Letters* **92** 2106

[49] Singh B, Mehta B, Varandani D, Savu A V and Brugger J 2012 CAFM investigations of filamentary conduction in Cu2O ReRAM devices fabricated using stencil lithography technique *Nanotechnology* **23** 495707

[50] Yang L, Kuegeler C, Szot K, Ruediger A and Waser R 2009 The influence of copper top electrodes on the resistive switching effect in TiO2 thin films studied by conductive atomic force microscopy *Applied Physics Letters* **95** 013109

[51] Lanza M, Zhang K, Porti M, Nafria M, Shen Z, Liu L, Kang J, Gilmer D and Bersuker G 2012 Grain boundaries as preferential sites for resistive switching in the HfO2 resistive random access memory structures *Applied Physics Letters* **100** 123508

[52] Lanza M, Bersuker G, Porti M, Miranda E, Nafría M and Aymerich X 2012 Resistive switching in hafnium dioxide layers: local phenomenon at grain boundaries *Applied Physics Letters* **101** 193502

[53] Szot K, Speier W, Bihlmayer G and Waser R 2006 Switching the electrical resistance of individual dislocations in single-crystalline SrTiO3 *Nature materials* **5** 312-20

[54] Brivio S, Tallarida G, Cianci E and Spiga S 2014 Formation and disruption of conductive filaments in a HfO2/TiN structure *Nanotechnology* **25** 385705

[55] Du Y, Kumar A, Pan H, Zeng K, Wang S, Yang P and Wee A T S 2013 The resistive switching in TiO2 films studied by conductive atomic force microscopy and Kelvin probe force microscopy *AIP Advances* **3** 082107

[56] Kim H, McIntyre P C and Saraswat K C 2003 Effects of crystallization on the electrical properties of ultrathin HfO2 dielectrics grown by atomic layer deposition *Applied physics letters* **82** 106-8

[57] Neuman C, Lawson A and Brown R 1964 Pressure dependence of the resistance of VO2 *The Journal of Chemical Physics* **41** 1591-5

[58] Berglund C and Guggenheim H 1969 Electronic Properties of V O 2 near the Semiconductor-Metal Transition *Physical Review* **185** 1022

[59] Morin F 1961 Halides, oxides, and sulfides of the transition metals *Journal of Applied Physics* **32** 2195-7

[60] Crunteanu A, Givernaud J, Leroy J, Mardivirin D, Champeaux C, Orlianges J-C, Catherinot A and Blondy P 2010 Voltage-and current-activated metal–insulator transition in VO2-based electrical switches: a lifetime operation analysis *Science and technology of advanced materials* **11** 065002

[61] Sharoni A, Ramírez J G and Schuller I K 2008 Multiple avalanches across the metal-insulator transition of vanadium oxide nanoscaled junctions *Physical review letters* **101** 026404

[62] Cavalleri A, Tóth C, Siders C W, Squier J, Ráksi F, Forget P and Kieffer J 2001 Femtosecond structural dynamics in VO 2 during an ultrafast solid-solid phase transition *Physical review letters* **87** 237401

[63] Wentzcovitch R M, Schulz W W and Allen P B 1994 VO 2: Peierls or Mott-Hubbard? A view from band theory *Physical review letters* **72** 3389

[64] Goodenough J B 1971 The two components of the crystallographic transition in VO2 *Journal of Solid State Chemistry* **3** 490-500

[65] Atkin J M, Berweger S, Chavez E K, Raschke M B, Cao J, Fan W and Wu J 2012 Strain and temperature dependence of the insulating phases of VO 2 near the metal-insulator transition *Physical Review B* **85** 020101

[66] Tselev A, Luk'Yanchuk I, Ivanov I, Budai J, Tischler J, Strelcov E, Kolmakov A and Kalinin S 2010 Symmetry relationship and strain-induced transitions between insulating M1 and M2 and metallic R phases of vanadium dioxide *Nano letters* **10** 4409-16

[67] Pouget J, Launois H, Rice T, Dernier P, Gossard A, Villeneuve G and Hagenmuller P 1974 Dimerization of a linear Heisenberg chain in the insulating phases of V 1− x Cr x O 2 *Physical Review B* **10** 1801

[68] Zhou Y and Ramanathan S 2015 Mott memory and neuromorphic devices *Proceedings of the IEEE* **103** 1289-310

[69] Pellegrino L, Manca N, Kanki T, Tanaka H, Biasotti M, Bellingeri E, Siri A S and Marré D 2012 Multistate memory devices based on free-standing VO2/TiO2 microstructures driven by Joule self-Heating *Advanced Materials* **24** 2929-34

[70] Wu T-L, Whittaker L, Banerjee S and Sambandamurthy G 2011 Temperature and voltage driven tunable metal-insulator transition in individual W x V 1− x O 2 nanowires *Physical Review B* **83** 073101

[71] Kumar S, Pickett M D, Strachan J P, Gibson G, Nishi Y and Williams R S 2013 Local Temperature Redistribution and Structural Transition During Joule-Heating-Driven Conductance Switching in VO2 *Advanced Materials* **25** 6128-32

[72] Zhou Y, Chen X, Ko C, Yang Z, Mouli C and Ramanathan S 2013 Voltage-triggered ultrafast phase transition in vanadium dioxide switches *IEEE Electron Device Letters* **34** 220-2

[73] Gopalakrishnan G, Ruzmetov D and Ramanathan S 2009 On the triggering mechanism for the metal–insulator transition in thin film VO2 devices: electric field versus thermal effects *Journal of Materials Science* **44** 5345-53

[74] Radu I P, Govoreanu B, Mertens S, Shi X, Cantoro M, Schaekers M, Jurczak M, De Gendt S, Stesmans A and Kittl J 2015 Switching mechanism in two-terminal vanadium dioxide devices *Nanotechnology* **26** 165202

[75] Ha S D, Zhou Y, Fisher C J, Ramanathan S and Treadway J P 2013 Electrical switching dynamics and broadband microwave characteristics of VO2 radio frequency devices *Journal of Applied Physics* **113** 184501

[76] Kim S, Park J, Woo J, Cho C, Lee W, Shin J, Choi G, Park S, Lee D and Lee B H 2013 Threshold-switching characteristics of a nanothin-NbO2-layer-based Pt/NbO2/Pt stack for use in cross-point-type resistive memories *Microelectronic Engineering* **107** 33-6

[77] Scheibel F, Gottschall T, Taubel A, Fries M, Skokov K P, Terwey A, Keune W, Ollefs K, Wende H and Farle M 2018 Hysteresis Design of Magnetocaloric Materials—From Basic Mechanisms to Applications *Energy Technology* **6** 1397-428

[78] Chen Y and Schuh C A 2011 Size effects in shape memory alloy microwires *Acta Materialia* **59** 537-53

[79] Wang J, Ke X, Chang T, Tian F, Zhou C, Yang S, Fang M, Cao K, Chen Y-S and Sun Z 2018 Zero-thermal-hysteresis Magnetocaloric Effect Induced by Magnetic Transition at Morphotropic Phase Boundary in Heusler Ni50Mn36Sb14-xInx Alloys *Physical Chemistry Chemical Physics*

[80] Bhattacharya K 2003 *Microstructure of martensite: why it forms and how it gives rise to the shape-memory effect* vol 2: Oxford University Press)

[81] Cui J, Chu Y S, Famodu O O, Furuya Y, Hattrick-Simpers J, James R D, Ludwig A, Thienhaus S, Wuttig M and Zhang Z 2006 Combinatorial search of thermoelastic shape-memory alloys with extremely small hysteresis width *Nature materials* **5** 286

[82] James R D and Hane K F 2000 Martensitic transformations and shape-memory materials *Acta materialia* **48** 197-222

[83] Frenzel J, George E P, Dlouhy A, Somsen C, Wagner M-X and Eggeler G 2010 Influence of Ni on martensitic phase transformations in NiTi shape memory alloys *Acta Materialia* **58** 3444-58

[84] Cao J, Ertekin E, Srinivasan V, Fan W, Huang S, Zheng H, Yim J, Khanal D, Ogletree D and Grossman J 2009 Strain engineering and one-dimensional organization of metal–insulator domains in single-crystal vanadium dioxide beams *Nature nanotechnology* **4** 732-7

[85] Wu J, Gu Q, Guiton B S, de Leon N P, Ouyang L and Park H 2006 Strain-induced self organization of metal− insulator domains in single-crystalline VO2 nanobeams *Nano letters* **6** 2313-7

[86] Tselev A, Strelcov E, Luk'yanchuk I A, Budai J D, Tischler J Z, Ivanov I N, Jones K, Proksch R, Kalinin S V and Kolmakov A 2010 Interplay between Ferroelastic and Metal− Insulator Phase Transitions in Strained Quasi-Two-Dimensional VO2 Nanoplatelets *Nano letters* **10** 2003-11

[87] Cao J, Gu Y, Fan W, Chen L, Ogletree D, Chen K, Tamura N, Kunz M, Barrett C and Seidel J 2010 Extended mapping and exploration of the vanadium dioxide stress-temperature phase diagram *Nano letters* **10** 2667-73

[88] Qazilbash M, Brehm M, Andreev G, Frenzel A, Ho P-C, Chae B-G, Kim B-J, Yun S J, Kim H-T and Balatsky A 2009 Infrared spectroscopy and nano-imaging of the insulator-to-metal transition in vanadium dioxide *Physical Review B* **79** 075107

[89] Frenzel A, Qazilbash M M, Brehm M, Chae B-G, Kim B-J, Kim H-T, Balatsky A, Keilmann F and Basov D 2009 Inhomogeneous electronic state near the insulator-to-metal transition in the correlated oxide VO 2 *Physical Review B* **80** 115115

[90] Jones A C, Berweger S, Wei J, Cobden D and Raschke M B 2010 Nano-optical investigations of the metal− insulator phase behavior of individual VO2 microcrystals *Nano letters* **10** 1574-81

[91] O'Callahan B T, Atkin J M, Jones A C, Park J H, Cobden D and Raschke M B 2014 Inhomogeneity in the ultrafast insulator-to-metal transition dynamics in VO $ _2$ *arXiv preprint arXiv:1412.5495*

[92] Chang Y, Yang J, Kim Y, Kim D, Noh T, Kim D-W, Oh E, Kahng B and Chung J-S 2007 Surface versus bulk characterizations of electronic inhomogeneity in a V O 2 thin film *Physical Review B* **76** 075118

[93] Guo H, Chen K, Oh Y, Wang K, Dejoie C, Syed Asif S, Warren O, Shan Z, Wu J and Minor A 2011 Mechanics and dynamics of the strain-induced M1–M2 structural phase transition in individual VO2 nanowires *Nano letters* **11** 3207-13

[94] Yoon J, Kim H, Chen X, Tamura N, Mun B S, Park C and Ju H 2016 Controlling the Temperature and Speed of the Phase Transition of VO2 Microcrystals *ACS applied materials & interfaces* **8** 2280-6

[95] Appavoo K, Lei D Y, Sonnefraud Y, Wang B, Pantelides S T, Maier S A and Haglund Jr R F 2012 Role of defects in the phase transition of VO2 nanoparticles probed by plasmon resonance spectroscopy *Nano letters* **12** 780-6

[96] Fan W, Cao J, Seidel J, Gu Y, Yim J, Barrett C, Yu K, Ji J, Ramesh R and Chen L 2011 Large kinetic asymmetry in the metal-insulator transition nucleated at localized and extended defects *Physical Review B* **83** 235102

[97] Aetukuri N B, Gray A X, Drouard M, Cossale M, Gao L, Reid A H, Kukreja R, Ohldag H, Jenkins C A and Arenholz E 2013 Control of the metal–insulator transition in vanadium dioxide by modifying orbital occupancy *Nature Physics* **9** 661

[98] Jian J, Wang X, Li L, Fan M, Zhang W, Huang J, Qi Z and Wang H 2017 Continuous tuning of phase transition temperature in VO2 thin films on c-cut sapphire substrates via strain variation *ACS applied materials & interfaces* **9** 5319-27

[99] Wu Y, Fan L, Chen S, Chen S, Chen F, Zou C and Wu Z 2014 A novel route to realize controllable phases in an aluminum (Al3+)-doped VO2 system and the metal–insulator transition modulation *Materials Letters* **127** 44-7

[100] Strelcov E, Tselev A, Ivanov I, Budai J D, Zhang J, Tischler J Z, Kravchenko I, Kalinin S V and Kolmakov A 2012 Doping-based stabilization of the M2 phase in free-standing VO2 nanostructures at room temperature *Nano letters* **12** 6198-205

[101] Tan X, Liu W, Long R, Zhang X, Yao T, Liu Q, Sun Z, Cao Y and Wei S 2016 Symmetry-controlled structural phase transition temperature in chromium-doped vanadium dioxide *The Journal of Physical Chemistry C* **120** 28163-8

[102] Miyazaki K, Shibuya K, Suzuki M, Sakai K, Fujita J-i and Sawa A 2016 Chromium–niobium co-doped vanadium dioxide films: Large temperature coefficient of resistance and practically no thermal hysteresis of the metal–insulator transition *AIP Advances* **6** 055012

[103] Miyazaki K, Shibuya K, Suzuki M, Wado H and Sawa A 2014 Correlation between thermal hysteresis width and broadening of metal–insulator transition in Cr-and Nb-doped VO2 films *Japanese Journal of Applied Physics* **53** 071102

[104] Khan G, Asokan K and Ahmad B 2017 Room temperature tunability of Mo-doped VO2 nanofilms across semiconductor to metal phase transition *Thin Solid Films* **625** 155-62

[105] Zhou X, Gu D, Xu S, Qin H and Jiang Y 2018 Investigation on microstructures and phase transition characteristics of titanium/yttrium co-doped vanadium oxide thin films *Materials Research Bulletin* **105** 98-103

[106] Huang K, Meng Y, Xu X, Chen P, Lu A, Li H, Wu B, Wang C and Chen X 2017 Orbital electronic occupation effect on metal–insulator transition in Ti x V1− x O2 *Journal of Physics: Condensed Matter* **29** 355402

[107] Quackenbush N F, Paik H, Holtz M E, Wahila M J, Moyer J A, Barthel S, Wehling T O, Arena D A, Woicik J C and Muller D A 2017 Reducing orbital occupancy in VO 2 suppresses Mott physics while Peierls distortions persist *Physical Review B* **96** 081103

[108] Braham E J, Sellers D, Emmons E, Villarreal R, Asayesh-Ardakani H, Fleer N A, Farley K E, Shahbazian-Yassar R, Arròyave R and Shamberger P J 2017 Modulating the Hysteresis of an Electronic Transition: Launching Alternative Transformation Pathways in the Metal–Insulator Transition of Vanadium (IV) Oxide *Chemistry of Materials* **30** 214-24

[109] Jin P, Nakao S and Tanemura S 1998 Tungsten doping into vanadium dioxide thermochromic films by high-energy ion implantation and thermal annealing *Thin Solid Films* **324** 151-8

2. MICROSTRUCTURE DEPENDENT FILAMENT FORMING KINETICS IN HFO_2 PROGRAMMABLE METALLIZATION CELLS*

2.1 Introduction

Non-volatile memory devices based on resistance switching in thin film metal-insulator-metal stacks hold promise for replacing traditional floating-gate based memory with denser, less power-consuming memory arrays [1]. Logic-intensive computing schemes such as neuromorphic computing may take advantage of the ability to combine logic and memory functions in a single device [2-4]. Furthermore, the possibility of multi-level resistance states [5, 6], and many orders of magnitude non-volatile resistance change introduces the possibility of novel reconfigurable systems and devices. While many combinations of electrode metals, and solid dielectric insulating layers have been investigated, cells based on HfO_2 dielectric layers are especially promising due to the widespread integration of HfO_2 into semiconductor fabrication plants. In HfO_2, non-volatile resistance switching has been reported to result from field driven migration of either anionic oxygen-vacancies or cationic metallic species (e.g., Cu, Ag); the former is typically referred to as valence change metallization (VCM) cells, and the latter as programmable metallization cells (PMC). Both architectures have demonstrated adequate cycling endurance ($>10^7$ cycles reported) [7, 8], sub nano-second switching time (~300 ps reported) [9] , and excellent scalability (10 nm reported) [10]. Because HfO_2 has a high anionic conductivity at higher temperatures, studies on VCM structures predominate in the literature. However, the PMC architecture offers some

* Reprinted with permission from "Microstructure Filament Forming Kinetics in HfO_2 Programmable Metallization Cells" by H. Clarke, T.D. Brown, J. Hu, R. Ganguli, A. Reed, A. Voevodin, P.J. Shamberger, 2016. Nanotechnology, 27(42), 425709, Copyright 2016 by IOP Publishing Ltd.

advantages over a typical VCM cell that make cationic switching salient; high forming voltages, which pose problems for circuit design and device endurance, are typically lowered for cationic switches [11], and the danger of physical damage to the top contact by gas evolution is reduced [12].

A major barrier to deployment of this technology is the large degree of intra- and inter-device variability in macroscopic device characteristics (e.g., Vset, Vreset, Ron, Roff) [1]. Most studies investigating the origins of device variability focus on the stochastic nature of defect formation within a homogeneous dielectric layer, which, at some threshold level, leads to percolation pathways connecting electrodes [13]. While this form of variability model explicitly assumes uniform dielectric layers, it is not clear that dielectrics are uniform and homogeneous as assumed, nor is it clear that uniform layers have the best resistance switching performance in all cases [14, 15]. Many approaches to reduce variability have been investigated, including using bilayer dielectrics [16], oxide layer doping [5, 17], varying electrode materials [18, 19] and circuit design to minimize parasitic capacitance discharge [20]. Surprisingly, comparatively little emphasis has been placed on controlling and characterizing the microstructure of the oxide layer. With the exception of a few studies [21, 22], the link between resistance switching properties and oxide microstructure is still a matter for further investigation.

Conversely, HfO_2 has been intensely studied as a gate dielectric for transistors, and as a dielectric for thin-film capacitors for analog circuits due to its high dielectric constant, low leakage current, high capacitance density, and its chemical stability on Si [23-25]. In particular, it has been found that breakdown voltage decreases with increasing film thickness and decreases with increasing crystallinity[26]. Leakage current has been reported to increase with the introduction of a grain boundaries[27, 28], but has also been shown to decrease post crystallization during high

temperature annealing[29]. In the context of capacitor breakdown, forming of a nano-scale conductive filament can be considered a localized ‘reversible’ breakdown in response to a large electric field, with the possibility for recovery of the initial insulating state.

Filament forming represents the first step in the resistance switching process, and requires higher electric fields than subsequent switching cycles in order to initiate formation of a conductive filament. Rates of field-driven defect migration and generation within the oxide layer during this step may contribute to changes in final conductive filament shape, location, thickness, and multiplicity. In turn, these properties of the initial conductive pathway determine the voltages and resistance states of subsequent cycles. In this case, the inter-device variability of the switch may originate not only from the magnitude of the field applied, but also from the microstructure of the oxide switching layer. Notably, the presence of grain boundaries has been demonstrated to play an important role in the location and thickness of vacancy based filaments [30], and may be equally important in properties of metallic filaments.

Here, we report and discuss the impact of atomic layer deposition (ALD) growth temperatures and post-deposition annealing temperatures on the resulting microstructure of thin (30 nm) HfO_2 films, and on the macroscopic electrical forming/breakdown properties of devices based on these films. We demonstrate a significant decrease in the time to breakdown due to film crystallization, and relate this to the introduction of high-mobility transport pathways along grain boundaries. Furthermore, we show that device bottom interfacial roughness secondarily promotes accelerated breakdown. Three separate modes of breakdown are also observed to correlated with microstructure, and contribute to variability in time until breakdown.

2.2 Methods

2.2.1 Material Preparation

Initial experiments focused on controlling the morphology of the HfO_2 layer by atomic layer deposition (ALD) under varying thermal conditions. HfO_2 films (30 nm thick) were prepared on <100> Si substrates with a three nm thick native oxide layer in a high vacuum ALD Cambridge Nanotech Fiji chamber, using its thermal mode. Tetrakis(dimethylamido)hafnium (TDMA-Hf) held at 75 ^oC and H_2O precursors were utilized as the Hf source and the oxidizer, respectively, and N_2 was used as the carrier/purge gas. Samples on each substrate were grown at ambient temperature of 100 ^oC or 250 ^oC. For the 100 ^oC grown samples, 1 cycle consisted of precursor pulse times of 2 s followed by 30 s purge time; for 250 ^oC grown samples, pulse times were 2 s followed by a 15 s wait cycle. In either case, 30 nm of HfO_2 was obtained after 360 cycles. For each growth condition, films were furnace annealed at 400 ^oC, 500 ^oC, or 600 ^oC in lab air for 3600 s.

Subsequent fabrication focused on deposition of HfO_2 in a MIM structure using three different bottom electrodes: p+ Si/HfO_2/Cu, Si/TiN/HfO_2/Cu, and Si/a-SiO_2/W/HfO_2/Cu. Heavily boron-doped <100> p+ Si substrates (0.001 – 0.005 Ω-cm) were obtained from a commercial distributor; while this bottom electrode had slightly higher resistance than other electrodes, it had the advantage of introducing a very smooth electrode/HfO_2 interface (areal root mean square roughness, S_q, < 0.2 nm). p+ Si wafers were rinsed in buffered oxide etch to remove native oxides before loading into the ALD chamber. 100 nm thick TiN bottom electrodes were sputtered on <100> Si wafers by a commercial distributor (Nova Electronic Materials). Finally, W bottom electrodes were fabricated by sputtering 300 nm thick W films on Si/a-SiO_2 wafers at $P = 2.5 \cdot 10^{-8}$ bar total pressure. Both TiN and W substrates were rinsed in a progressive bath of acetone,

isopropyl alcohol, and distilled water to remove organic contaminants prior to deposition of the dielectric HfO_2 layer. Thin layers (30 nm) of HfO_2 were deposited on p+ Si and on TiN bottom contacts using the same growth and annealing conditions as before. Films deposited on W bottom electrodes were annealed in a tube furnace in O_2 at 1 bar for 1800 s. Annealing at 600 ^oC for 1800 s resulted in delamination of the HfO_2 layer/oxidation of the W layer. HfO_2 films were cleaved into one cm^2 samples, and cleaned in a progressive solvent bath of acetone, methanol, isopropyl alcohol, and distilled water with 300 s sonication in each bath. Cu top electrodes (100 nm thick) were deposited through a shadow mask by e-beam evaporation. Resulting top electrodes were squares with edge lengths of 40 x 40 μm^2.

2.2.2 Material Characterization

Topographic characterization was performed with an Asylum MFP 3-D atomic force microscope (AFM) under AC 'tapping' mode. Several AFM scans (N > 3) were taken on each sample to provide uncertainty estimates. Areal root mean squared roughness (S_q) values were calculated as the standard deviation from the mean surface height over a 1 μm^2 area. X-ray diffraction data for samples deposited on Si/a-SiO_2, Si/TiN, or p+ Si were obtained using a Rigaku Smart-lab diffractometer; Si/a-SiO_2/W/HfO_2 films were characterized on a Bruker D8 Advance diffractometer. Both instruments utilized Cu Kα radiation and a parallel incident beam. Crystalline orientation was measured as a ratio of the two highest intensity diffraction peaks, as low overall scattering intensity precluded meaningful whole pattern fitting for most spectra.

Electrical characterization was performed on a Keithley 4200 semiconductor parameter analyzer equipped with remote amplification modules. Tests were performed using a 2 terminal set-up, in which the bottom electrode was grounded and a positive or negative bias applied at the top copper electrode; this arrangement was previously demonstrated to lead to formation of

metallic copper filaments under positive bias[31], and oxygen-vacancy rich filaments under negative bias[8]. A compliance current of 10 μA to 1 mA was utilized to prevent irreversible filament formation due to overcurrent, although overshoot of the set current value almost certainly occurred due to discharge of stray capacitances[20]. Electroforming was studied in p+ Si/HfO_2/Cu and Si/TiN/HfO_2/Cu devices due to the outstanding yield offered in these devices, and the accessible range of microstructures they afforded. Both constant bias and voltage sweeps were used to form conductive filaments. The time at which forming began (t_{begin}) and completed (t_{form}) at constant bias, and the voltage at which forming completed (V_{form}) in the sweep were recorded. Virgin 40 μm devices were used for each data point in this study.

2.3 Results

2.3.1 Film Crystallinity and Degree of Orientation

Degree of HfO_2 crystallinity and texture was observed to vary as a function of ALD growth temperature, post-deposition annealing temperatures, and underlying substrate (Fig. 2.1; Table 2.1). On all substrates, films grown at 100 °C and annealed at 400 °C or less show no diffraction peaks in XRD, suggesting an amorphous film. Films crystallized upon post-deposition annealing at 600 °C. ALD growth at 250 °C yielded amorphous as-deposited films on a-SiO_2, W, and TiN substrates. However, high temperature growth on single crystalline p+ Si substrates yielded a polycrystalline film (Fig. 2.1c). Upon post-deposition annealing, high temperature deposited films crystallized at a lower temperature than their low growth temperature counterparts (400 °C) on all substrates. Thus, despite the lack of observable crystallinity in as-deposited 250 °C films, some initial nucleation likely occurred during the ALD growth process in order to facilitate

crystallization at lower annealing temperatures. In all cases, crystalline HfO_2 is observed in the stable low-temperature monoclinic Baddelyite structure ($P2_1/c$, #14).

Table 2.1. Summary of microstructural properties (S_q, average grain size, and degree of orientation) resulting from thermal deposition and post-deposition annealing conditions. * Indicates that surface roughness data was not collected for this film. **Indicates that the $(\mathbf{111})$ and $(\bar{\mathbf{1}}\mathbf{11})$ peaks could not be resolved from the XRD pattern due to overlap with a Si substrate peak.

Subst.	Dep. Temp. (°C)	Anneal Temp. (°C)	S_q (nm)	Grain Size (nm)	$\mathbf{A_{(111)}/A_{(\bar{1}11)}}$
Si/SiO₂	100	---	---	---	amorphous
	100	400	---	---	amorphous
	100	600	---	---	0.15±0.03
	250	---	---	---	amorphous
	250	400	---	---	0.38±0.01
	250	600	---	---	0.305±0.007
W	100	---	---	---	amorphous
	100	400	---	---	amorphous
	100	600	---	---	amorphous
	250	---	---	---	amorphous
	250	400	---	---	0.39±0.06
	250	600	---	---	0.28±0.09
TiN	100	400	1.0±0.1	---	amorphous
	100	600	2.1±0.2	25±4	1.2±0.4
	250	---	*	---	amorphous
	250	400	1.8±0.1	40±8	0.46±0.01
	250	600	1.7±0.1	33±1	0.42±0.04
p+ Si	100	400	0.15±0.02	---	amorphous
	100	600	0.31±0.02	24±2	0.60±0.03
	250	---	1.32±0.03	35±2	**
	250	400	1.23±0.09	37±3	0.54±0.09
	250	600	1.2±0.1	36±4	0.38±0.03

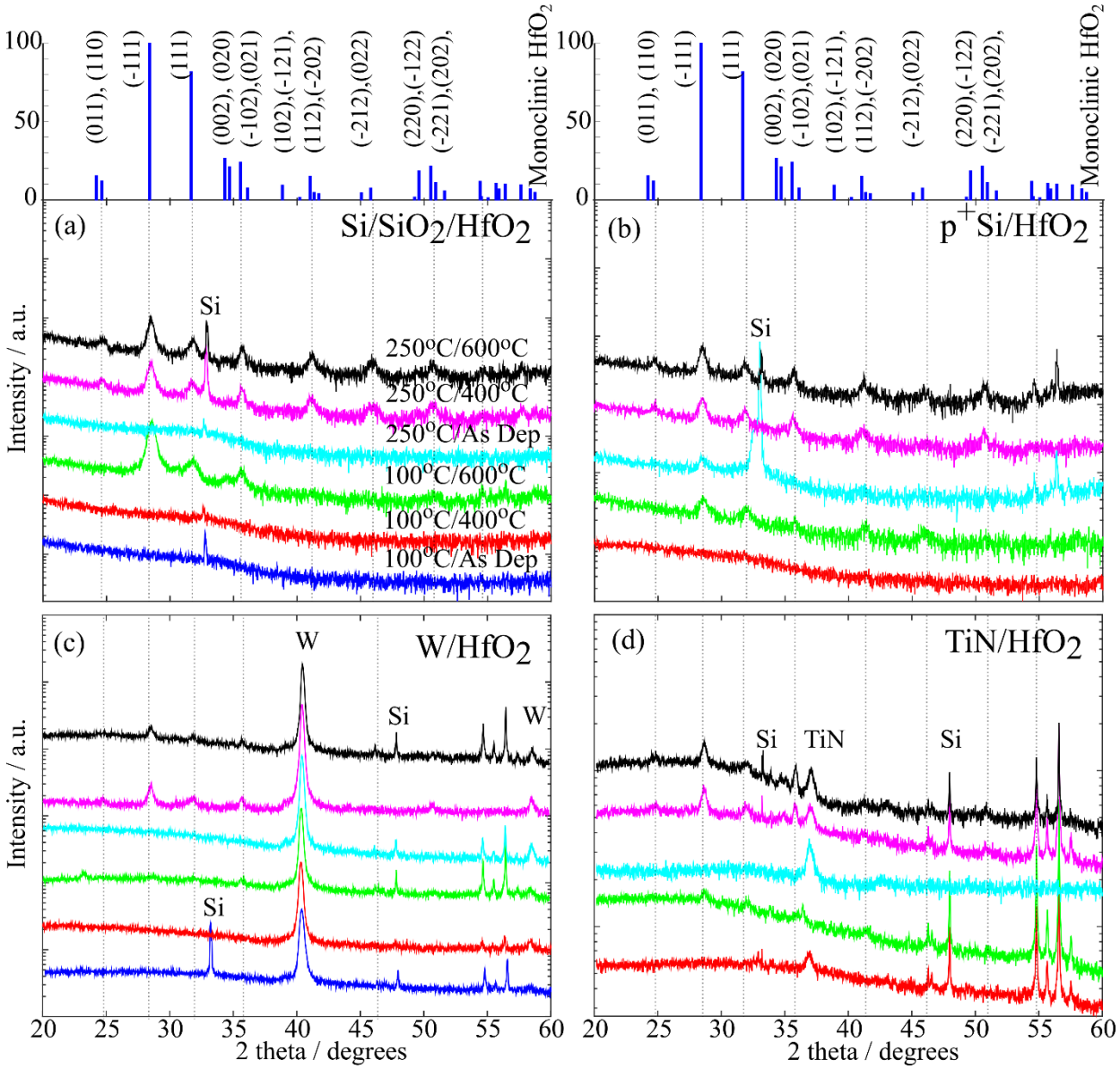

Figure 2.1. XRD Spectra for 30 nm HfO_2 films. Growth conditions given by deposition temperature/annealing temperature appear in the same order and color for each spectrum. The expected powder diffraction pattern for monoclinic HfO_2 with labeled peaks and expected relative intensities [32] is given above for reference (a) XRD spectra for Si/a-SiO2/HfO_2 films (b) XRD spectra for p+Si/HfO_2 films (c) XRD spectra for W/HfO_2 films (d) XRD spectra for TiN/HfO_2 films.

Degree of orientation in polycrystalline films demonstrates a strong dependence on substrate identity and a complicated dependence on initial ALD growth temperatures (Table 2.1;

Fig. 2.2). With one notable exception, all films show some degree of $(\bar{1}11)$ texture, with the area ratio of the second highest intensity (111) peak to the most intense $(\bar{1}11)$ peak less than the expected powder diffraction value ($A_{(111)}/A_{(\bar{1}11)}$= 0.80) [32]. On Si/a-$SiO_2$ substrates, post-deposition annealing of low growth temperature films (grown at 100 ^oC/annealed at 600 ^oC) resulted in strongly $(\bar{1}11)$ textured films, where the area ratio $A_{(111)}/A_{(\bar{1}11)}$ is (0.15 +/- 0.03). In contrast, post-deposition annealing of high temperature films (grown at 250 ^oC/annealed at 400 ^oC or 600 ^oC) resulted in a lesser degree of orientation; $A_{(111)}/A_{(\bar{1}11)}$ is 0.38+/- 0.01 and 0.305+/- 0.007, respectively. In films grown on single crystalline p+ Si substrates, however, texture development resulted from increased thermal budget. $A_{(111)}$ of the as deposited film could not be assessed due to overlap with an Si substrate peak. Otherwise, the degree of orientation of HfO_2/p+ Si films increases with growth temperature/annealing temperature in the following order: 100 ^oC /600 ^oC < 250 ^oC /400 ^oC < 250 ^oC /600 ^oC. TiN/HfO_2 crystalline films show the same trend in degree of orientation with thermal budget, albeit with films generally more randomly oriented than p+ Si films (Table 2.1; Fig. 2.2). Therefore, the thermal dependence of $(\bar{1}11)$ texture varies between substrate groups, being the most pronounced when HfO_2 films are deposited at a low temperature (100 ^oC) on a-SiO_2 substrates. On crystalline p+ Si and TiN substrates, increasing thermal budget results in increasing film $(\bar{1}11)$ texture.

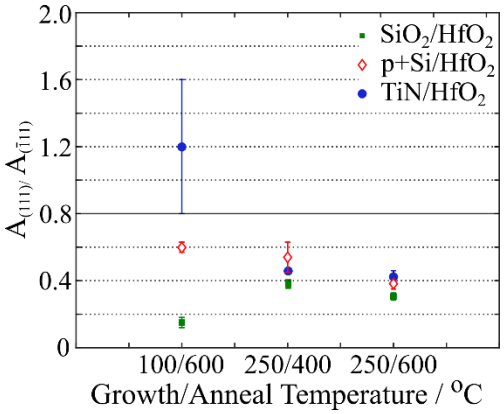

Figure 2.2. Degree of HfO_2 orientation as a function of processing temperatures and bottom substrate. The expected $\mathbf{A_{(111)}/A_{(\bar{1}11)}}$ from the powder diffraction pattern [32] is marked by the solid line.

High resolution transmission electron microscopy (HRTEM) was performed on Si/a-SiO_2/HfO_2 films and confirms XRD results (Fig. 2.3). The randomly oriented polycrystalline film (250 ^{o}C/400 ^{o}C) possesses a columnar grain structure with disordered grain boundaries < 1 nm in width oriented nearly perpendicular to the substrate. All observed boundaries are continuous between the top and bottom electrodes. In contrast, the Si/a-SiO_2/HfO_2 film (100 ^{o}C/600 ^{o}C) is confirmed to possess a strongly textured microstructure, with columnar grains oriented with $(\bar{1}11)$ planes nearly parallel to the a-SiO_2 interface. Grain boundaries in this film are difficult to discern in cross-sectional HRTEM images due to the continuous nature of nearly-parallel basal planes in neighboring grains. No clear competitive growth region is observed near the basal plane of these highly-oriented films, suggesting that texture is inherited from preferred orientation of nuclei rather than through orientation-dependent growth rates.

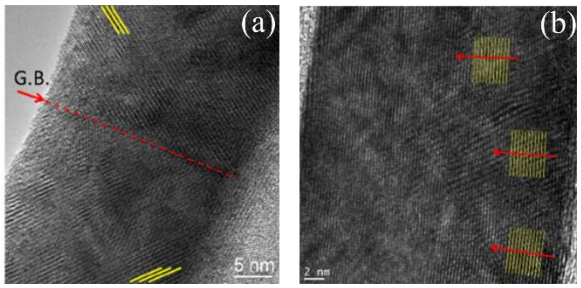

Figure 2.3. High resolution TEM cross-section of (a) randomly oriented polycrystalline grains in the Si/a-SiO_2/HfO_2 250 ^oC /400 ^oC film. Yellow lines indicate (100) planes (b) Oriented columnar grains in the Si/a-SiO_2/HfO_2 100 ^oC /600 ^oC film. Yellow lines indicate ($\bar{1}11$) planes.

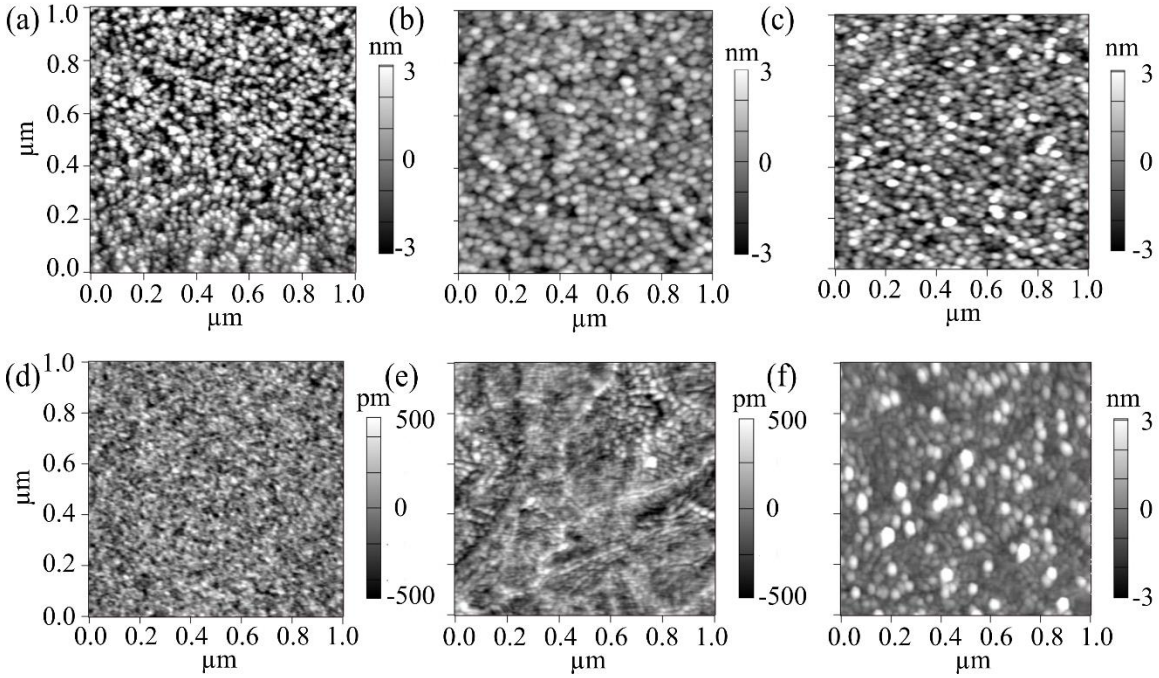

Figure 2.4. Topography of (a) TiN substrate (b) HfO_2 film deposited on TiN at 100 ^oC and annealed at 400 ^oC (c) HfO_2 film deposited on TiN at 250 ^oC and annealed at 600 ^oC (d) p+Si substrate (e) HfO_2 film deposited on p+ Si at 100 ^oC and annealed at 600 ^oC (f) HfO_2 film deposited on p+ Si at 250 ^oC and annealed at 600 ^oC.

2.3.2 Interfacial Roughness and Average Grain Size

AFM scans (Fig. 2.4) show that areal root mean square roughness (S_q) of p+ Si/HfO_2 films and TiN/HfO_2 films show different degrees of dependency on bottom substrate roughness and initial deposition temperature (Fig. 2.5a). p+ Si substrates are initially very smooth (S_q < 0.2 nm), and both the amorphous and polycrystalline HfO_2 films deposited on p+ Si at 100 °C possess S_q< 0.4 nm. The polycrystalline HfO_2 film on p+ Si (100 °C /600 °C) shows an anomalous surface morphology of ridges instead of the usual granular structures seen in all other films (Fig. 2.4e). Films deposited on p+ Si at 250 °C are composed of a granular texture in all cases with a relatively rough surface (S_q> 1 nm). Thus, surface roughness of HfO_2 films on p+ Si substrates appears to be unrelated to film crystallinity, which varies with post-deposition annealing, and primarily a function of initial deposition temperature. In contrast, TiN substrates are initially relatively rough (S_q > 1 nm), and overlying bare HfO_2 films (Fig. 2.4a-c) are assumed to inherit the roughness of the underlying TiN film, independent of crystallinity or growth temperature (Fig. 2.5a). Therefore, HfO_2 film topography (S_q) is obscured by bottom substrate profiles when deposited on rough TiN substrates, but dictated by thermal budget when grown on smooth p+ Si substrates.

Average grain size in both p+ Si/HfO_2 and TiN/HfO_2 films increases with ALD growth temperature, and only marginally with post-deposition annealing temperature (Fig. 2.5b; Table 2.1). The polycrystalline HfO_2 film on p+ Si (100 °C /600 °C) shows a grain diameter of 24±2 nm. In the high temperature (250 °C) deposit set, average grain diameter ranges from 35±2 nm as-deposited to 36±4 nm with a 600 °C anneal, showing little grain growth upon annealing. Similarly, in TiN/HfO_2 films, grain size increases most significantly between the thermal growth conditions 100 °C/600 °C and 250 °C/400 °C (Fig. 2.5b; Table 2.1). Here, initial deposition temperature,

rather than post-deposition annealing temperature, dictates the grain size of HfO_2 films on both p+Si and TiN substrates.

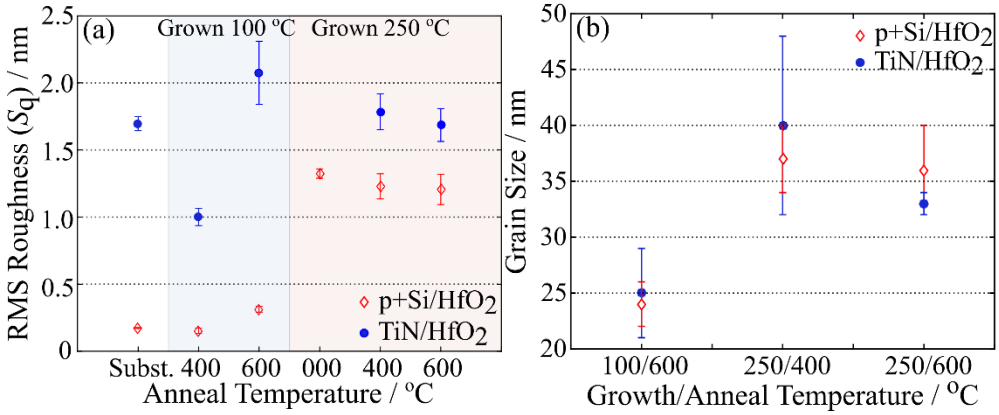

Figure 2.5. (a) RMS roughness values (S_q) as a function of processing conditions for HfO_2 films on p+Si substrates and TiN substrates. (b) Average grain size determined from AFM image analysis in p+ Si/HfO_2 and TiN/HfO_2 films.

2.3.3 Interfacial Oxide Layers

In those TiN bottom electrode samples grown at 100 °C and annealed at 600 °C, the bottom electrode of the MIM stack became non-conductive and the film exhibited a noticeable color change in reflected white light (indicative of a change in film thickness or dielectric constant), suggesting oxidation occurred during annealing. Forming data was not obtained from this film. In all other films, bottom electrode conductivity was maintained, and only slight color changes were observed, suggesting that SiO_x or TiO_x interlayers were relatively minimal. Thickness of these layers likely does not exceed 2-4 nm, as evidenced by HRTEM analysis (Fig. 2.2) and by x-ray reflectometry analysis (XRR) of the initial set of $HfO_2/SiO_x/Si$ films, which was grown on a native SiO_x oxide layer (Fig. A-2). As exception, the film stack deposited at 100 °C and annealed at 600 °C possesses an interfacial SiO_x layer with a 7.3 nm thickness. While SiOx or TiOx interfacial

layers are anticipated to always be present to some minor extent, we interpret changes in filament formation behavior to be dominantly controlled by the thicker layer in the MIM stack, i.e. the HfO_2 layer (26.8 – 29.7 nm).

2.3.4 Filament Forming Under Constant Bias

To understand the role of oxide microstructure in ionic transport and the formation of conductive filaments, low-resistance states were induced under a constant bias in 40 x 40 μm^2 TiN/HfO_2/Cu and p+ Si/HfO_2/Cu devices in both amorphous films and polycrystalline films. A constant, positive or negative bias was applied to the Cu top electrode in order to induce cationic or anionic switching, respectively.

The time at which the conductive filament has completely formed, t_{form}, is defined as the time at which the compliance current is abruptly reached; t_{form} decreases exponentially with increasing electric field applied in all cases (Fig. 2.6). In addition, four major trends in t_{form} data are observed based on processing temperatures of p+ Si/HfO_2 and TiN/HfO_2 films. (1) t_{form} is generally an order of magnitude longer in amorphous films than in polycrystalline films, irrespective of film substrate or bias polarity (Fig. 2.6). (2) Within the suite of films deposited on p+ Si, significant differences in t_{form} are observed between polycrystalline films as a function of thermal processing conditions (Fig. 2.6a, c). This trend is observed only under positive bias. The order of increasing t_{form} by growth temperature/annealing temperature is: (100 °C /600 °C), (250 °C /400 °C), and (250 °C /600 °C). (3) In the suite of films deposited on TiN, t_{form} data also show polarity dependent differences between polycrystalline films (Fig. 2.6b, d). Forming times are observed, under negative bias, to be generally longer in polycrystalline films processed at (250 °C /400 °C) than in those processed at (250 °C /600 °C). No such differences are observed under positive bias. (4) Finally, forming times are longer in all p+ Si/HfO_2/Cu devices than in

TiN/HfO_2/Cu for the same processing temperatures. The most remarkable difference is obtained between amorphous p+ Si/HfO_2/Cu and TiN/HfO_2/Cu devices, with extrapolated t_{form} data two orders of magnitude longer in p+ Si devices. Strong evidence is therefore obtained that filament forming mechanisms depend chiefly on oxide microstructure (1), but also to a lesser extent on interfacial properties associated with TiN and p+ Si bottom substrates (2,4), and the identity of the mobile ion species (3).

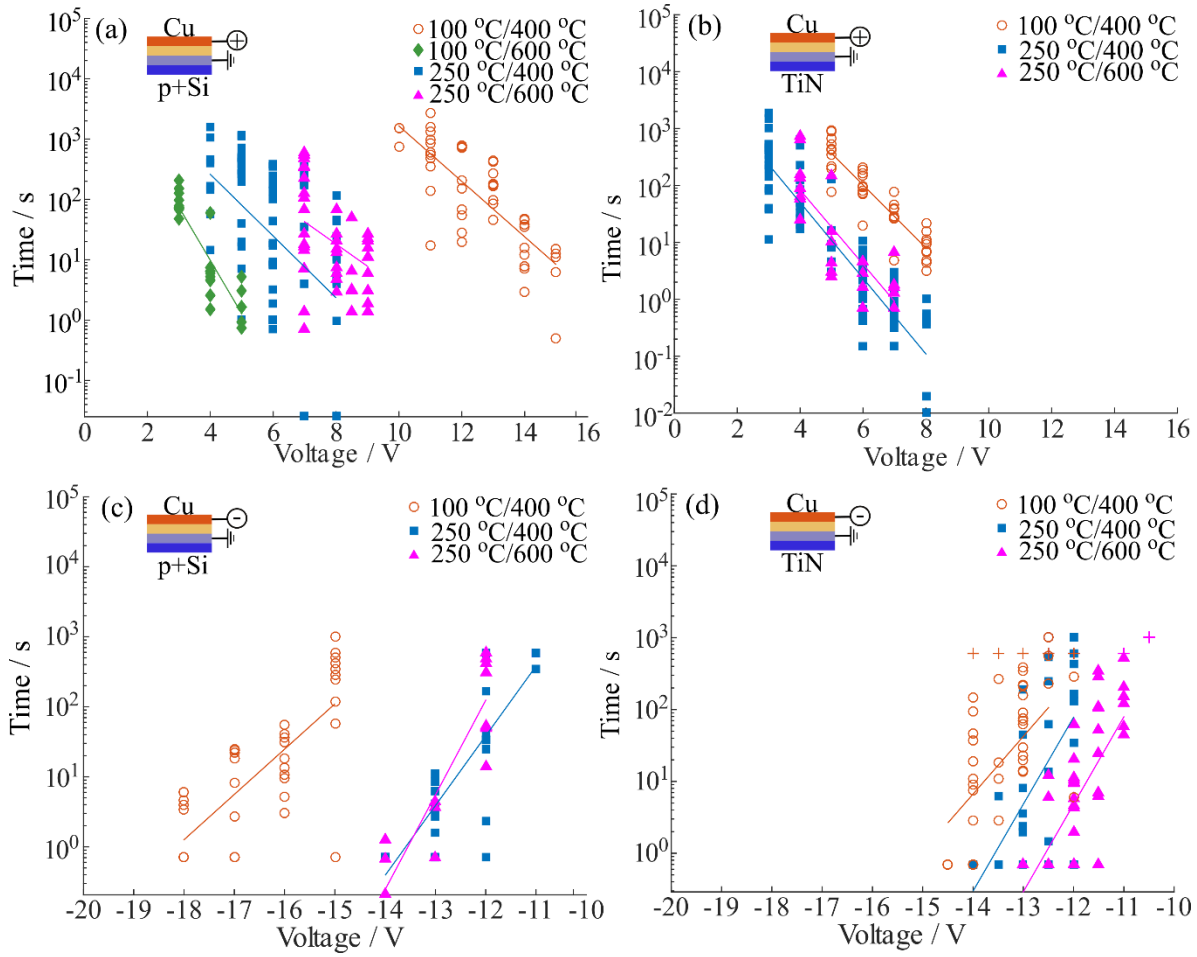

Figure 2.6. Time at which forming ends (t_{form}) as a function of constant applied voltage for (a) p+ Si/HfO_2/Cu devices under positive bias (b) TiN/HfO_2/Cu devices under positive bias (c) p+ Si/HfO_2/Cu devices under negative bias (d) TiN/HfO_2/Cu devices under negative bias. Devices based on a polycrystalline oxide layer are represented by filled shapes and their amorphous oxide counterparts by open circles. Crosses represent devices that have not formed after 600 s of constant voltage stress.

2.3.5 Leakage Current and Forming Current Transients

Current evolution under constant positive bias followed two distinct pathways, depending on dielectric microstructure (Fig. 2.7). In amorphous films (Fig. 2.7a, 2.7c), current evolution transitioned through three regimes. In regime I, leakage current decays with time (Fig. 2.7a, 2.7c). Within this regime, pulsing bias at V=V+ for 20 s, followed by V=0 for 20 s resulted in a cyclic

charging/discharging behavior (Fig. 2.8a). While capacitive charging of a device might result in similar behavior, the accumulated charge represented by these transients is orders of magnitude larger than that expected due to the capacitance of a device this size (~3 nF versus 5 pF). Furthermore, this leakage current decay is observed only in films deposited at 100 °C, regardless of final annealing temperature or crystallinity. Thus, this behavior is likely due to charging of interfacial and bulk trap sites created during low temperature ALD that are not removed upon annealing[33, 34]. Interestingly, the presence of an initially high oxygen defect concentration within films deposited at 100 ^{o}C does not predispose faster filament forming kinetics; p+ Si/HfO_2 films processed at 100 ^{o}C /400 ^{o}C form at much longer times than films processed at 100 ^{o}C /600 ^{o}C, with the major difference between the films being an amorphous versus a polycrystalline microstructure.

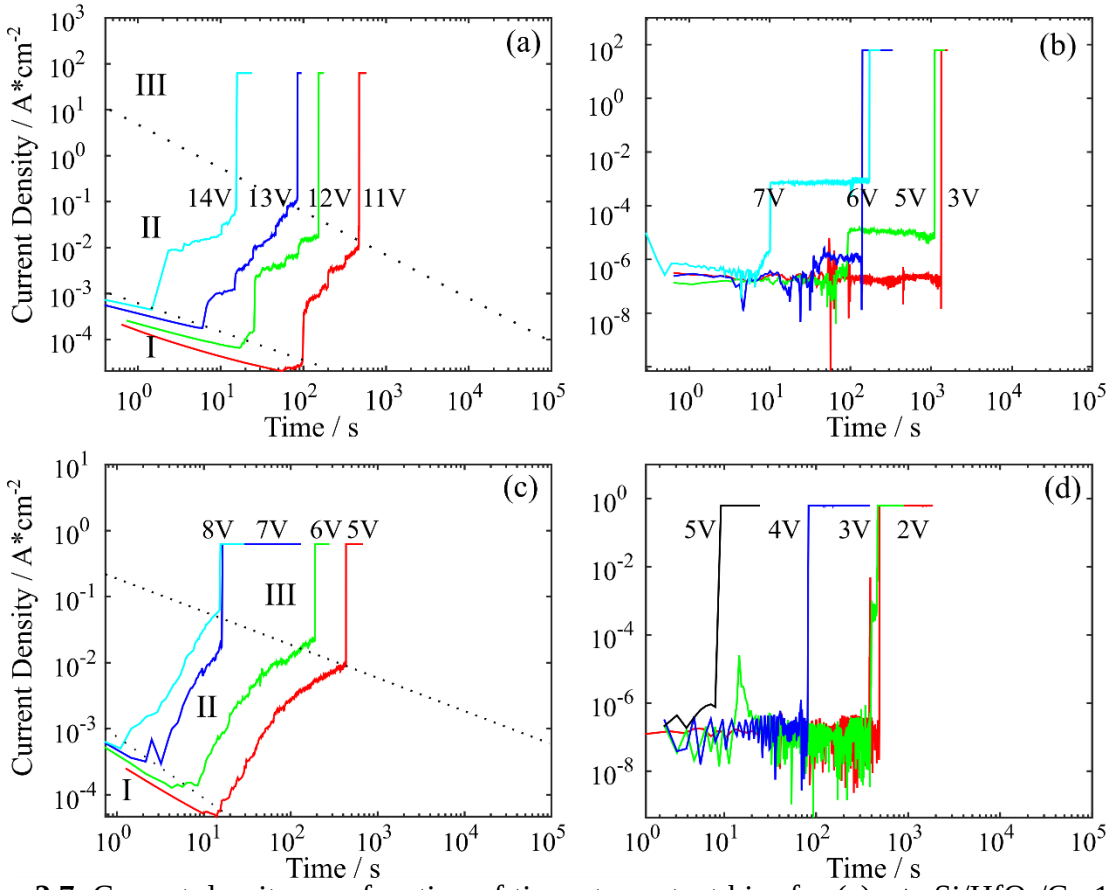

Figure 2.7. Current density as a function of time at constant bias for (a) p+ Si/HfO_2/Cu 100 ºC /400 ºC (amorphous) (b) p+ Si/HfO_2/Cu 250 ºC /400 ºC (polycrystalline) (c) TiN/HfO_2/Cu 100 ºC /400 ºC (amorphous), and (d) TiN/HfO_2/Cu 250 ºC /400 ºC (polycrystalline) devices. Regimes I – III of the current evolution are delineated with dashed lines.

Regime II commences at t_{begin}, when current first begins to increase, and is now considered a transient forming current. The literature generally describes this current transient as an increase in electronic hopping (Poole-Frenkel conduction) or tunneling between trap sites as new defects are generated in the film [35]. The removal of a voltage bias for 1800 s intervals during progressive breakdown under positive constant voltage bias does not cause electronic current to decay (Fig. 2.8b). Progressive breakdown is therefore apparently caused by the permanent accumulation of

defects in the film, which are not relaxed or removed by diffusion or thermal gradients in absence of the electric field.

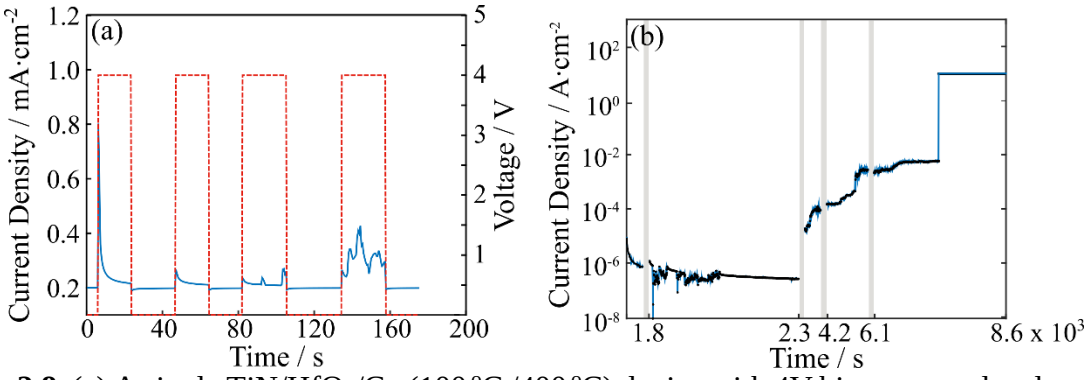

Figure 2.8. (a) A single TiN/HfO_2/Cu (100 ºC /400 ºC) device with 4V bias removed and reapplied at 20 second intervals during the Regime I current decay. Voltage is represented by the dashed red line. Current begins to show signs of filament formation beginning around 100s. (b) Current evolution over time for a single 40 µm TiN/HfO_2/Cu (100 ºC /400 ºC) device at 4V with bias removed and reapplied during the Regime II transient. Grey bars represent a 30 min. wait period during which voltage is removed.

Finally, in regime III, current increases abruptly to a low resistance state within one measurement interval (10 ms - 700 ms). This separate, 'hard breakdown' event is associated with runaway defect generation during vertical filament growth, as local electric fields and power dissipation increase between the growing filament front and the anode[1]. In some cases, current drops below the compliance limit in a 'self-healing' phenomenon that has been observed previously[36, 37]. These leakage current and forming current profiles indicate that filament forming in amorphous films involves the gradual, irreversible, accumulation of defects, the time-scale of which is independent of the initial defect concentration in the films. This 'progressive breakdown' is then followed by a separate, rapid filament forming event.

In the majority of polycrystalline films, forming is abrupt, and no measureable leakage or forming current is detected above the noise floor of the system (~10^{-12} A) until reaching a critical time ($t_{begin} = t_{form}$) at which a conductive pathway forms. In some devices deposited on p+ Si (Fig. 2.7d), an intermediate current state below the threshold current is abruptly reached and exists for some period of time before the final filament forming event ($t_{begin} \neq t_{form}$). As exception to this abrupt forming behavior, TiN/HfO_2/Cu devices where HfO_2 was deposited at 250 °C and annealed at 600 °C, demonstrate progressive forming as previously described for amorphous films. Polycrystalline devices deposited above 250 °C, therefore, show no leakage current, but demonstrate a range of forming transient current behaviors, with the majority of devices forming abruptly. In general, two major differences exist between the transient current signals of amorphous and polycrystalline oxide devices under positive constant voltage bias: (1) amorphous films show an initial current decay related to deposition at 100 °C and filling of interfacial charge states, and (2) cumulative internal increase in conductivity is observed in amorphous films, whereas conductivity increases abruptly in polycrystalline films.

Furthermore, current evolution shows asymmetry with bias polarity. Under large negative bias (> -12 V), leakage current (> 1 nA) is observed in both polycrystalline and amorphous films, regardless of deposition temperature. However, the time constant for leakage current decay is much longer in amorphous films than in polycrystalline films, again confirming high concentration of charge traps in amorphous films. Moreover, in both TiN/HfO_2/Cu and p+ Si/HfO_2/Cu devices, forming transients are abrupt in amorphous films and progressive in polycrystalline films under negative bias. The shift of forming current behavior between positive and negative constant bias may be related to the identity of the defect species involved in filament forming.

2.3.6 Filament Forming Under Bias Sweeps

Forming of conductive filaments was also studied under a positive voltage sweep with a constant 0.1 V/s sweep rate, and results confirm trends in susceptibility to breakdown among microstructural conditions (Fig. 2.9). Critical voltages are defined as V_{start}, the point at which current begins to increase above the noise floor, and V_{form}, the voltage at which current abruptly increases to the compliance current. Under a positive bias, the dynamic breakdown field (given by V_{form}/d_{HfO2}, where d_{HfO2} = 30 nm) is about 1.0 to 2.6 MV/cm in TiN/HfO_2/Cu devices and 1.0 to 4.5 MV/cm in p+ Si/HfO_2/Cu devices. In voltage sweep experiments, no significant differences in V_{form} are observed between microstructures for devices deposited on TiN, while for p+ Si/HfO_2/Cu devices, V_{form} in amorphous HfO_2 films significantly exceeds V_{form} in crystalline HfO_2 films (Fig. 2.9). Consistent with constant bias tests, current increases abruptly in the case of crystalline films ($V_{start} = V_{form}$), whereas a gradual transient increase of current is observed in the case of amorphous films (V_{start} ~0.5 to 1 V $\neq V_{form}$). This behavior is observed regardless of bottom contact. However, leakage current transients and forming current transients cannot be separated during a voltage sweep, so that forming under constant bias offers the most complete understanding of transient forming processes.

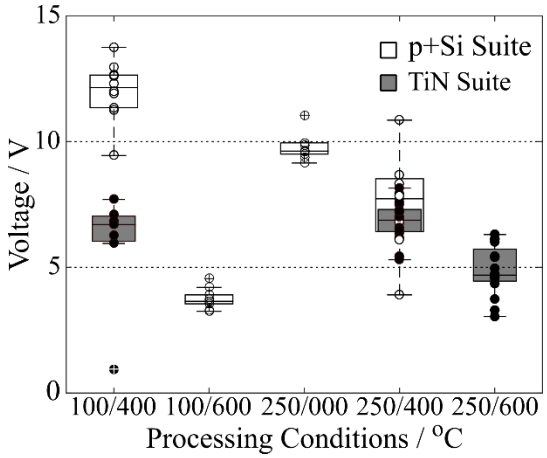

Figure 2.9. V_{form} for 40 µm edge length TiN/HfO_2/Cu (solid grey boxes) and p+ Si/HfO_2/Cu devices (empty boxes) with 0.1 V/s sweep rate.

2.4 Discussion

2.4.1 Control of Crystallinity and Oxide Texture in ALD Films

While crystallinity of HfO_2 films generally increases with thermal budget on all substrates, the degree of $(\bar{1}11)$ orientation obtained in each substrate suite shows a complicated dependence on substrate crystallinity and initial ALD growth temperature, in keeping with previous studies [23, 38, 39]. In this study, the clearest thermal dependence of texture development is seen during HfO_2 deposition on Si/a-SiO_2 substrates. While diffraction peaks from crystalline HfO_2 were not observed in as deposited ALD films grown at either low (100 °C) or high (250 °C) temperatures, identical post-deposition annealing resulted in a greater degree of orientation in the low-temperature growth case (100 °C) than in the high-temperature growth case (250 °C) (Fig. 2.1; Table 2.1). Thus, we infer that initial growth temperature impacts the internal HfO_2 structure, but to a degree that was not apparent using a laboratory XRD system. Such an observation could be caused by either a very limited extent of crystallinity (<1 vol.%) or by nanoscale crystallization

which could result in substantial peak broadening; in both cases, diffracted intensity from thin films could be difficult to distinguish from background, especially at the low scattering intensities observed in these 30 nm thick films.

We hypothesize that during high temperature growth, incipient HfO_2 nuclei form in random orientations; further annealing of this structure would result in growth of these nuclei, and random polycrystalline orientations. Previous studies of in situ RHEED growth monitoring of HfO_2 ALD growth have reported crystallite growth beginning at 300 ^oC using $HfCl_4$ and H_2O precursors, once a certain critical film thickness of 5 – 30 nm has been achieved [39]. In contrast, nucleation is kinetically limited at lower temperatures such that HfO_2 nuclei do not form until higher temperature post-deposition anneals. In this latter case, it is not surprising that nucleation occurs preferentially at lower-energy configurations. First-principles calculations have shown that the $(\bar{1}11)$ basal plane orientation constitutes that of the lowest surface energy, suggesting that nucleation at the substrate/HfO_2 interface with $(\bar{1}11)$ orientation is favorable[40]. Importantly, a competitive growth region is not visible in HRTEM in either oriented or randomly oriented polycrystalline films (Fig. 2.3), further suggesting that texture develops from the growth of oriented nuclei at the substrate/film interface rather than through faster growth rates along preferred directions.

The smaller degree of $(\bar{1}11)$ texture in HfO_2 films grown on crystalline p+ Si or TiN substrates suggests that microstructure development additionally depends on interfacial energies between HfO_2 and the underlying substrate. This observation supports the previous hypothesis that growth of oriented films results from preferred orientation of nuclei at the film/substrate interface, as changing of the underlying substrate would not be expected to influence nucleation throughout the film thickness. Thus, it seems likely that the interfacial energy between an amorphous SiO_2

substrate and HfO_2 is more favorable for nucleation of $(\bar{1}11)$ oriented nuclei than on other crystalline substrates.

2.4.2 Filament Forming Kinetics under Constant Bias

HRTEM studies with combined elemental mapping have confirmed that breakdown under positive bias in PMC's is connected to the injection of metallic ions from the electrode into the film [8, 31, 41, 42]. Under negative bias, it has been verified that oxygen species are the dominant defect type, which also condense into a conductive path through the dielectric layer[12, 30] [28]. Although both processes are of technological importance, we focus primarily on copper filament forming under positive bias, as inducing copper filaments reflects standard PMC operation. In order to unravel the respective roles of oxide microstructure and device interface properties toward filament forming kinetics, we consider a phenomenological model in which filament forming is reduced to four, spatially localized, electrochemical events [43]. (1) The copper electrode is oxidized, (2) copper cations migrate under the induced electric field across the dielectric layer to the cathode, where (3) copper cations are reduced. (4) Finally, an elemental copper filament nucleates and grows to short the cell, completing a high resistance state (HRS) to low resistance state (LRS) transition.

Any of these spatially separated processes may be limiting or co-limiting. In particular, the role of the oxide may be to control drift mobility of copper cations across the HfO_2 layer under high electric fields; this mobility would be intrinsically dissimilar in amorphous versus polycrystalline oxide films. Additionally, either top or bottom interfacial roughness may serve to geometrically enhance the local electric field strength and contribute to increased defect migration rates. Conversely, kinetics of the reduction reaction (e- transfer between Cu^+ and the bottom electrodes) should be controlled by the oxide/electrode interface where the over-potential makes

the reaction thermodynamically favorable (assuming a linear potential drop across the film). Finally, the nucleation of copper filaments is controlled by surface energies of the bottom electrode/oxide interface. Because the kinetics of the electrochemical reduction reaction are not directly observable in this experimental set-up, we consider the roles of oxide microstructure (crystallinity, degree of orientation, and average grain size) and electrode roughness profiles in determining overall conductive filament forming kinetics.

2.4.2.1 Role of Amorphous and Crystalline Oxide Layers

Because breakdown occurred on at least an order of magnitude longer time scale for amorphous devices than for polycrystalline HfO_2 devices, regardless of substrate, we consider that filament formation in amorphous films is limited by the migration of mobile ionic species (presumably copper cations under positive bias). In contrast, formation occurs on a shorter time scale in all polycrystalline films with the introduction of fast diffusion paths along grains boundaries (Fig. 2.10). Longer forming times in amorphous films are observed under both a positive and a negative bias condition (Fig. 2.6), pointing to a similar mechanism of kinetic limitation, albeit occurring at a higher threshold voltage under negative bias. Presumably, copper cations have a lower activation energy for migration in HfO_2 than do oxygen vacancies.

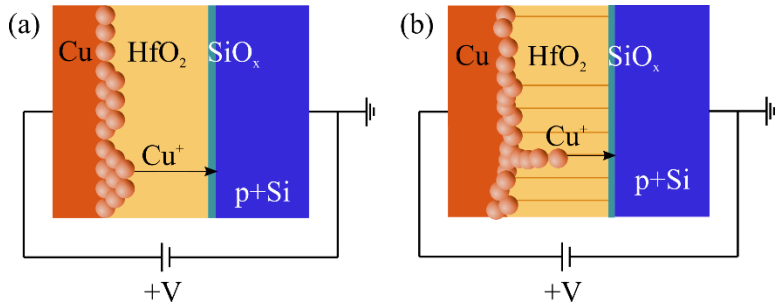

Figure 2.10. A schematic of the forming process under positive bias is given for (a) amorphous films and for (b) polycrystalline films, in which copper cations are proposed to migrate along grain boundary pathways illustrated by brown lines.

These results are consistent with dielectric breakdown studies of high-k layers in MOS capacitors and in thin gate-oxide layers; crystallization of HfO_2 is widely observed to lead to acceleration of breakdown, often attributed to defect localization along grain boundaries [29, 44-46]. Silicates and nitrides of HfO_2 are frequently introduced to suppress crystallization during subsequent thermal treatments in silicon based device fabrication [44, 47]. Here, we consider that introduction of grain boundaries provides a pathway along which mobility of copper cations and oxygen vacancies is enhanced, and in fact, accelerates device forming kinetics.

The exponential acceleration of breakdown at higher voltages (Fig. 2.6) that is observed in all films may be explained by the Mott-Gurney equation, which describes electric field ($\vec{E}$) enhanced mobility (μ_i) of ionic defects hopping between potential wells across the oxide with an activation energy, U_A [48].

$$\mu_i = q l_x z f v_o \exp\left(-\frac{U_A}{kT}\right) \sinh\left(\frac{l_x q \vec{E}}{2kT}\right) \tag{2.1a}$$

$$\mu_i = \begin{cases} q l_x z f v_o \exp\left(-\frac{U_A}{kT}\right) & l_x q\vec{E} \ll kT \\ q l_x z f v_o \exp\left(-\frac{U_A}{kT}\right) \exp\left(-\frac{l_x q \vec{E}}{2kT}\right) & l_x q\vec{E} \gg kT \end{cases} \tag{2.1b}.$$

Here, f is a geometric factor, q is the elemental charge, z is the formal charge of the ionic species, v_o is the atomic jump attempt frequency, k is Boltzman's constant, T = 300 K, and l_x is the average distance that an ionic species must hop in the direction of the field. In the case of high-field experiments described herein, application of an electric field lowers the activation energy barrier U_A for an ion to jump into neighboring vacancy sites in the direction of the field by $\frac{-q\vec{E}l_x}{2}$, far below the value at which thermal hopping in the opposite direction is significant. Therefore, the expression reduces to an exponential dependence of ionic mobility on electric field. Writing the expression for ionic current, i, as a function of ionic defect density c_i, the formal charge of the defect, z, and the mobility of the ionic defect, μ_i

$$i = c_i z F \mu_i \vec{E} \qquad (2.2),$$

and integrating generates an exponential dependence of t_{form} on average $\vec{E}$ field that is observed in all cases;

$$t_{form} = Q_{form} \cdot \frac{1}{A\mu_0} \vec{E} \exp\left(-\frac{l_x q \vec{E}}{2kT}\right) \qquad (2.3).$$

Equation 3 assumes some threshold behavior for a minimum quantity of migrated ionic species (Q_{form}) before conductive filaments are formed i.e. some minimum number of cations needed to compose a conductive pathway. The mobility under $\vec{E} = 0$ is given by μ_0. Moreover, the charge density of the species, c_i, is assumed to be constant, although additional carriers may be created under high fields.

2.4.2.2 Role of Oxide Texture and Grain Size

Differences in t_{form} within polycrystalline films deposited on the same substrate (Fig. 2.6) may be related to other oxide microstructural properties, including degree of orientation, and average grain size. Namely, the degree of HfO_2 crystalline orientation is correlated to changes in

t_{form} data in p+ Si/HfO_2 and TiN/HfO_2 films. As the degree of oxide orientation increases with thermal budget in p+ Si/HfO_2 films (Fig. 2.2), forming time increases (Fig. 2.6a). Polycrystalline TiN/HfO_2 films, processed at either 250 °C/400 °C or 250 °C/600 °C, show equivalent degrees of oxide orientation (Table 1), correlated to equivalent values of t_{form} (Fig. 2.6b). In view of a random distribution of grain boundaries, the probability of possessing a boundary with low activation energy for ion migration is higher in randomly oriented polycrystalline films than in oriented films. This view is further supported by the observation of area scaling of t_{form} in TiN/HfO_2/Cu devices. The probability of finding an energetically favorable grain boundary increases with the contact area of the top electrode. Accordingly, breakdown times are an order of magnitude shorter in 0.04 mm^2 devices compared against 0.0016 mm^2 devices (Fig. A-1b). Variations in average grain size do not seem to be well correlated with the order of forming times within both p+ Si/HfO_2/Cu and TiN/HfO_2/Cu devices, since differences in grain size are not significant between films annealed at 400 °C or 600 °C in either the p+ Si/HfO_2 or TiN/HfO_2 suite (Fig. 2.5b).

2.4.3 Role of Device Interfaces

Two key observations in this study cannot be explained by bulk oxide crystallinity and degree of orientation: (1) t_{form} data are uniformly shorter in TiN/HfO_2/Cu devices than in p+ Si/HfO_2/Cu devices, and (2) significant separation in t_{form} data between polycrystalline p+ Si/HfO_2 films is observed under positive bias but not under negative bias, while the opposite is true for TiN/HfO_2 films (Fig. 2.5). These observations of asymmetry under bias application and between bottom electrode suites indicate some dependence on other oxide and interfacial characteristics, which include non-stoichiometry, interfacial roughness, and interfacial thickness. Within the bulk, HfO_x non-stoichiometry has been previously shown to be a critical variable in anionic resistance switches [1, 12]. ALD growth techniques typically result in fully stoichiometric films; however,

TiN bottom electrodes have a high oxygen affinity and vacancies created during forming bias application may become localized at the TiN/HfO_2 interface, speeding forming kinetics. Trends in top or bottom interfacial roughness are not sufficient to explain trends in t_{form} data. In all cases, the mean aspect ratio (S_q/mean grain diameter) of a granular protrusion is < 1, so that the multiplicative electric field enhancement factor, β, derived in [49] from Maxwell's equations around a hemispheroid protrusion, is ~1. Moreover, devices with very smooth (S_q < 1 nm) top and bottom interfaces (p+ Si/HfO_2/Cu 100 °C/600 °C), in which field enhancement should be minimized, demonstrate the fastest forming times, in opposition to what is given from Equation 3. Finally, SiO_x interlayers are shown by XRR of Si/SiO_x/HfO_2 films to vary little in thickness between thermal processing conditions, so that significant changes in average E-field and t_{form} are not expected. Therefore, it is likely that t_{form} asymmetry under bias polarity and with regard to TiN or p+ Si bottom electrodes is a complicated function of oxide chemistry, rather than physical electrode roughness or film thickness.

2.4.4 Filament Forming Statistics

Inter-device variability in t_{form} is generally equivalent in films regardless of thermal processing condition (Fig. A-3). The polycrystalline p+ Si/HfO_2 film deposited at 250 °C and annealed at 400 °C, shows an anomalously large relative standard deviation in t_{form}. The physical source of inter-device variability in t_{form} distributions is unlikely to be deviations in film thickness (σ = 0.2 nm over 1 cm^2 area), but might rather stem from a distribution of transport path energies. Assuming that cation migration is the rate limiting step in filament formation, a wider distribution in transport path energies leads to a wider distribution in t_{form}. However, because trends in relative standard deviation of t_{form} data are not separated on the basis of processing condition, correlations with physical properties of crystallinity or interfacial roughness cannot be made.

2.5 Conclusions

We demonstrate the ability to vary HfO_2 microstructure with combinations of growth temperatures, post-deposition annealing temperatures, and substrates for HfO_2 based PMCs. Furthermore, we investigate the importance of the resultant oxide microstructure on filament forming kinetics of TiN/HfO_2/Cu and p+ Si/HfO_2/Cu devices under either a positive or a negative constant bias. Low growth deposition and annealing at 400 ^oC results in amorphous HfO_2 layers when deposited on p+ Si or TiN. Higher temperature growth at 250 $^\circ C$ and subsequent annealing at 400 ^oC or 600 ^oC results in oriented polycrystalline films. The possibility for growing highly $(\bar{1}11)$ textured polycrystalline HfO_2 films is demonstrated with a combined low growth temperature (100 ^oC) and high temperature post-deposition anneal (600 ^oC) on Si/a-SiO_2 substrates. The preferred nucleation of $(\bar{1}11)$ oriented crystallites at the SiO_2/HfO_2 surface is thought to contribute to the development of film texture. Our experimental findings indicate that the crystalline nature of the oxide layer primarily determines the kinetics of filament forming, and that filament forming is significantly slower in amorphous films than in polycrystalline films. Differences in breakdown times within a subset of polycrystalline films are apparent under positive bias in films deposited on p+ Si, and may be related to the degree of oxide orientation. Interfacial roughness is not found to play a significant role in filament forming kinetics in these films. Current transients prior to final breakdown are progressive in amorphous films and abrupt/step-wise in polycrystalline films, and may signal differences in filament forming mechanisms or involvement of mixed defect species. We have identified optimal ALD growth/annealing conditions (100 °C/600 °C) for minimizing filament forming kinetics; these conditions correspond to a polycrystalline, more randomly oriented film, with smooth top and bottom interfaces. Given the significant differences between amorphous and polycrystalline films in kinetics of filament

forming, it is reasonable to expect that inter-device/intra-device cycle endurance and switching parameter variability may also be dependent on oxide microstructure

2.6 References

[1] Yang J J, Strukov D B and Stewart D R 2013 Memristive devices for computing *Nature nanotechnology* **8** 13-24

[2] Park S, Noh J, Choo M-l, Sheri A M, Chang M, Kim Y-B, Kim C J, Jeon M, Lee B-G and Lee B H 2013 Nanoscale RRAM-based synaptic electronics: toward a neuromorphic computing device *Nanotechnology* **24** 384009

[3] Yu S, Wu Y, Jeyasingh R, Kuzum D and Wong H-S P 2011 An electronic synapse device based on metal oxide resistive switching memory for neuromorphic computation *Electron Devices, IEEE Transactions on* **58** 2729-37

[4] Indiveri G, Legenstein R, Deligeorgis G and Prodromakis T 2013 Integration of nanoscale memristor synapses in neuromorphic computing architectures *Nanotechnology* **24** 384010

[5] Wang Y, Liu Q, Long S, Wang W, Wang Q, Zhang M, Zhang S, Li Y, Zuo Q and Yang J 2010 Investigation of resistive switching in Cu-doped HfO2 thin film for multilevel non-volatile memory applications *Nanotechnology* **21** 045202

[6] Yu S, Wu Y and Wong H-S P 2011 Investigating the switching dynamics and multilevel capability of bipolar metal oxide resistive switching memory *Applied Physics Letters* **98** 103514

[7] Lien C, Chen Y, Lee H, Chen P, Chen F and Tsai M-J 2010 The highly scalable and reliable hafnium oxide ReRAM and its future challenges: IEEE) p 1084-7

[8] Lv H, Xu X, Liu H, Liu R, Liu Q, Banerjee W, Sun H, Long S, Li L and Liu M 2015 Evolution of conductive filament and its impact on reliability issues in oxide-electrolyte based resistive random access memory *Scientific reports* **5**

[9] Lee H, Chen Y, Chen P, Gu P, Hsu Y, Wang S, Liu W, Tsai C, Sheu S and Chiang P-C 2010 Evidence and solution of over-RESET problem for HfO x based resistive memory with sub-ns switching speed and high endurance: IEEE) p 19.7. 1-.7. 4

[10] Govoreanu B, Kar G, Chen Y, Paraschiv V, Kubicek S, Fantini A, Radu I, Goux L, Clima S and Degraeve R 2011 10× 10nm 2 Hf/HfO x crossbar resistive RAM with excellent performance, reliability and low-energy operation: IEEE) p 31.6. 1-.6. 4

[11] Tsuruoka T, Terabe K, Hasegawa T and Aono M 2010 Forming and switching mechanisms of a cation-migration-based oxide resistive memory *Nanotechnology* **21** 425205

[12] Bersuker G, Gilmer D, Veksler D, Kirsch P, Vandelli L, Padovani A, Larcher L, McKenna K, Shluger A and Iglesias V 2011 Metal oxide resistive memory switching mechanism based on conductive filament properties *Journal of Applied Physics* **110** 124518

[13] Raghavan N, Fantini A, Degraeve R, Roussel P, Goux L, Govoreanu B, Wouters D, Groeseneken G and Jurczak M 2013 Statistical insight into controlled forming and forming free stacks for HfOx RRAM *Microelectronic Engineering* **109** 177-81

[14] Rahaman S Z, Maikap S, Ray S K, Lee H-Y, Chen W-S, Chen F T, Kao M-J and Tsai M-J 2012 Record resistance ratio and bipolar/unipolar resistive switching characteristics of memory device using germanium oxide solid electrolyte *Japanese Journal of Applied Physics* **51** 04DD11

[15] Rahaman S, Maikap S, Chen W, Lee H, Chen F, Kao M and Tsai M 2012 Repeatable unipolar/bipolar resistive memory characteristics and switching mechanism using a Cu nanofilament in a GeOx film *Applied Physics Letters* **101** 073106

[16] Zhou L W, Shao X L, Li X Y, Jiang H, Chen R, Yoon K J, Kim H J, Zhang K, Zhao J and Hwang C S 2015 Interface engineering for improving reliability of resistance switching in Cu/HfO2/TiO2/Pt structure *Applied Physics Letters* **107** 072901

[17] Zhang H, Liu L, Gao B, Qiu Y, Liu X, Lu J, Han R, Kang J and Yu B 2011 Gd-doping effect on performance of HfO2 based resistive switching memory devices using implantation approach *Applied Physics Letters* **98** 042105

[18] Bertaud T, Walczyk D, Walczyk C, Kubotsch S, Sowinska M, Schroeder T, Wenger C, Vallée C, Gonon P and Mannequin C 2012 Resistive switching of HfO 2-based Metal–Insulator–Metal diodes: Impact of the top electrode material *Thin Solid Films* **520** 4551-5

[19] Lin K-L, Hou T-H, Shieh J, Lin J-H, Chou C-T and Lee Y-J 2011 Electrode dependence of filament formation in HfO2 resistive-switching memory *Journal of Applied Physics* **109** 084104

[20] Kinoshita K, Tsunoda K, Sato Y, Noshiro H, Yagaki S, Aoki M and Sugiyama Y 2008 Reduction in the reset current in a resistive random access memory consisting of NiOx brought about by reducing a parasitic capacitance *Applied Physics Letters* **93** 3506

[21] Capulong J O, Briggs B D, Bishop S M, Hovish M Q, Matyi R J and Cady N C 2012 Effect of crystallinity on endurance and switching behavior of HfO x-based resistive memory devices: IEEE) p 22-5

[22] Briggs B D, Bishop S M, Capulong J O, Hovish M Q, Matyi R J and Cady N C 2011 Comparison of HfO x-based resistive memory devices with crystalline and amorphous active layers: IEEE) p 1-2

[23] Cho M-H, Roh Y, Whang C, Jeong K, Nahm S, Ko D-H, Lee J, Lee N and Fujihara K 2002 Thermal stability and structural characteristics of HfO2 films on Si (100) grown by atomic-layer deposition *Applied physics letters* **81** 472-4

[24] Gutowski M, Jaffe J E, Liu C-L, Stoker M, Hegde R I, Rai R S and Tobin P J 2002 Thermodynamic Stability of High-K Dielectric Metal Oxides ZrO 2 and HfO 2 in Contact with Si and SiO2(vol 716): Cambridge Univ Press) p B3. 2

[25] Lee B H, Kang L, Nieh R, Qi W-J and Lee J C 2000 Thermal stability and electrical characteristics of ultrathin hafnium oxide gate dielectric reoxidized with rapid thermal annealing *Applied Physics Letters* **76** 1926-8

[26] Yu-Jian H, Yue H, Shi-Jin D, Wei Z and Ran L 2007 Electrical Characterization of Metal–Insulator–Metal Capacitors with Atomic-Layer-Deposited HfO2 Dielectrics for Radio Frequency Integrated Circuit Application *Chinese Physics Letters* **24** 2942

[27] Aguirre B, Vemuri R, Zubia D, Engelhard M H, Shutthananadan V, Bharathi K K and Ramana C V 2011 Growth, microstructure and electrical properties of sputter-deposited hafnium oxide (HfO 2) thin films grown using a HfO 2 ceramic target *Applied Surface Science* **257** 2197-202

[28] Baik H S, Kim M, Park G-S, Song S A, Varela M, Franceschetti A, Pantelides S and Pennycook S 2004 Interface structure and non-stoichiometry in HfO2 dielectrics *Applied physics letters* **85** 672-4

[29] Kim H, McIntyre P C and Saraswat K C 2003 Effects of crystallization on the electrical properties of ultrathin HfO2 dielectrics grown by atomic layer deposition *Applied physics letters* **82** 106-8

[30] Lanza M, Bersuker G, Porti M, Miranda E, Nafría M and Aymerich X 2012 Resistive switching in hafnium dioxide layers: local phenomenon at grain boundaries *Applied Physics Letters* **101** 193502

[31] Liu Q, Sun J, Lv H, Long S, Yin K, Wan N, Li Y, Sun L and Liu M 2012 Real-Time Observation on Dynamic Growth/Dissolution of Conductive Filaments in Oxide-Electrolyte-Based ReRAM *Advanced Materials* **24** 1844-9

[32] RUH R and CORFIELD P W 1970 Crystal structure of monoclinic hafnia and comparison with monoclinic zirconia *Journal of the American Ceramic Society* **53** 126-9

[33] Gusev E and D'Emic C 2003 Charge detrapping in HfO2 high-κ gate dielectric stacks *Applied physics letters* **83** 5223-5

[34] Kang L, Lee B H, Qi W-J, Jeon Y, Nieh R, Gopalan S, Onishi K and Lee J C 2000 Electrical characteristics of highly reliable ultrathin hafnium oxide gate dielectric *Electron Device Letters, IEEE* **21** 181-3

[35] Raghavan N, Pey K L and Shubhakar K 2014 High-κ dielectric breakdown in nanoscale logic devices–Scientific insight and technology impact *Microelectronics Reliability* **54** 847-60

[36] Raghavan G, Chiang C, Anders P B, Tzeng S-M, Villasol R, Bai G, Bohr M and Fraser D B 1995 Diffusion of copper through dielectric films under bias temperature stress *Thin Solid Films* **262** 168-76

[37] Gonon P, Mougenot M, Vallée C, Jorel C, Jousseaume V, Grampeix H and El Kamel F 2010 Resistance switching in HfO2 metal-insulator-metal devices *Journal of Applied Physics* **107** 074507

[38] Bohra F, Jiang B and Zuo J-M 2007 Textured crystallization of ultrathin hafnium oxide films on silicon substrate

[39] Aarik J, Aidla A, Mändar H, Sammelselg V and Uustare T 2000 Texture development in nanocrystalline hafnium dioxide thin films grown by atomic layer deposition *Journal of Crystal Growth* **220** 105-13

[40] Mukhopadhyay A B, Sanz J F and Musgrave C B 2006 First-principles calculations of structural and electronic properties of monoclinic hafnia surfaces *Physical Review B* **73** 115330

[41] Wu X, Pey K, Zhang G, Bai P, Li X, Liu W and Raghavan N 2010 Electrode material dependent breakdown and recovery in advanced high-kappa gate stacks *Applied Physics Letters* **96** 2903

[42] Pey K, Raghavan N, Liu W, Wu X, Shubhakar K and Bosman M 2013 Real-time analysis of ultra-thin gate dielectric breakdown and recovery-A reality: IEEE) p 319-31

[43] Waser R, Dittmann R, Staikov G and Szot K 2009 Redox-based resistive switching memories−nanoionic mechanisms, prospects, and challenges *Advanced Materials* **21** 2632-63

[44] Schroeder U, Weinreich W, Erben E, Mueller J, Wilde L, Heitmann J, Agaiby R, Zhou D, Jegert G and Kersch A 2009 Detailed Correlation of Electrical and Breakdown Characteristics to the Structural Properties of ALD Grown HfO2-and ZrO2-based Capacitor Dielectrics *ECS Transactions* **25** 357-66

[45] Lanza M, Zhang K, Porti M, Nafria M, Shen Z, Liu L, Kang J, Gilmer D and Bersuker G 2012 Grain boundaries as preferential sites for resistive switching in the HfO2 resistive random access memory structures *Applied Physics Letters* **100** 123508

[46] Raghavan N, Pey K L, Shubhakar K, Wu X, Liu W and Bosman M 2012 Role of grain boundary percolative defects and localized trap generation on the reliability statistics of high-κ gate dielectric stacks: IEEE) p 6A. 1.-6A. 1.11

[47] Seong N-J, Lee W-J and Yoon S-G 2006 Structural and electrical characterizations of ultrathin HfO2 gate dielectrics treated by nitrogen-plasma atmosphere *Journal of Vacuum Science & Technology B* **24** 312-5

[48] O'Dwyer J J 1973 *The theory of electrical conduction and breakdown in solid dielectrics*: Clarendon Press)

[49] Hourdakis E, Bryant G W and Zimmerman N M 2006 Electrical breakdown in the microscale: Testing the standard theory *Journal of applied physics* **100** 123306

3. CONDUCTIVE FILAMENT SHAPE IN HfO_2 PROGRAMMABLE METALLIZATION CELLS UNDER A RANGE OF FORMING VOLTAGES

3.1 Introduction

Despite promising performance in areas of cycle endurance [1, 2], scaling [3], and power use [4], the possible technological integration of electrochemical metallization cells in neuromorphic computing has been curtailed by high levels of variability in their electrical switching parameters between cycles and between devices [5]. Fundamentally, this variability stems from the non-uniformity in the shape, volume, and composition of the conducting filaments that determine the device's non-volatile resistance state, as well as their continuing evolution over numerous set and reset cycles. These filaments are formed as the result of high electric fields (>10 MV cm^{-1}) which are believed to drive migration of positively charged ions from the redox active metal electrode across the dielectric layer to the inert bottom electrode, shorting the dielectric layer, although current is limited at a set compliance value (I_{cc}) [6]. As an additional complication, this process of "arrested dielectic breakdown" exists on a continuum of field driven and thermally driven dielectric breakdown, and high thermal gradients exist due to joule heating in nm scale cross-sections within ns time-scales (i.e., near adiabatic conditions) [5-8]. In the extreme, this thermal pulse can result in irreversible broadening of the filament, hard-dielectric breakdown and thus device failure [1].

Taken together, this involvement of several driving forces and their interaction with defects both in the dielectric layer as well as the electrode materials presents a complicated practical problem to identify the major determinant of filament variability or critical interface/device layer to engineer. Several studies have made use of analytical solutions [9-12] or finite element modeling

[13] in order to understand the complicated interplay of electrical field, thermal joule heating, redox reactions, and materials defects in determining the kinetics and variability of resistance switching. In particular, the RESET operation in which the filament is dissolved has presented large degrees of device variability and challenge to model [14-16]. For many of these models, the explicit shape of the filament, whether conical, cylindrical, or hour-glass must be assumed at some step [17]. In the framework of the widely accepted phenomenological model [18], both lateral and transverse ion migration is limited in oxides, and as ions travel from anode to cathode, the electric field concentrates around the tip of the growing filament driving increased ion flux in that area, forming a conical shape with its base at the anode. However, a growing body of experimental work concerning direct imaging of formed filaments show that while there are several reports of cone shaped filaments [19-23], hourglasses [24], branched filaments [25], and larger more cylindrical shapes [26] have also been reported. Overall, the number of studies concerning direct imaging of filament area are relatively few when compared against the vast body of work on device level characterization. This dearth of reports stems from the fact that basic characterization of conductive filament (CF) shape is non-trivial, principally due to the challenging nature of studying nanometer scaled conductive defects within the several layer device matrix. However, knowledge of filament morphology resulting from direct characterization of filament shape is essential to solve critical ongoing challenges of device switching variability.

In order to characterize these challenging structures, studies have relied on two of the most accessible nanoscale techniques, TEM and conductive atomic force microscopy (c-AFM). Studies utilizing both in-situ TEM and TEM cross-sections following device programming have revealed that conductive filaments in electrochemical metallization systems are indeed composed of metal (although the ionization state is unknown), and the conductive area seems to be enriched in metal

as the device approaches failure[1, 27]. However, in the *in-situ* studies, the exposure of the device area may introduce artificial electric field distributions as well as artificial defect concentrations associated with the exposed surface. Likewise, moisture has been shown to be an important element in resistive switching[28], and is by nature, excluded from TEM experiments. A particularly interesting aspect of filament growth has been generated by high-resolution TEM work that shows build-up of metallic clusters nucleated within the dielectric layer [29]. The first observation of these Ag or Cu clusters, and the associated growth mode in which the filament grows from anode to cathode, opposes the theoretical frame-work of field-drive ion migration followed by electro-chemical reduction at the device cathode [27]. This work has generated some debate as to whether metal ions can in fact be reduced within the bulk of the dielectric, versus nucleating and growing a filament only once reaching the cathode [30]. Although TEM has been used to reveal previously unpredicted growth modes of conductive filaments as well as show a build-up of metal within failed filaments, only a 2D slice of the filament is generated in these experiments, and the true 3D shape remains an open question.

Instead, conductive atomic force microscopy (c-AFM) studies have proven to be especially promising by virtue of combining a high sensitivity circuit and the capability of tracking microscale features with nanometer scale resolution. These studies include work in which the top electrode of a device has been removed post programming, and a 2D scan of the surface used to reveal conductive pathways (composed of either oxygen vacancies or metal atoms) through the insulating oxide matrix [31-35]. Testing between amorphous and polycrystalline materials shows that conductive spots are preferentially localized at grain boundaries, and are indeed more readily set/reset than their larger, randomly dispersed filaments in amorphous films[33, 36]. While these studies yield interesting information, they present only a snap shot after each programming step

has been executed. To gain an understanding of the evolution over operation sequence, the tip has been used as a mobile 100 nm^2 electrode, to which a voltage is applied as it scans over the surface of the oxide [25, 37-40]. However, these experiments often involve artificially concentrated electric fields around the sharp AFM tip, as well as read voltages high enough to influence filament forming/rupturing and program voltages < 10 V, which may be too low to influence forming in some cases.

An especially innovative alternative applies c-AFM with a doped diamond tip used both as a scalpel and a traditional conductive AFM tip [22, 41]. This technique yields the ability to create a 3D tomogram of conductive filaments with nm scale vertical and lateral resolution. Using this technique, both inverted cones [22] and hourglass filament shapes [24] have been demonstrated. Additionally, it has been determined that reset resistance states are correlated to exceedingly narrow (<10 nm radius) tunneling gaps between the filament end and the top electrode [42]. Therefore, although c-AFM suffers from an inability to collect chemical information, a full analysis of filament shape in devices formed under less artificial conditions is possible using this 3D "scalpel" technique. As yet, this promising technique has been applied in only a small subset of dielectric films out of the vast possibilities for oxide chemistry and microstructure. Moreover, because of the time consuming nature of these experiments, it is difficult to establish inter-device variability in filament shape.

In this work, the 3D scalpel technique is used to investigate conductive filament shape variability in (3) p+Si/HfO_2/Cu devices formed under identical electrical stress conditions. Additionally, the filament shape in thick (30 nm) and thin (10 nm) HfO_2 films is obtained and shows a high degree of variability between branched, inverse conical, and conical shapes. Here, a low forming voltage/electric field attainable only in polycrystalline HfO_2 films is used to limit

overshoot of the set compliance current, as forming at higher voltages demonstrates an increasing spectrum of thermal damage to both dielectric and top electrode layers. The relative impacts of forming voltage (V_{form}), electric field, and dielectric microstructure on thermal damage mechanisms was explored using a 2D device deconstruction experiment, and demonstrated that V_{form} is the principal determinant of compliance current (I_{cc}) overshoot and therefore thermal damage area, while oxide microstructure can control damage location. Notably, electrical bias conditions were chosen as representative of the forming conditions commonly employed in device scale variability studies, and the impact of those conditions on the material integrity of the device which may be hidden under thick top electrodes is revealed. These results combined with the observed variability in shape (instead of merely volume) suggests that even in oxide systems in which ion migration is kinetically limited, thermal contributions to lateral ion diffusion as well as oxide defects may play a larger role than earlier surmised in determining conductive filament shape under the given electrical bias conditions.

3.2 Methods

3.2.1 Device Fabrication

p+Si/HfO_2/Cu devices were fabricated on highly doped <100> p+Si substrates purchased from NovaElectronics (0.001 Ω·m). Substrates were first cleaned in a buffered oxide etch solution (5:1 HF) for 30 s before loading in Cambridge Nanotech Fijii atomic layer deposition (ALD) chamber. TMAHf was used as the Hf precursor and an O2 plasma (300 W) was used as the oxidant. Sixty growth cycles consisting of a 20 s TMAHf pulse, 30 N_2 purge, 20 s O_2 plasma pulse, and N_2 purge were carried out at either 100 °C or 250 °C to deposit 30 nm of HfO_2 uniformly on the p+Si substrate. Wafers were post-deposition annealed at 400 °C or 600 °C for one hour to induce

crystallization in the HfO_2 films. XRD characterization was performed to assess crystal structure of the films and is reported in a previous publication [43].

Resistance switching devices were defined photo-lithographically (Fig. 3.1) after cleaning the HfO_2 surface in acetone, methanol, isopropyl alcohol, and DI H_2O. To provide an isolation layer, a SiO_2 film (70 nm) was sputtered from a SiO_2 target (99.99% purity) in an Ar(g) plasma with 4% O_2 at a total pressure of $3 \cdot 10^{-3}$ Torr at 500 . Base pressure in the deposition system was below $5.0 \cdot 10^{-6}$ Torr and the target was cleaned for 20 min prior to deposition. The resulting deposition rate was about 0.2 Å/s. A Cr film (10 nm) was subsequently deposited as an adhesion layer by e-beam evaporation. After lift-off in acetone and photoresist stripper, patterns for the copper electrodes were photo-lithographically defined. Copper was e-beam deposited (25 nm) across the edge of the SiO_2 pads to create 20 x 20 µm devices connected by a thin (5 µm wide) line to 400 x 400 µm bond pads, again by lift-off. Copper electrodes were intentionally thin (25 nm) in order to facilitate further experiments in which the copper electrode might be physically removed.

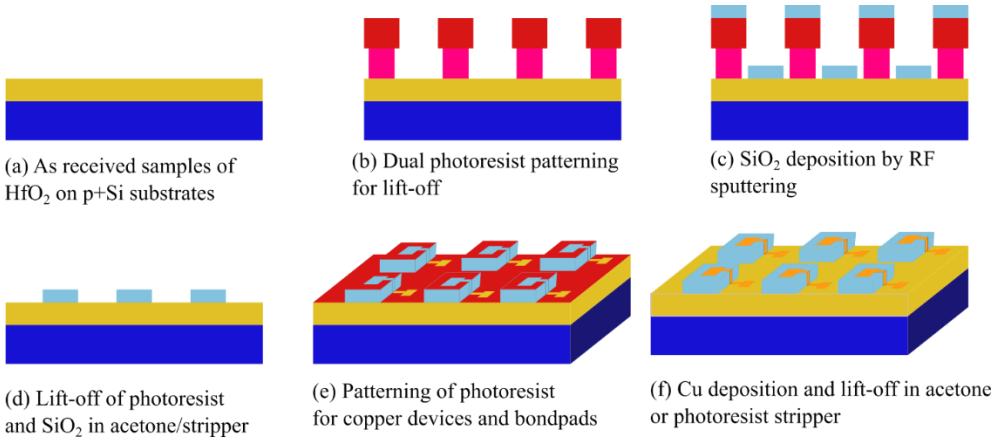

Figure 3.1. Deposition and photolithographic sequence for fabrication of p+Si/HfO_2/Cu devices. Red and pink layers indicate photoresist, yellow layers indicated HfO_2, orange layers Cu, light blue layers SiO_2, and blue layers p+Si substrates.

3.2.2 Electrical Characterization

Devices were formed at a range of 3 to15 V under constant bias stress using a Keithley 4200 SCS parameter analyzer. A positive bias was applied to copper top electrode using a W probe tip (1 µm radius) applied to the bond pad and the bottom p+Si electrode was grounded in order to drive copper migration into the HfO_2 film. A compliance current of 100 µA was employed to limit destructive breakdown of the HfO_2 film. However, an overshoot current did flow through the cell for at least several 100 µs due to the time lag of the 4200 SCS internal circuitry.

3.2.3 Atomic Force Microscopy

Following electrical characterization, atomic force microscopic (AFM) imaging was used to characterize damage morphologies both before and after a wet chemical etch of the copper top electrode. First, tapping mode images were taken of the device top electrode using a Bruker Icon AFM with a scan rate of 0.5 Hz, and resolution of 384 pts/line. Any visible defects were imaged

at higher magnification. The top electrode was then chemically etched away in a dilute 0.5 % $FeCl_3$ (CE-100 Transene Electronic Chemicals) solution for 20 s. Post-etch, the area of bare HfO_2 where the top electrode had previously been located was imaged in conductive atomic force microscopy (c-AFM) mode using a conductive Pt-Ir AFM tip (MikroMasch HQ: NSC18/Pt, fo = 75 kHz, k = 2.8 N/m, coated tip radius < 30 nm) or a doped diamond-coated tip (Bruker DDESP-V2, fo = 400 kHz, k = 80 N/m) to obtain conductivity maps. A -5.0 mV bias was applied at the stage to which the sample was electrically connected via Ag paste, and the sensitivity range was 1 nA/V with signal saturation at 12 nA. With these settings, the noise floor of the measurement circuit was approximately 5.0 pA. AFM data was corrected for planar offsets using Gwyddion software package. Compilation of 2D scans into a 3D tomogram was accomplished using a cross-correlation function in MATLAB to sequentially align scans correcting for thermal drift, as well as including the topography data in the conductive signal of each scan.

3.2.4 Wet Etch

We used a selective wet etch process to remove the Cu top electrode, revealing the dilectric layer, as well as damage in that layer. A solution of 35 wt% FeCl3 and 6 wt% HCl (CE-100 Transene Chemicals) was serially diluted to 0.1 wt% FeCl3 and the devices, with alignment marks protected with photoresist, were immersed in solution for 20 s until Cu was no longer optically visible. To verify the selectivity of the Cu etchant, AFM topography scans were performed on a region of patterned material that was partially protected by photolithography during wet etching. We investigated regions that 1) were protected by photoresist and therefore not exposed to Cu etchant, 2) bare HfO_2 films that were exposed to Cu etchant, and 3) HfO_2 films underlying Cu top electrodes which were exposed by the etching procedure. A comparison of these regions illustrated nearly complete removal of Cu electrode in the protected region coupled with no discernible

difference in HfO_2 film thickness (to the sub-nm resolution) or average surface roughness. No occurrence of localized etch pits in the underlying HfO_2 films was observed.

3.3 Results

3.3.1 Film Microstructure

Suites of HfO_2 films varying in thickness (5 nm, 10 nm, 15 nm, and 30 nm) and growth conditions were created to test effects of electric field and film microstructure. Growth conditions used to control film microstructure were varied between two ALD deposition temperatures (100 ^oC or 250 ^oC) and three post-deposition annealing conditions (no anneal, 400 ^oC, and 600 ^oC). Detailed microstructural results of these thermal processing conditions in 30 nm HfO_2 films are reported elsewhere [43], but in general resulted in a range of microstructure from amorphous to polycrystalline films with varying degrees of $(\bar{1}11)$ orientation with increasing thermal budget.

Degree of HfO_2 crystallinity and texture was observed to vary as a function of ALD growth temperature, post-deposition annealing temperatures, and film thickness (Table 1). In all cases, crystalline HfO_2 was observed in the stable low-temperature monoclinic Baddelyite structure ($P2_1/c$, #14). 30 nm thick films grown at 100 °C and annealed at 400 °C show no diffraction peaks in XRD, suggesting an amorphous film. Films grown at 100 ^oC crystallized upon annealing at 600 ^oC. Conversely, ALD deposition at higher temperature (250 ^oC) resulted in polycrystalline films with some dependence on film thickness. Powder XRD characterization showed polycrystalline structure in 30 nm films, but no discernible peaks could be found in 15 nm thick films grown under identical conditions. Instead, 15 nm films grown at 250 ^oC crystallized only upon post-deposition annealing at 400 ^oC. This crystallization at a lower annealing temperature than their lower temperature growth counterparts (400 ^oC vs 600 ^oC) indicates that some nuclei may have formed

with a volume below the detection limits of the instrument. Therefore, HfO_2 film growth at 250 ^oC may result in nano-crystallites within an amorphous matrix which leads to full crystallization at a critical thickness between (15 – 30 nm). No meaningful peak intensity could be obtained in 5 nm and 10 nm films due to the limited volume of the films. Therefore, the crystallinity of these thinner film suites is inferred from results in 30 nm thick HfO_2 films. For clarity, films are referred to by their inferred crystallinity and growth conditions (growth temperature/post-deposition anneal temperature).

AFM characterization shows that areal root mean square surface roughness (*S*q) of the HfO_2 films depends strongly on the roughness of the p+Si substrate (*S*q < 0.2 nm), as well as on the deposition temperature, but very little on the post-deposition annealing temperature. In 30 nm films, an increased roughness is observed in subsets of films between initial growth temperatures, with films grown at 100 ^oC having similar roughness to the polished p+Si (Sq = 0.4 nm), and films grown at 250 ^oC showing increased roughness (1.2 nm < *S*q < 1.32 nm; Table 1). Interestingly, in thinner films (5 – 15 nm thick) grown at 250 ^oC, surface roughness is much smoother, again similar to the roughness of the substrate (0.21 < S_q < 0.31 nm). Post-deposition annealing temperature has little influence on the surface roughness of HfO_2 films in these thickness suites as well. Therefore, the roughness of the HfO_2 surface is primarily inherited from the roughness of the polished p+Si electrode, with the higher growth temperature (250 ^oC) causing increased roughness only once a critical film thickness has been reached (15 – 30 nm). Finally, because the surface roughness of the film is independent of film crystallinity and is relatively smooth, any changes in forming kinetics or conductive filament shape are ascribed to film microstructure rather than difference in electrode roughness.

Table 3.1. Summary of microstructural properties resulting from thermal deposition and post-deposition annealing conditions.

HfO_2 thickness	Growth Temp. (ºC)	Anneal Temp. (ºC)	*Sq* (nm)	Grain size (nm)	Crystallinity
5	250	---	0.27 ± 0.03	19 ± 2	*
5	250	400	0.32 ± 0.01	23 ± 3	*
10	250	---	0.23 ± 0.05	23 ± 3	*
10	250	400	0.20 ± 0.01	20 ± 3	*
10	250	600	0.34 ± 0.06	---	*
15	250	---	0.31	18± 4	Amorphous
15	250	400	0.31	19 ± 2	Polycrystalline
30	100	400	0.15 ± 0.02	---	Amorphous
30	100	600	0.31 ± 0.02	24 ± 2	Polycrystalline
30	250	---	1.32 ± 0.03	35 ± 2	Polycrystalline
30	250	400	1.23 ± 0.09	37 ± 3	Polycrystalline
30	250	600	1.2 ± 0.1	36 ± 4	Polycrystalline

* denotes that peaks could not be clearly identified above background

3.3.2 Electrical Characterization

Because the behavior of subsequent cycles is determined largely by the properties of the initial filament, this study focuses only on the morphology of the initially formed filament. Forming of conductive filaments was accomplished using a constant bias (V_{form}) applied to the top electrode and the time at which current rose precipitously to the compliance current taken as the forming time (t_{form}). As previously observed [43], forming times in HfO_2 films showed an exponential dependence on applied bias and were much shorter in polycrystalline layers than in amorphous layers due to the existence of fast migration paths along grain boundaries (Fig. 3.2a). However, a common forming voltage of 8 V was preserved in order to make direct comparison between polycrystalline and amorphous layers formed under identical bias conditions. Between HfO_2 films of different thickness, results in 10 nm thick HfO_2 films show similar trends with

voltage and between processing conditions, albeit with a shift toward lower voltages, as expected from the scaling of the electric field with film thickness (Fig. B-1). In fact, when the slope of forming time versus electric field is extracted, significant difference between slopes are obtained between microstructural suites, but not between different thicknesses of HfO_2 films with identical thermal treatments. In 5 nm thick films, significant differences in t_{form} are not observed between HfO_2 films grown at 250 ^oC/annealed at 400 ^oC and grown at 250 ^oC/no post-deposition anneal. Because of the limited thickness of the film, lab XRD results could not confirm a difference in crystallinity between heat treatments. It is possible that at such limited thickness, the roughness of the bottom electrode and top surface serve to drastically reduce the migration distance in both cases.

Current-time traces of devices selected for AFM imaging are representative of I-t curves obtained for the majority of devices formed, and show similar characteristics, regardless of the crystallinity of the HfO_2 layer (Fig. 3.2b). An initial decay in current associated with charging of the capacitance of the dielectric layer proceeds, followed by either an abrupt or step-like increase in current, until a final breakdown is achieved with current limited at 100 μA which is taken as the forming time (t_{form}). We interpret these intermediate current jumps as the beginning of filament formation as ionic migration of Cu^+ into the HfO_2 film creates additional sites for electronic Poole-Frenkel hopping conduction or trap assisted tunneling to occur. In some cases, sharp decreases in current are observed as in sample SC, device C. In this case, these fluctuations are attributed to fluctuations in charge trapping and de-trapping (Fig. 3.2b). I-t curves in 10 nm films show similar characteristics. Both abrupt and gradual forming traces are observed (Fig. 3.2b) which may have implications for the initial shape and size of the conductive region.

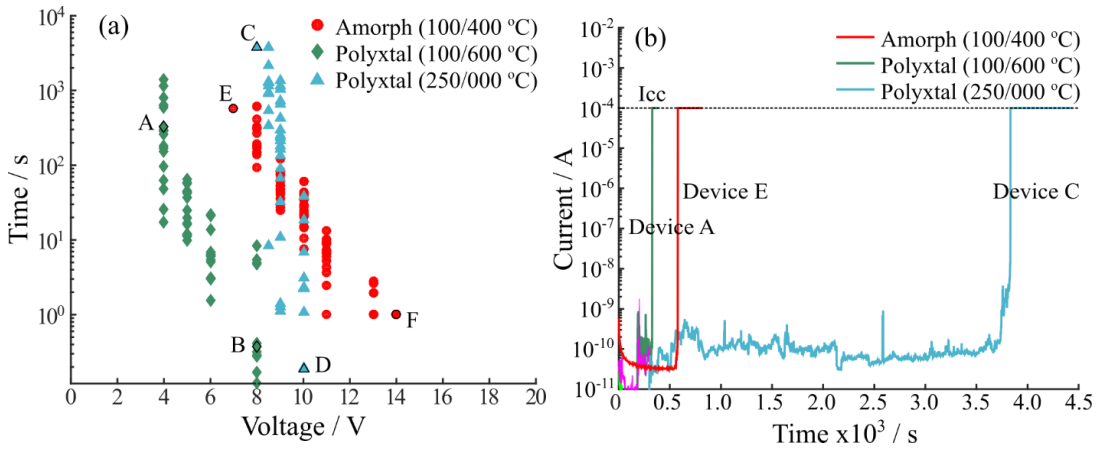

Figure 3.2. (a) Forming time (t_{form}) as a function of applied voltage bias (V_{form}) for devices based on 30 nm HfO_2 films with varying heat treatments and microstructures. (b) Current-time traces for selected devices from each microstructural category/heat treatment.

Resistance of formed devices was measured after the forming operation and results show that as V_{form} decreases, the resistance of the formed device increases. Here, when devices are formed above 4 V, the resistance of the "on-state", R_{on} does not scale with the set compliance current by ohm's law as expected, indicating some overshoot of the compliance current due to charge storage in parasitic elements of the test circuit [44]. Notably, R_{on} decreases as V_{form} increases both within and between HfO_2 films of differing microstructure (Fig B-2), consistent with the observation that the transient length and amplitude of the compliance current overshoot is related to applied voltage [45]. Thus, resistance of the conductive filament is primarily controlled by the compliance current overshoot and indirectly, V_{form}, rather than the electric field across the dielectric or microstructure of the dielectric. Finally, the variability in R_{on} is uniform across all forming conditions and HfO_2 dielectric microstructure groups ($\sigma \sim 15$ kΩ). Therefore, although the principal determinant of resistance state is I_{cc} overshoot, the source of variability could still have

several sources: (i) capacitance of the test circuits between runs (ii) materials properties that limit ion migration (iii) materials properties that limit heat transfer.

3.3.3 Device Deconstruction and 3D Tomography of Conductive Filaments

3.3.3.1 Device Deconstruction

In order to observe the relative impacts of electric field, V_{form}, and film microstructure on conductive filament size and shape, a dedicated AFM workflow was developed to deconstruct the formed device layer by layer, and ultimately obtain 3D shape by scratching through the HfO_2 matrix in selected devices. Device deconstruction was accompanied by optical microscopy and atomic force microscopy (1) on the top electrode of the device before forming, (2) from the top electrode of the device post-forming, and (3) conductive and topographic AFM imaging of the HfO_2 surface post removal of the top electrode. At the Cu top electrode, several topographic features were present in AFM images of the copper top electrode, but were later found not continuous from the HfO_2 surface through to the copper top electrode and were therefore interpreted as debris (Fig. 3.3a). Following removal of the top electrode, conductivity was exclusively used to identify and locate a conductive filament. Notably, all conductive signals were accompanied by some deformation of the HfO_2 layers of varying extents, with an oblong "hillock" ranging from (2 nm – 20 nm) in height found under the lowest V_{form} conditions (4 V). This observation demonstrates that conductive filament forming is accompanied by physical disruption and localized uplift of the oxide layer, which similarly deforms the Cu layer above it.

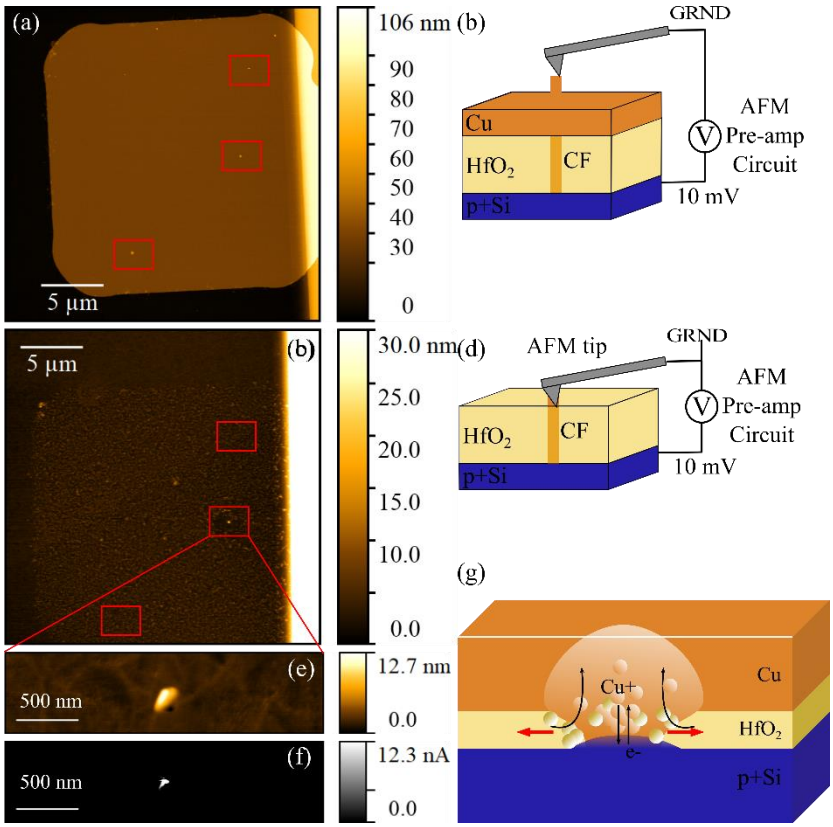

Figure 3.3. Deconstruction series of a conductive filament formed in 30 nm thick polycrystalline HfO_2 (100 ^oC/600 ^oC) at 4 V. (a) AFM topographic imaging of the device top electrode post-forming demonstrates 3 topographic "hillocks" which are potential conductive filament sites. (b) Schematic of the experimental set-up. (c) Imaging of the area post-etching removal of the top electrode shows that not all hillocks previously observed were below the top electrode, accompanied by (d) a schematic of the device status. Only a single location (e) showed both a topographic hillock associated with (f) a strong conductive signal saturating the amplification circuit, which is smaller in area (0.003 μm^2) than the topographic feature (0.025 μm^2). (g) A schematic of the potential forming mechanism showing that as Cu ions migrate toward the bottom electrode, the HfO_2 matrix is displaced upwards, while a high current density flowing from grounded bottom electrode to positively biased top electrode causes some electro-migration of the p+Si bottom electrode upwards. Simultaneously, the high electron current density causes a large increase in temperature in the region of the filament, which in turn drives lateral growth of the filament.

A major limitation of AFM techniques is an inability to sample the chemical composition of the structure under study. The composition of these central hillocks is a matter for further

investigation, but mostly likely involves some mixture of copper ions and defective, vacancy rich oxide. As the positive electric field drives metal migration into the oxide layer (as has been evidenced in several TEM-EELS studies [1, 46, 47]), volume expansion of the HfO_2 matrix must occur. At such high levels of current density and in the presence of large thermal gradients, it is not inconceivable that Cu downward migration forces some mass extrusion to the free surface (Fig. 3.3e). This mixed (Hf-Cu-O) composition would then explain the inability of the $FeCl_3$ solution to remove the conductive "hillock" and planarize the bare HfO_2 surface. Moreover, expected resistance values calculated from the resistivity of bulk Cu using a simple cylindrical model (area is the minimum measured conductive area and the height is equal to film thickness) yields values six orders of magnitude lower than measured device R_{on} values (Table 2). This discrepancy points to a filament composition that is not purely copper. Finally, the results of TEM studies of gate oxide breakdown suggest that the identified conductive "hillocks" might in some part be formed by the electro-migration of Si from the bottom electrode [48]. Electrons flowing from the bottom electrode toward the positively biased top electrode at a current density of ($J \sim 1 \cdot 10^8$ A·cm^{-2}) could produce an "electron wind" that causes Si atoms to migrate into and across the oxide layer. Such migration, termed dielectric breakdown induced epitaxy (DBIE), has been found to be the major microstructural defect in cases of hard dielectric breakdown in a wide variety of gate oxides (Si_3N, SiO_2, HfO_2) [49-51]. In these oxide layers (3 – 5nm thick), DBIE defects are observed using voltages as low as 2.5 V and compliance currents as low as 10 µA – 50 µA. In these voltage ranges, the metallic spiking desirable for resistance switching cannot be isolated from DBIE [51]. Thus, the chemical nature of the observed deformation of the oxide layer and conductive filament is proposed to be some mixture of Hf, O, Cu, and Si, although a uniform composition throughout is

not necessarily supported. Further TEM-EELS sample preparation and characterization would be required to definitively establish the composition of the region.

3.3.3.2 3D Tomograms

Following this initial deconstruction, selected devices were chosen for further investigation to establish the 3D shape of the formed conductive filaments. While 2D scans can give insight into area scaling at the top of the filament and filament location, subsequent switching parameters (V_{reset}, V_{set}, and the resistance states) are determined by the narrowest diameter and shape of a filament which could be buried within the matrix of the dielectric layer. In 10 nm thick and 30 nm thick polycrystalline HfO_2 films with devices formed at 4 V and compliance current of 100 µA, no macroscopic damage to the Cu top electrode or to the underlying HfO_2 films was observed by optical microscopy. Instead, the filament location corresponds to a topographic hillock (2 – 17 nm) above the plane of the HfO_2 film. Devices formed under these conditions were therefore chosen to study conductive filaments in the absence of catastrophic dielectric breakdown mechanisms.

Etch-wells were created over the course of more than 100 scans until the bottom electrode was reached and identified by the appearance of weak conductive signal across the bottom of the well. Etch removal rates were variant over both space and time. As the diamond AFM tip removed material from the initial hillock during the first several scans, the overall height of the scan area was increased by 1 nm, rather than decreased, indicative of the redistribution of material from the original hillock position. Following this process, the depth of the scratch through well increased at a decreasing rate, related to the progressive dulling of the conductive AFM tip. A removal rate of approximately 0.1 – 0.3 nm/scan was achieved with force settings of 0.4 V. In later cases, the contact force was gradually increased between wide scans in order to maintain a near constant etch rate. In all cases, the conductive signal saturates the AFM circuit (12 nA) and is contiguous

throughout the scan area. Although drift of the conductive area is noticeable as an artifact of unavoidable thermal sample drift during AFM imaging over a period of several hours, the boundaries of the conductive region do not change drastically between individual scans – indicating a small spatial uncertainty. Because an excessive contact force is employed to remove HfO_2 during scanning, it unlikely that filament area is underestimated due to poor tip-sample contact.

Conductive filament shape was studied in three conductive filaments in 10 nm thick polycrystalline HfO_2 layers (250/400 ^oC). Reconstructed tomograms show a wide degree of variability in shape, but also show that the filaments are similar in size and share a few common features. Topography maps initially showed oblong conductive regions associated with hillocks with dimensions lengths (100 – 300 nm) and width (50 – 75 nm). As the diamond tip begins to etch into the HfO_2 surface, conductivity narrows and expands non-uniformly approaching the bottom electrode (Fig. 3.4). Moreover, the location of the conductive spot seems to be more readily removed with the progression of the initial hillock into a shallow pit at the location of the conductive region, indicative of material mechanically weaker and more defect filled than that of the surrounding matrix. In all cases, the overall dimensions of the conductive signal is smaller than the topographic features it is associated with, indicating that not all of the deformed and defect rich region is highly conductive. Topographic data simultaneously collected was used to correct the conductive signal of the scans, so that reinterpreted 2D bisection of the conductive volume yields the true shape of the filament (Fig. 3.4d). The final dimensions of the filaments is relatively similar with an overall oblong shape and maximum dimensions of (~100 nm x ~50 nm). Here, the largest dimensions of these “filaments” far exceed the median grain size (~25 nm) for these films, with even the narrowest points approaching the width of a single grain. Clearly, whatever route along a

grain boundary ionic migration may have initially taken, this route was subsumed in the expansion of the filament laterally and vertically during forming. Here, the large temperature gradients caused by high current densities flowing through the nascent filament serve to broaden conductive filaments laterally and become the principal determinants of the maximum filament radii.

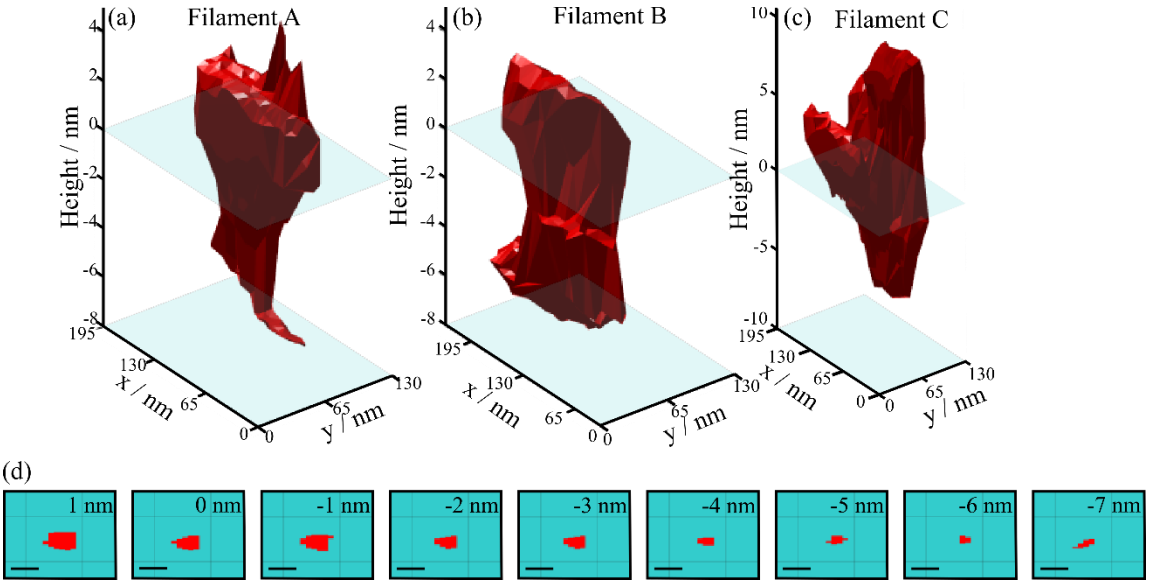

Figure 3.4. Three separate filaments in 10 nm thick polycrystalline (250/ 400 ºC/) HfO_2 films formed under nominally the same conditions (4 V, I_{cc} = 100 µA) showing (a) an inverted cone geometry, (b) a more cylindrical geometry, and (c) a branched geometry. The narrowing of filament A is clearly seen in (d) topography corrected 2D conductivity maps sampled at 1 nm intervals along the height of the filament, with 0 nm referencing the bare HfO_2 surface. The inset scale bar corresponds to 32.5 nm.

Despite these similarities, a comparison in shape between three filaments formed under identical conditions shows the wide degree of variation in shape expected from measured device R_{on} values (Table 3.2). In filament A, an inverted cone shape is apparent as conductivity narrows from the HfO_2 surface (0 nm) to the bottom electrode reaching ~20 nm in diameter at its narrowest point, as can be seen in the tomogram (Fig. 3.4a) as well as corrected 2D scans (Fig. 3.4d). Filament

B is more cylindrical in nature, albeit with some regions narrowing around -3 nm. Filament C is the most distinctively different in shape from the others, with a second branch stemming from the bottom electrode to intersect the HfO_2 surface, while the main portion of the filament also shows some narrowing in the (-2 nm to -4 nm) region. Interestingly, although at least one of the filaments (Filament A) demonstrates the inverse cone shape expected from the accepted electrochemical metallization model [6, 8], the others deviate strongly from this expected shape. This observation of deviation from the accepted model may stem from thermally driven filament broadening, while the wide range of shapes encountered in filament formed under identical electrical stress conditions could stem from (i) differences in initial ionic migration routes (ii) differences in heat transfer and thermal gradients through the oxide layer or electrodes [52], or (iii) differences in stored parasitic capacitances. Here, the final size and shape of the filament formed under the present electrical bias conditions (representative of device testing conditions in many other studies [53-55]) is likely determined by potent thermal driving forces during the broadening phase of the filament, which are themselves susceptible to several sources of variability.

The conductive filament shape formed under equivalent bias (V_{form} = 4V) within a 30 nm thick oxide layer was also examined and compared with results obtained in 10 nm films. At lower electric field (1.3 MV/cm) in the 30 nm thick randomly oriented polycrystalline HfO_2 film (100 ^oC/600 ^oC), the conductive filament (Fig. 3.5) is larger in area as compared with the filaments in 10 nm films (Fig. 3.4), corresponding to the lower measured resistance of the device (Table 3.2). The initial height of the hillock was 17.8 nm tall and required several scans itself to remove. The dimensions of the filament at its' largest point near the HfO_2 interface and at the bottom electrode are on the order of 150 nm x 50 nm. The filament's narrowest point (20 nm in radius) corresponds to the intersection of the HfO_2 surface, and rather than being the true shape of the filament, it is

likely that redistribution of the material from the scribed away hillock limits the conductive signal area. In contrast to the shape of the filaments in the thinner films, the area of the filament does not decrease progressing toward the bottom electrode, but instead remains fairly constant until splitting into several branches intersecting the bottom electrode (Fig. 3.5). Although the entire thickness of the film was not able to be removed before dulling of the diamond tip precluded further scratching (final depth of the well was 28 nm), it is likely that a continuation of the branches would be observed penetrating into the p+Si bottom electrode. As in the 10 nm thick films, the shape of the conductive filament deviates strongly from the expected inverse conical shape under the given electroforming conditions.

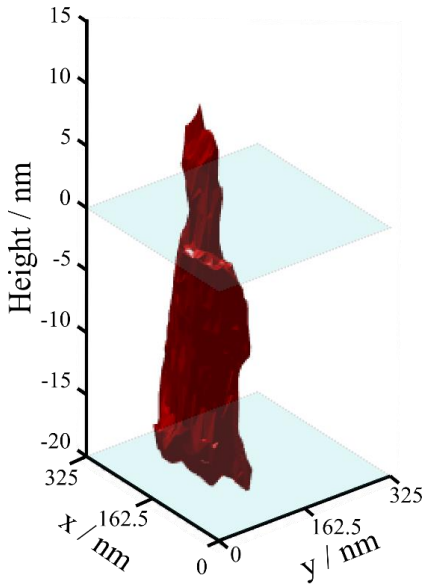

Figure 3.5. 3D reconstruction of filament formed in 30 nm polycrystalline HfO_2 film (100 ^oC /600 ^oC) at 4 V, Icc = 100 µA.

Table 3.2. Electrical forming characteristics for devices used in 3D scratch-through experiments

Filament	HfO_2 thickness	V_{form}	t_{form} (s)	Ron (kΩ)
A	10	4	102	23.8
B	10	4	10	83.4
C	10	4	76	44.4
D	30	4	1408	6.7

3.3.4 Extent of deformation: from filament structures to catastrophic breakdown

In order to determine the relative impacts of V_{form}, electric field, and HfO_2 film microstructure the deformation caused by uncontrolled mass flux during device forming was observed first at the copper top electrode and then at the uncovered dielectric layer by a combination of optical microscopy and atomic force microscopy at smaller length scales. The extent of deformation lies along a spectrum from nm scale uplift of the Cu top electrode and HfO_2 layer deformation to micron scale catastrophic disruption and melting away of the top electrode, implicating thermal dielectric breakdown mechanisms. Importantly, the area of the damage scales with V_{form} and the scaling is relatively unaffected by HfO_2 layer microstructure or film thickness i.e. electric field (Fig. 3.6; Fig. B3 - B5).

In all devices formed above 5V, the copper top electrode appears to have melted in a ridge surrounding a depression in the HfO_2 layer (Fig. 3.6 inset). Optical Microscopy and AFM topographic imaging of device top electrodes revealed linearly increasing melt area as forming voltage increased within each oxide microstructure series in 30 nm HfO_2 films (Fig. 3.6). Between oxide microstructure series, and over the full range of forming voltages, a few common features were observable in dielectric breakdown spots. In amorphous oxides (100/400 ^oC), as the forming bias increases between 7 V and 14 V, and the oxide breakdown observed on the edges of devices

grows in area from ~1 μm^2 at 7 V to ~10 μm^2 at 14 V (Fig. 3.6). In oriented polycrystalline HfO_2 films (250/000 ºC), damage areas range from ~0.2 μm^2 to 2 μm^2 at 8 V and 10 V, respectively. In the more randomly oriented polycrystalline film (100/600 ºC) cumulative damage area scales from 500 nm^2 at 4 V to 2 μm^2 at 8 V. In many cases, devices in this film formed at (4 – 5) V showed no penetration of the copper top electrode optically. However, AFM imaging of the top electrode later revealed the presence of (10 to 30) nm hillocks which deformed, but did not penetrate the 25 nm thick copper top electrode.

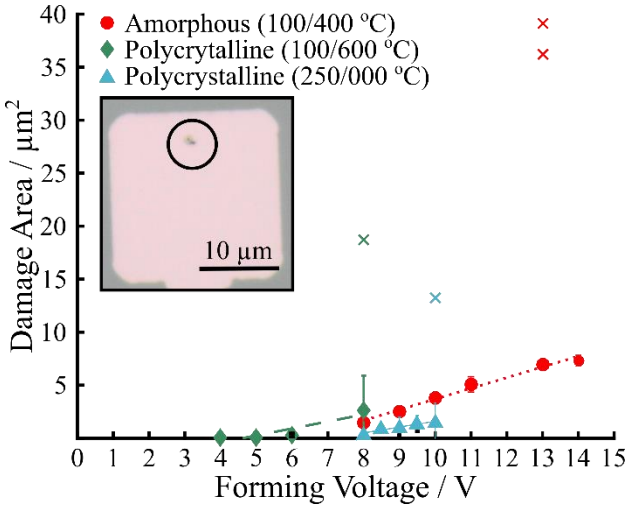

Figure 3.6. Mean area of dielectric breakdown calculated from optical microscopy images at 100X magnification at each applied forming bias. Outliers in each series are plotted as an 'X'. Inset: a characteristic device from 30 nm polycrystalline (250/000 ºC) films showing disruption of the thin (25 nm) copper top contact.

The morphology of the breakdown in the HfO_2 dielectric layer is similar to breakdown morphologies observed in capacitance failure and gate oxide failures in MOS-caps. A small hillock (3 – 50 nm in height and 50 – 500 nm in width) is observed before and after the removal of the copper electrode in all samples (Fig. 3.3) and over all forming voltages. It is likely that this hillock represents the initial site of breakdown with damage irradiating outward from this site. In devices formed above 5 V, this hillock is surrounded by a pit, which in some cases penetrates into the p+Si substrate. The area and depth of this pit also scales with forming voltage, ranging from 1 μm^2 to ~3 μm^2 (Fig. B3 - B5). Within each oxide microstructure series, the area of the damage scales with V_{form} (Fig. B3 - B5), with the most dramatic breakdown structures observed in 30 nm amorphous HfO_2 films (V_{form} =14 V) and minimized in polycrystalline films at 4V with "hillocks" 2 nm – 30 nm tall. Thus, damage in the HfO_2 dielectric layer shows the same trends in scaling with V_{form} as top electrode melting and is indicative of redistribution of the dielectric layer along a spectrum, from simple expansion/extrusion at 4V to increasing mass loss at 14 V.

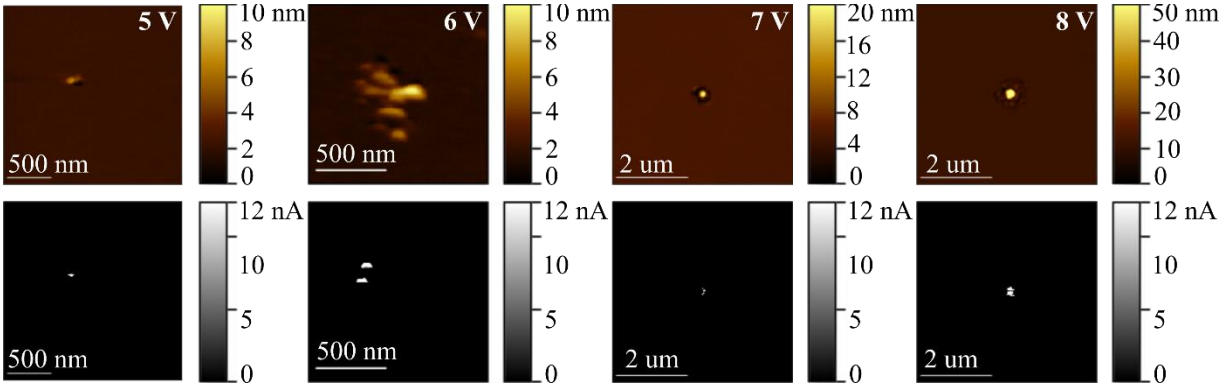

Figure 3.7. (Top) AFM topographic images demonstrate increasing areas of mass redistribution as a function of increasing V_{form} from 5 – 8 V accompanied by (Bottom) increasing areas of conductive regions demonstrated in c-AFM images.

The primary mechanism for the massive damage of the HfO_2 layer and Cu top electrode observed optically and by AFM is frequently encountered in studies of capacitor breakdown and gate oxide breakdown, as well as during electrostatic discharge (ESD) events [47, 51, 56-58]. As the resistance of the device under test transitions from the initial high resistance state to the final low resistance state within hundreds of ns, parasitic capacitance in the testing equipment and the bondpad of the device (estimated around ~1 nF), discharges a large current into the device. Measurement of discharge currents at ns time scales has shown that this overshoot can range from 10 – 100 times the compliance current [44, 59, 60]. The solution widely adopted includes integration of a transistor or diode lithographically connected to the device on chip, so that the area which accumulates stray capacitance is minimized. However, it has also been shown that parasitic currents can be limited via reduction of applied forming voltage indirectly by increasing the discharge time and reducing the amplitude of the discharge peak [45]. The magnitude of this current was not measured as in other studies, but can be estimated from the reset current (I_{reset}) obtained in the subsequent cycle by the relationship $I_{set} \approx I_{reset}$. In tested devices, I_{reset} ranged between 1 mA and 10 mA, indicating that the parasitic current overshoot was at least 10 times greater than the set I_{cc} of 100 μA when $V_{form} > 4$ V. At it's lowest levels, this uncontrolled current discharge then causes local heating via joule heating, driving ion diffusion leading to broadening of the conductive filament. At the other extreme, temperatures reached are high enough to participate in a feedback loop of catastrophic dielectric breakdown; as electrons release heat passing through the dielectric layer, more defects are thermally created, which in turn allow even more electrons to flow through the breakdown location, eventually leading to the observed catastrophic breakdown structures.

Between HfO_2 films with different initial microstructure tested at an identical V_{form} (8V), the morphology of the breakdown differs in shape and in location (Fig. B-6). In amorphous HfO_2 films, damage occurs only at the edge of devices so that the central hillock is surrounded by a semicircle of missing HfO_2 material, penetrating down to 30 nm through the p+Si bottom electrode. In more oriented polycrystalline film, the site is within the interior of the device electrode, and encompasses a hillock surrounded by a bowl, again penetrating through the depth of the bottom electrode. Finally, in more randomly oriented polycrystalline films, several shallow sites are identified with a central hillock. The randomly oriented grain structure of the polycrystalline (100/600 ^oC) film provides for significantly different damage morphology than that observed in the amorphous (100/400 ^oC) and more oriented polycrystalline (250/000 ^oC) films. Copper migration is energetically favored along several different grain boundary pathways, leading to the observation of multiple breakdown spots. Moreover, the total device current is divided and reduced in each separate parallel branch in the case of multiple filaments, resulting in a smaller damage extent at each location. Therefore, while V_{form} is the principal determinant of damage area and depth, the microstructure of the oxide layer determines the location and multiplicity of disruption.

Although these observations of top electrode melting and oxide disruption dependence on V_{form} seem rather obvious in the context of the wide body of dielectric breakdown literature, the implications for resistance switching device based studies are not inconsequential. While it has been demonstrated that parasitic discharges and I_{set}/I_{reset} can be controlled below 10 μA with lithographically integrated transistors or diodes [61], some amount of thermal energy dissipation is still required during reset operations or even during the initial filament forming operation where applied voltages are often > 2 V. Many groups report initial forming ($I_{cc} \geq 100$ μA) in order to

achieve stable R_{on} states and acceptable R_{on}/R_{off} ratios. Additionally, many recent reports on device variability utilize devices with no integrated compliance current control, suggesting that thermal dielectric breakdown mechanisms observed in this work would also be observed in these systems. As shown, these mechanisms are highly destructive to the oxide layer and contribute a large degree of variability in physical size/shape of damage spots, and could occlude the impact of tested variables. For this reason, proper device integration and use of lower I_{cc} values is necessary for minimization of device variability due to thermal damage to the oxide layer, with the caveat that the R_{on} state will be raised closer to the R_{off} state.

3.4 Conclusions

In conclusion, the 3D shape of conductive filaments formed in p+Si/HfO_2/Cu PMC devices based on a polycrystalline HfO_2 layer has been explored with a scalpel c-AFM tomography technique. Results for filaments formed under identical conditions show a range of shapes including conical, cylindrical, and branched, which deviates from the exclusively inverted-cone shape predicted by the phenomenological electrochemical model [6]. Thermal broadening of the filament caused by compliance current overshoot is strongly implicated in this shape deviation by the observation of an increasing spectrum of HfO_2 film damage with increasing forming voltage (and not electric field). Here, the amplitude and duration of compliance current overshoot scales with V_{form}, and thus the thermal energy released into the confined filament region scales with $V_{form.}$ At the lowest voltage (4V), filament formation is accompanied by minimal uplift of the HfO_2 dielectric film and Cu top electrode, while at the highest voltage (14 V) catastrophic mass removal is observed. Finally, the role of microstructure is shown to be to direct the location of filament forming sites, while V_{form} directs the ultimate size of the filaments or damage.

3.5 References

[1] Lv H, Xu X, Liu H, Liu R, Liu Q, Banerjee W, Sun H, Long S, Li L and Liu M 2015 Evolution of conductive filament and its impact on reliability issues in oxide-electrolyte based resistive random access memory *Scientific reports* **5**

[2] Lien C, Chen Y, Lee H, Chen P, Chen F and Tsai M-J 2010 The highly scalable and reliable hafnium oxide ReRAM and its future challenges: IEEE) p 1084-7

[3] Govoreanu B, Kar G, Chen Y, Paraschiv V, Kubicek S, Fantini A, Radu I, Goux L, Clima S and Degraeve R 2011 10× 10nm 2 Hf/HfO x crossbar resistive RAM with excellent performance, reliability and low-energy operation: IEEE) p 31.6. 1-.6. 4

[4] Ye C, Zhan C, Tsai T-M, Chang K-C, Chen M-C, Chang T-C, Deng T and Wang H 2014 Low-power bipolar resistive switching TiN/HfO2/ITO memory with self-compliance current phenomenon *Applied Physics Express* **7** 034101

[5] Yang J J, Strukov D B and Stewart D R 2013 Memristive devices for computing *Nature nanotechnology* **8** 13-24

[6] Valov I, Waser R, Jameson J R and Kozicki M N 2011 Electrochemical metallization memories—fundamentals, applications, prospects *Nanotechnology* **22** 254003

[7] Waser R and Aono M 2007 Nanoionics-based resistive switching memories *Nature materials* **6** 833

[8] Waser R, Dittmann R, Staikov G and Szot K 2009 Redox-based resistive switching memories−nanoionic mechanisms, prospects, and challenges *Advanced Materials* **21** 2632-63

[9] Strachan J P, Torrezan A C, Miao F, Pickett M D, Yang J J, Yi W, Medeiros-Ribeiro G and Williams R S 2013 State dynamics and modeling of tantalum oxide memristors *IEEE Transactions on Electron Devices* **60** 2194-202

[10] Pickett M D, Strukov D B, Borghetti J L, Yang J J, Snider G S, Stewart D R and Williams R S 2009 Switching dynamics in titanium dioxide memristive devices *Journal of Applied Physics* **106** 074508

[11] Raghavan N 2017 Failure of Weibull distribution to represent switching statistics in OxRAM *Microelectronic Engineering* **178** 230-4

[12] Strukov D B and Williams R S 2011 Intrinsic constrains on thermally-assisted memristive switching *Applied Physics A* **102** 851-5

[13] Kim S, Choi S and Lu W 2014 Comprehensive physical model of dynamic resistive switching in an oxide memristor *ACS nano* **8** 2369-76

[14] Russo U, Ielmini D, Cagli C and Lacaita A L 2009 Self-accelerated thermal dissolution model for reset programming in unipolar resistive-switching memory (RRAM) devices *IEEE Transactions on Electron Devices* **56** 193-200

[15] Ielmini D, Nardi F and Cagli C 2011 Physical models of size-dependent nanofilament formation and rupture in NiO resistive switching memories *Nanotechnology* **22** 254022

[16] Menzel S 2017 Comprehensive modeling of electrochemical metallization memory cells *Journal of Computational Electronics* **16** 1017-37

[17] Kim K M, Lee M H, Kim G H, Song S J, Seok J Y, Yoon J H and Hwang C S 2010 Understanding structure-property relationship of resistive switching oxide thin films using a conical filament model *Applied Physics Letters* **97** 162912

[18] Waser R, Dittmann R, Staikov G and Szot K 2009 Redox-based resistive switching memories−nanoionic mechanisms, prospects, and challenges *Advanced materials* **21** 2632-63

[19] Kim H J, Yoon K J, Park T H, Kim H J, Kwon Y J, Shao X L, Kwon D E, Kim Y M and Hwang C S 2017 Filament Shape Dependent Reset Behavior Governed by the Interplay between the Electric Field and Thermal Effects in the Pt/TiO2/Cu Electrochemical Metallization Device *Advanced Electronic Materials* **3** 1600404

[20] Kwon D-H, Kim K M, Jang J H, Jeon J M, Lee M H, Kim G H, Li X-S, Park G-S, Lee B and Han S 2010 Atomic structure of conducting nanofilaments in TiO 2 resistive switching memory *Nature nanotechnology* **5** 148

[21] Privitera S, Bersuker G, Butcher B, Kalantarian A, Lombardo S, Bongiorno C, Geer R, Gilmer D and Kirsch P 2013 Microscopy study of the conductive filament in HfO2 resistive switching memory devices *Microelectronic Engineering* **109** 75-8

[22] Celano U, Goux L, Belmonte A, Opsomer K, Franquet A, Schulze A, Detavernier C, Richard O, Bender H and Jurczak M 2014 Three-dimensional observation of the conductive filament in nanoscaled resistive memory devices *Nano letters* **14** 2401-6

[23] Yang Y, Gao P, Gaba S, Chang T, Pan X and Lu W 2012 Observation of conducting filament growth in nanoscale resistive memories *Nature communications* **3** 732

[24] Belmonte A, Celano U, Redolfi A, Fantini A, Muller R, Vandervorst W, Houssa M, Jurczak M and Goux L 2015 Analysis of the excellent memory disturb characteristics of a hourglass-shaped filament in Al 2 O 3/Cu-based CBRAM devices *IEEE Transactions on Electron Devices* **62** 2007-13

[25] Brivio S, Tallarida G, Cianci E and Spiga S 2014 Formation and disruption of conductive filaments in a HfO2/TiN structure *Nanotechnology* **25** 385705

[26] Buckwell M, Montesi L, Hudziak S, Mehonic A and Kenyon A J 2015 Conductance tomography of conductive filaments in intrinsic silicon-rich silica RRAM *Nanoscale* **7** 18030-5

[27] Liu Q, Sun J, Lv H, Long S, Yin K, Wan N, Li Y, Sun L and Liu M 2012 Real-Time Observation on Dynamic Growth/Dissolution of Conductive Filaments in Oxide-Electrolyte-Based ReRAM *Advanced Materials* **24** 1844-9

[28] Tappertzhofen S, Valov I, Tsuruoka T, Hasegawa T, Waser R and Aono M 2013 Generic relevance of counter charges for cation-based nanoscale resistive switching memories *ACS nano* **7** 6396-402

[29] Yang Y, Gao P, Li L, Pan X, Tappertzhofen S, Choi S, Waser R, Valov I and Lu W D 2014 Electrochemical dynamics of nanoscale metallic inclusions in dielectrics *Nature communications* **5**

[30] Valov I and Waser R 2013 Comment on Real-Time Observation on Dynamic Growth/Dissolution of Conductive Filaments in Oxide-Electrolyte-Based ReRAM *Advanced Materials* **25** 162-4

[31] Claramunt S, Wu Q, Maestro M, Porti M, Gonzalez M, Martin-Martinez J, Campabadal F and Nafría M 2015 Non-homogeneous conduction of conductive filaments in Ni/HfO 2/Si resistive switching structures observed with CAFM *Microelectronic Engineering* **147** 335-8

[32] Choi B, Jeong D, Kim S, Rohde C, Choi S, Oh J, Kim H, Hwang C, Szot K and Waser R 2005 Resistive switching mechanism of TiO2 thin films grown by atomic-layer deposition *Journal of Applied Physics* **98** 033715

[33] Son J and Shin Y-H 2008 Direct observation of conducting filaments on resistive switching of NiO thin films *Applied Physics Letters* **92** 2106

[34] Singh B, Mehta B, Varandani D, Savu A V and Brugger J 2012 CAFM investigations of filamentary conduction in Cu2O ReRAM devices fabricated using stencil lithography technique *Nanotechnology* **23** 495707

[35] Yang L, Kuegeler C, Szot K, Ruediger A and Waser R 2009 The influence of copper top electrodes on the resistive switching effect in TiO2 thin films studied by conductive atomic force microscopy *Applied Physics Letters* **95** 013109

[36] Lanza M, Zhang K, Porti M, Nafria M, Shen Z, Liu L, Kang J, Gilmer D and Bersuker G 2012 Grain boundaries as preferential sites for resistive switching in the HfO2 resistive random access memory structures *Applied Physics Letters* **100** 123508

[37] Bersuker G, Gilmer D, Veksler D, Kirsch P, Vandelli L, Padovani A, Larcher L, McKenna K, Shluger A and Iglesias V 2011 Metal oxide resistive memory switching mechanism based on conductive filament properties *Journal of Applied Physics* **110** 124518

[38] Lanza M, Bersuker G, Porti M, Miranda E, Nafría M and Aymerich X 2012 Resistive switching in hafnium dioxide layers: local phenomenon at grain boundaries *Applied Physics Letters* **101** 193502

[39] Szot K, Speier W, Bihlmayer G and Waser R 2006 Switching the electrical resistance of individual dislocations in single-crystalline SrTiO3 *Nature materials* **5** 312-20

[40] Du Y, Kumar A, Pan H, Zeng K, Wang S, Yang P and Wee A T S 2013 The resistive switching in TiO2 films studied by conductive atomic force microscopy and Kelvin probe force microscopy *AIP Advances* **3** 082107

[41] Buckwell M, Zarudnyi K, Montesi L, Ng W H, Hudziak S, Mehonic A and Kenyon A J 2016 Conductive AFM Topography of Intrinsic Conductivity Variations in Silica Based Dielectrics for Memory Applications *ECS Transactions* **75** 3-9

[42] Celano U, Goux L, Belmonte A, Opsomer K, Degraeve R, Detavernier C, Jurczak M and Vandervorst W 2015 Understanding the dual nature of the filament dissolution in conductive bridging devices *The journal of physical chemistry letters* **6** 1919-24

[43] Clarke H, Brown T, Hu J, Ganguli R, Reed A, Voevodin A and Shamberger P J 2016 Microstructure dependent filament forming kinetics in HfO2 programmable metallization cells *Nanotechnology* **27** 425709

[44] Kinoshita K, Tsunoda K, Sato Y, Noshiro H, Yagaki S, Aoki M and Sugiyama Y 2008 Reduction in the reset current in a resistive random access memory consisting of Ni O x brought about by reducing a parasitic capacitance *Applied Physics Letters* **93** 033506

[45] Kalantarian A, Bersuker G, Gilmer D, Veksler D, Butcher B, Padovani A, Pirrotta O, Larcher L, Geer R and Nishi Y 2012 Controlling uniformity of RRAM characteristics through the forming process: IEEE) p 6C. 4.1-6C. 4.5

[46] Raghavan G, Chiang C, Anders P B, Tzeng S-M, Villasol R, Bai G, Bohr M and Fraser D B 1995 Diffusion of copper through dielectric films under bias temperature stress *Thin Solid Films* **262** 168-76

[47] Raghavan N, Pey K L and Shubhakar K 2014 High-κ dielectric breakdown in nanoscale logic devices–Scientific insight and technology impact *Microelectronics Reliability* **54** 847-60

[48] Lombardo S, Stathis J H, Linder B P, Pey K L, Palumbo F and Tung C H 2005 Dielectric breakdown mechanisms in gate oxides *Journal of applied physics* **98** 121301

[49] Selvarajoo T A, Ranjan R, Pey K-L, Tang L-J, Tung C H and Lin W 2005 Dielectric-breakdown-induced epitaxy: a universal breakdown defect in ultrathin gate dielectrics *IEEE Transactions on Device and Materials Reliability* **5** 190-7

[50] Pey K, Raghavan N, Li X, Liu W, Shubhakar K, Wu X and Bosman M 2010 New insight into the TDDB and breakdown reliability of novel high-κ gate dielectric stacks: IEEE) p 354-63

[51] Lombardo S, Stathis J H, Linder B P, Pey K L, Palumbo F and Tung C H 2005 Dielectric breakdown mechanisms in gate oxides *Journal of Applied Physics* **98** 12

[52] Chang S, Chae S, Lee S, Liu C, Noh T, Lee J, Kahng B, Jang J, Kim M and Kim D-W 2008 Effects of heat dissipation on unipolar resistance switching in Pt⁄Ni O⁄Pt capacitors *Applied Physics Letters* **92** 183507

[53] Fantini A, Goux L, Degraeve R, Wouters D, Raghavan N, Kar G, Belmonte A, Chen Y-Y, Govoreanu B and Jurczak M 2013 Intrinsic switching variability in HfO 2 RRAM: IEEE) p 30-3

[54] Lin K-L, Hou T-H, Shieh J, Lin J-H, Chou C-T and Lee Y-J 2011 Electrode dependence of filament formation in HfO2 resistive-switching memory *Journal of Applied Physics* **109** 084104

[55] Wei Zhou L, Long Shao X, Yuan Li X, Jiang H, Chen R, Jean Yoon K, Jin Kim H, Zhang K, Zhao J and Seong Hwang C 2015 Interface engineering for improving reliability of resistance switching in Cu/HfO2/TiO2/Pt structure *Applied Physics Letters* **107** 072901

[56] Ribes G, Mitard J, Denais M, Bruyere S, Monsieur F, Parthasarathy C, Vincent E and Ghibaudo G 2005 Review on high-k dielectrics reliability issues *IEEE Transactions on Device and materials Reliability* **5** 5-19

[57] Wunsch D and Bell R 1968 Determination of threshold failure levels of semiconductor diodes and transistors due to pulse voltages *IEEE Transactions on Nuclear Science* **15** 244-59

[58] Kelly M, Servais G, Diep T, Lin D, Twerefour S and Shah G 1995 A comparison of electrostatic discharge models and failure signatures for CMOS integrated circuit devices: IEEE) p 175-85

[59] Tirano S, Perniola L, Buckley J, Cluzel J, Jousseaume V, Muller C, Deleruyelle D, De Salvo B and Reimbold G 2011 Accurate analysis of parasitic current overshoot during forming operation in RRAMs *Microelectronic Engineering* **88** 1129-32

[60] Wan H, Zhou P, Ye L, Lin Y, Tang T, Wu H and Chi M 2010 In situ observation of compliance-current overshoot and its effect on resistive switching *IEEE Electron Device Letters* **31** 246-8

[61] Nardi F, Ielmini D, Cagli C, Spiga S, Fanciulli M, Goux L and Wouters D 2011 Control of filament size and reduction of reset current below 10μA in NiO resistance switching memories *Solid-State Electronics* **58** 42-7

4. NUCLEATION CONTROLLED HYSTERESIS IN UNSTRAINED HYDROTHERMAL VO_2 PARTICLE*

4.1 Introduction

The metal-insulator transition in VO_2 has been extensively studied due to both fundamental interests in the nature of coupled structural-electronic phase transitions, as well as practical interest in the large changes in electronic resistivity, optical transmittance, reflectivity, and thermal conductivity that accompany this phase transition. These changes in properties accompany a martensitic-like structural phase transition from the low-temperature monoclinic phase (M1) to a high temperature rutile phase (R) near 67 ^{o}C [1]. Understanding of specific microscopic phase transformation mechanisms is a critical step along the path of controlling various aspects of the phase transition, including transformation temperatures, transformation widths, and hysteresis widths. In particular, the hysteresis of a phase transition could result from kinetic undercooling or superheating required to overcome nucleation energy barriers of a daughter phase, or could be associated with internal friction accompanied by the growth of a new domain and concurrent motion of a heterophase boundary. Engineering of hysteresis widths could be especially advantageous as it offers an additional, path dependent route to control phase fraction at a given temperature intermediate between the final transition temperatures, and therefore can control the degree of reversibility (or volatility) of macroscopic properties (resistivity, reflectivity, transmissivity).

---

* Reprinted with permission from "Nucleation controlled hysteresis in unstrained hydrothermal VO_2 particles" by Heidi Clarke, Bill D. Caraway, Diane G. Sellers, Erick J. Braham, Sarbajit Banerjee, Raymundo Arròyave, Patrick J. Shamberger, 2018. Physical Review Materials, 2, 103402, Copyright 2018 by American Physical Society.

Variation of transformation width and the extent of phase coexistence has been controlled by application of external strain in undoped VO_2. Undoped VO_2 particles, elastically clamped to the substrate by high temperature CVD growth (900 – 1100 ^oC) [2] demonstrate a rich variety of microscopic phase coexistence of M1, M2, and R phases [3-12]. These microstructures result from the balance of external strain energy from elastic clamping to the substrate and the interfacial energy added by domain wall formation [4]. At the particle level, these observations have shown that phase coexistence regimes in individual strained particles lead to broad phase transitions via modifications to thermodynamic driving forces which change T_{cr} [3, 4, 6, 13, 14]. In contrast, phase transitions in free-standing VO_2 studied simultaneously in these experiments [3, 4, 9] are sharp, and no microscopic domains have been observed. The lack of phase coexistence suggests that free-standing, undoped VO_2 particles may represent the ideal setting for studies of intrinsic nucleation in VO_2.

Previous kinetic studies in individual un-doped free-standing VO_2 particles suggest that nucleation of M1 (R) embryos upon cooling (heating) is rate-limiting, while the growth of M1 or R phases is too fast to be observed by most techniques [15]. Heterogeneous nucleation is also posited, as calculations using classical nucleation theory yield a homogeneous nucleation barrier of ~ 10^4 kT, ruling out homogeneous nucleation as a mechanism at experimentally observed transition temperatures [16]. Furthermore, a few studies have sought to identify heterogeneous nucleation sites in nano-scaled systems. Oxygen vacancies located at grain boundaries are implicated by plasmonic resonance spectroscopy as heterogeneous nucleation sites [17]. By contrast, in elastically clamped individual VO_2 particles, nucleation sites have been associated with twin walls during the heating transition, and with point defects introduced by α-particle irradiation during the cooling transition [18]. In strained (due to substrate-film lattice mismatch) epitaxial thin

films, nucleation has also been statistically linked to domain boundary sites [7, 8]. Therefore, in both free-standing and elastically clamped individual particles, heterogeneous nucleation is rate-limiting and associated with crystallographic defects which serve to lower the energy barrier for phase transition.

In contrast to the well characterized heterogeneous nucleation in metallic martensitic systems [19, 20], the statistics of nucleation of the martensitic transformation in VO_2 is not well established, and the hysteresis width dependence on particle size as well as the width of transformation peak are not completely explained. In studies on bulk ensembles of particles, a dependence of hysteresis width on availability of nucleation sites has been explained by developing phenomenological models correlating ΔT_{cr} with particle width [15], particle volume [16, 21], thin film grain size [22], and thin film defect density [17, 22]. However, there remains a lack of direct observations quantifying the statistics of nucleation on an individual particle basis for oxides synthesized by different growth techniques. To address this deficit, it is necessary to relate the distribution between particles both on heating and cooling to the macroscopically observed transition widths and to identify any particle size dependence within the statistical distributions. Clarifying changes in phase transformation mechanisms requires microscopic investigation of domain nucleation and growth, beginning with the simplest case - undoped, unstrained VO_2. Resolving these questions can expose important underlying clues in understanding transformation mechanisms in both undoped and chemically doped systems, and can reveal new approaches to engineering metal-insulator transitions with desired transformation behavior.

In this work, we observe nucleation limited M1 to R and R to M1 phase transitions in free-standing, hydrothermally grown VO_2 on the individual particle basis by optical microscopy.

Furthermore, we identify a distribution of transformation hysteresis across a population of particles, which directly correlates to bulk powder observations of T_c and ΔT_{cr}. Here, we show that a distribution in the potency of nucleation sites between individual particles, both on heating and cooling, is responsible for the observed macroscopic hysteresis width in this phase transition. These findings have strong implications for future scaling of micro or nano-electronic VO_2 devices, which must maximize a number of sufficiently low activation barrier nucleation sites to achieve low hysteresis widths and minimize power dissipations.

4.2 Methods

Single crystal particles of VO_2 were synthesized hydrothermally from bulk V_2O_5 powder (Beantown Chemicals) using a reducing agent of high purity isopropanol. Samples were prepared with 1.63 g V_2O_5, 10 mL of isopropanol, and 65 mL of deionized water (ρ= 18.2 MΩ cm-1, Barnstead International NANOpure Diamond ultrapure water system). The mixtures were placed in 125 mL polytetrafluoroethylene cups and heated in a high pressure autoclave reactor at 210 °C for 72 hours. Samples were recovered by vacuum filtration and washed three times with deionized water and acetone. To relieve any strain from synthesis, samples were annealed under Ar (g) at 550°C for 5 hours. Only M1 and R phases are observed in samples synthesized by this approach [23]. Resulting morphology of VO_2 particles included wire-like structures consisting of a majority single stranded wires, and a few twinned "wishbone" particles (Fig. 4.1). Length of studied particles ranged from 0.5 to 46.1 μm in length and 0.2 to 1.1 μm in width. Out of plane thickness of the wires was not determined in optical experiments. However, atomic force microscopic (AFM) images of several particles (N = 35) show a thickness ranging from 0.1 μm – 0.7 μm. Particle length and width are uncorrelated, however a weak correlation between particle height and

width could be calculated [R^2 = 0.4; (Fig. C-1), [24]]. Individual particle volume is approximated by multiplying the particle area measured in calibrated optical microscopy images by the predicted height from the AFM derived regression function (height = 0.7·width). Differential scanning calorimetry (DSC) of bulk VO_2 samples was conducted on a TA Q2000 using a scan rate of 1 ^oC and calibrated using an Indium melting point standard.

For optical microscopy studies, samples are dispersed by sonication in high purity ethanol. A drop of suspended VO_2 particles is placed on a glass coverslip, and the solvent is allowed to evaporate, dispersing particles on the underlying glass slide. Resulting particles loosely adhere to the glass substrate, held by relatively weak Van der Waals interactions between particles and the substrate. Thus, unlike CVD-grown VO_2 particles, which evidence substantial elastic clamping with the underlying substrate, hydrothermally-grown VO_2 particles are free to deform during nucleation and growth of secondary solid phases.

Optical microscopy was performed using an Olympus BX-53 polarized light microscope, and images were captured on an Olympus UC30 color CCD camera. Images reported in this work were all collected under bright-field reflected un-polarized white light. Under these conditions, light reflected off high temperature rutile (R) domains is visibly blue-shifted with respect to light reflected off low-temperature monoclinic (M1) phase, due to a subtle decrease in reflectivity between 600-800 nm in the R phase [25]. In all cases, exposure was manually selected and held constant through the image series. Sample temperature was controlled with a Linkham LTS120 Peltier temperature stage, which permits control within +/- 0.1 °C from -25 to 120 °C.

4.3 Results and Discussion

4.3.1 Local Transformation in VO_2 Particles

Optical observations of phase transformation in individual undoped VO_2 particles are consistent with nucleation-limited transformation, followed by rapid propagation of a heterophase (M1/R) boundary through a particle volume. Reflected light microscopy shows abrupt transformation within easily distinguishable particles in response to small temperature changes (Fig. 4.1). Regions experience a subtle blue-shift upon transformation to the higher temperature R phase, consistent with UV-Vis spectroscopy which indicates stronger reflection in the red region from the low-temperature M1 phase, providing a convenient method with which to readily distinguish M1 and R phases [25]. At temperatures below or above the critical transformation temperatures, T_{cr}, there are no observable changes in the reflected visible spectrum of a specific volume (Fig. 4.1; Fig. C-3 – C-5, [24]). Thus, phase transformation within domains of undoped VO_2 particles are limited to a relatively narrow temperature difference (< 0.5 ^{o}C), limited only by the temperature resolution of the temperature control stage. Similar abrupt transformation behavior is illustrated both on heating and on cooling.

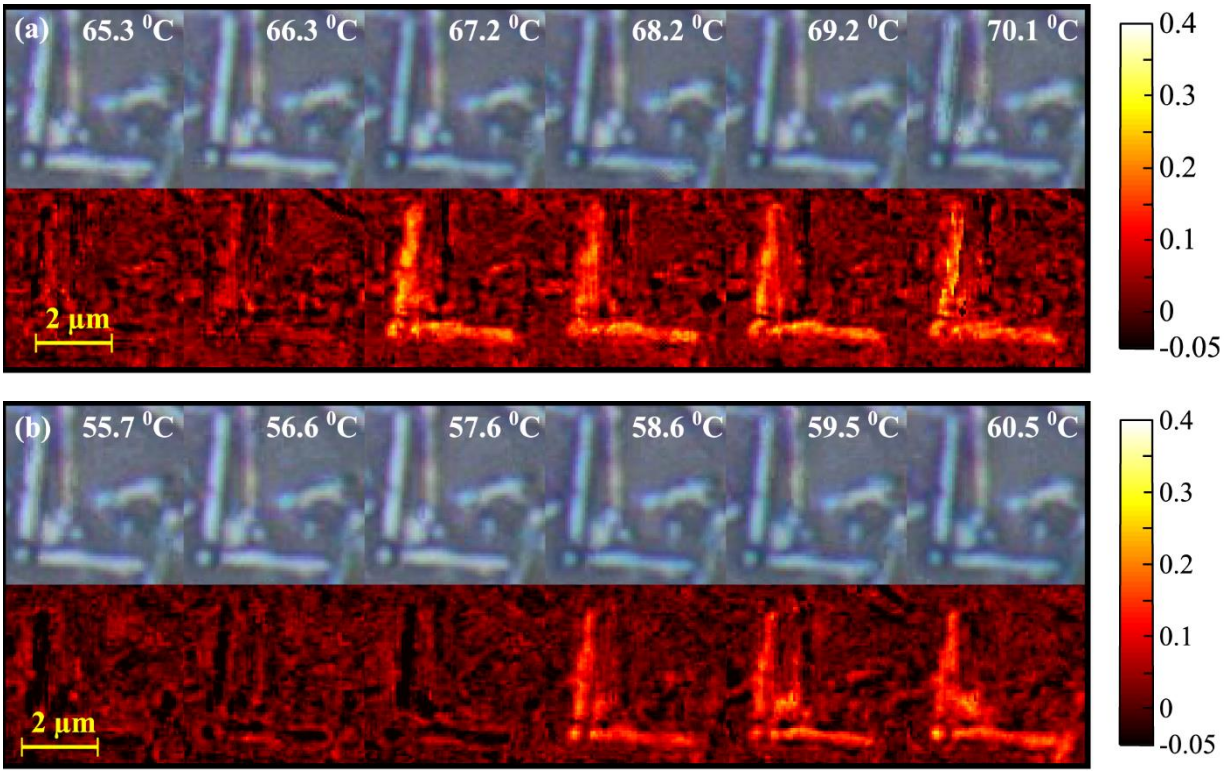

Figure 4.1. Abrupt blue-shift in single VO_2 particles under unpolarized reflected white light and the associated red-difference plots during (a) a heating cycle performed at 1 °C increments (b) the subsequent cooling cycle at 1 °C increments. Difference plots were created by extracting normalized red pixel values, and calculating the difference between a low temperature reference image and high temperature image at each pixel. Reference temperatures were 39.3 ^{o}C during heating, and 54.7 ^{o}C during cooling.

Both forward and reverse transformations in undoped VO_2 particles are consistent with rapid progression from a single, or a very small number of individual nucleation events. In the majority of cases, phase transformation occurs uniformly throughout the entire volume of the particle within one discrete temperature interval (Fig. 4.1, Fig. C - 3, [24]). In the few cases which evidence phase coexistence, discrete domains of the sample transform abruptly, leading to two readily identifiable critical transformation temperatures within a single particle (observed in 6% of particles). The length scale of individual domains is on the orders of microns in length (Fig.

4.2, Fig. C-4, [24]). In those cases which evidence phase coexistence within a single particle, heterophase boundaries separating domains that transform at different T_{cr} are spatially fixed from one cycle to the next (Fig. 4.2, Fig. C-4, [24]), suggesting that phase transformation is impeded by some static defect in the particle, which may correspond with either an internal defect (dislocations, twin plane, etc.) or with some external defect (abrupt crystal facet edge). Thus, the occurrence of discrete transformation of two domains may indicate multiple nucleation events within a single particle, or temporary pinning of a grain boundary, which becomes mobile at a higher temperature. As with all nucleation processes, the stochastic nature of the transformation is evident. For a given region, T_{cr} appears fairly repeatable over multiple cycles, albeit with some degree of stochastic behavior (+/- 1 ^{o}C; Fig. 4.2).

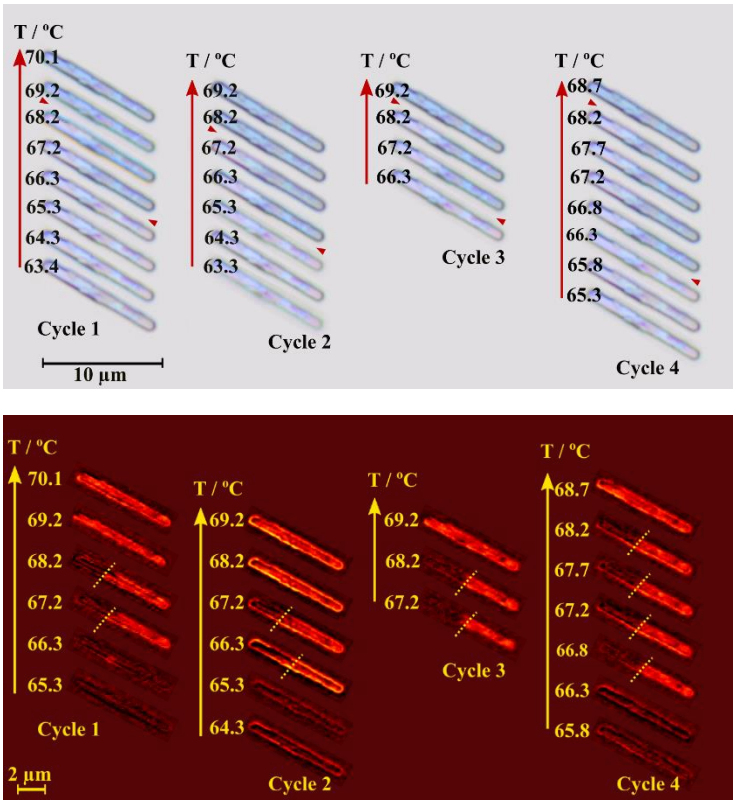

Figure 4.2. A single VO_2 particle showing a two-step pinned transition over the course of 2 °C for four cycles in (a) original bright-field images, and (b) difference plots of the red component between the temperature given and 64.3 °C (cycle 1), 63.3 °C (cycle 2), 66.3 °C (cycle 3) and 65.3 °C (cycle 4).

Abrupt phase transformation in undoped VO_2 suggests that the phase transition is kinetically limited by nucleation of new structural domains within an existing solid phase, rather than by limited mobility of a heterophase interface. Classical heterogeneous nucleation is associated with an energy barrier due to the creation of a heterophase interface with some associated interfacial energy. After such domains are nucleated, growth proceeds spontaneously, driven by the volumetric free energy difference between the two phases. Motion of heterophase boundaries is not observable on the time scales used in optical experiments, suggesting that

heterophase boundary motion is very rapid, consistent with thermally driven transitions previously observed in individual particles below nanosecond timescales [26].

4.3.2 Transformation of Particle Ensembles

Transformation of a collection of undoped VO_2 particles is tracked to understand statistical variations observed within that population. Five areas ~140 x 105 μm containing a large ensemble of VO_2 particles (N = 347) were imaged during heating and cooling by 1 ^oC increments, and transformation temperatures were tracked for individual particles (Fig. C-4, C-5). Particles evidence a distribution of both forward (T_{mean} = 72.2 ^oC, σ ~ 4.4 ^oC) and reverse (T_{mean} = 59.4 ^oC, σ ~ 4.4 ^oC) transformation temperatures (Fig. 4.3). This distribution is dependent on particle volume during both the heating transition and cooling transitions [Fig. 4.3(a)] within the range of particles sampled in this study (0.1 – 28.0 μm^3, Fig. C-2). Importantly, forward and reverse temperatures are only weakly correlated [Fig. 4.3(c)], as would be anticipated if the distribution in transformation temperature was due to a difference in local thermodynamic equilibrium between each particle (e.g., due to variable external strain imposed on an ensemble of particles or variation in oxidation state). Furthermore, it is evident that there is no history effect of the heating transformation which impacts the cooling transition temperature. This distribution of transformation temperatures is consistent with a distribution of potency of nucleation sites for both the forward and the reverse transformations, where the potency of forward and reverse nucleation sites are independent. The range of transformation temperatures between different particles, and between domains within an individual particle (e.g., T_2, T_3, Fig. 4.4) result from differences in the potency of nucleation sites between different domains, each of which require different volumetric free energy driving force (e.g., ΔG_2, ΔG_3) to overcome the barrier to nucleation (Fig. 4.4).

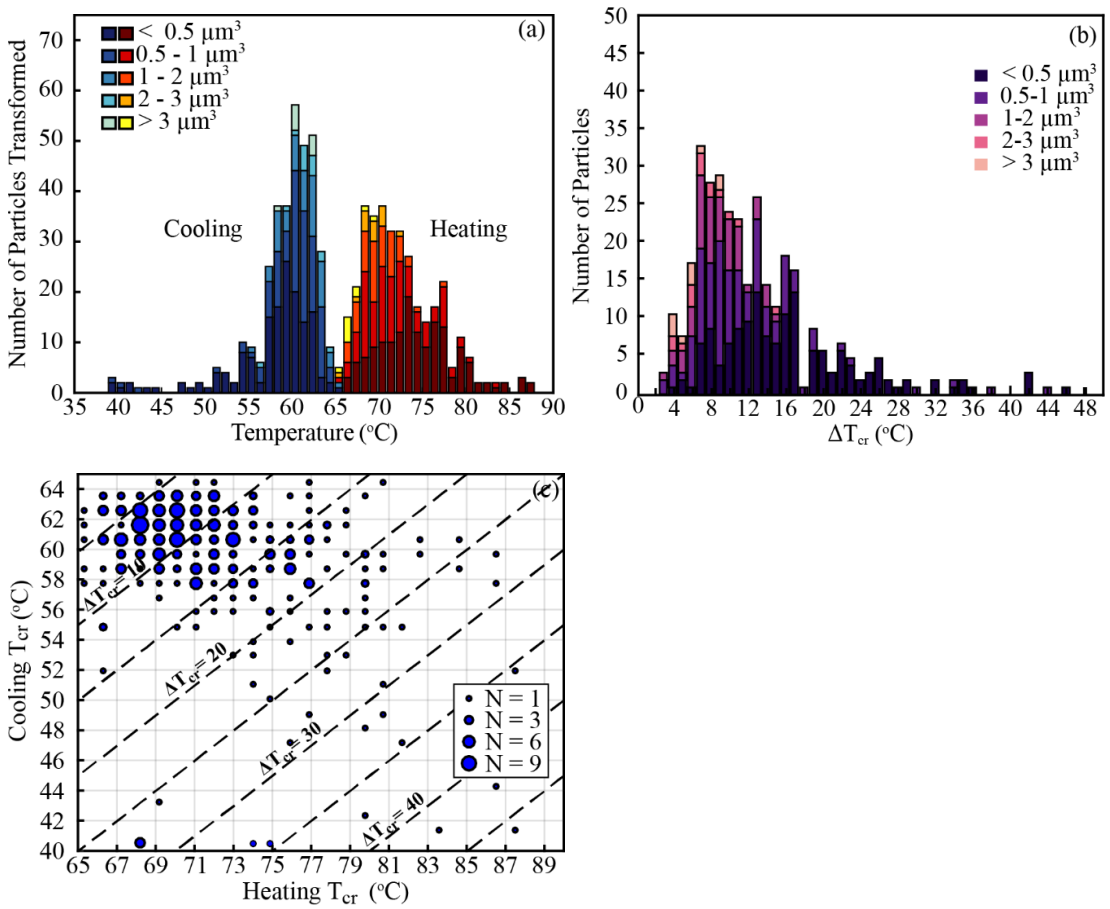

Figure 4.3. (a) Histogram of the transition temperature (heating and cooling) of 347 individual particles observed in optical microscopy, and the calculated (b) histogram of the hysteresis in the same 347 individual particles showing extreme variations in hysteresis width between 2.9 and 46.8 °C. Notably, large hysteresis particles are composed exclusively of small particles (< 2 µm^3). (c) A scatter plot of the individual particle heating and cooling transition temperatures shows little correlation between heating and cooling transitions.

Integrated transformation on a particle basis shows general agreement on cooling and heating with the aggregate phase transformation as measured by differential scanning calorimetry (Fig. C-6). The midpoint of the transition on cooling obtained from DSC and particle counts are 61.0 °C and 59.3 °C, respectively, while the midpoints on heating are 71.4 °C and 71.3 °C. Therefore, the hysteresis obtained from the two data sources are also similar (DSC ΔT_{cr} = 10.4 °C

and optical ΔT_{cr} = 12.0 °C). Deviation of integrated heating transformation signal between DSC and optical counts is most pronounced at higher and lower temperatures, which may indicate a selection bias against smaller particles which occurred during preparation of samples for imaging. Regardless of these small discrepancies, the macroscopic transformation behavior (ΔT_{cr}, heating T_{cr}, and cooling T_{cr}) can be nearly reproduced by the aggregation of microscopic observations in individual particles.

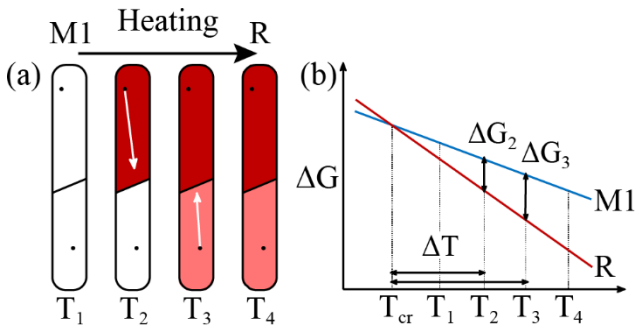

Figure 4.4. a) Phase transformation from the M1 to R phase upon heating in undoped VO_2 occurs abruptly after nucleation of a domain from a potent site (black dot), where (b) nucleation in different domains in triggered at different transformation temperatures (T_2, T_3), depending on the potency of nucleation sites within that domain, and therefore, the thermodynamic driving force (ΔG_2, ΔG_3) necessary to overcome energetic barriers to nucleation. In general, the facile interface passes through the particle leading to complete transformation. In ~4 % of particles, this interface is hindered by some crystal defect, leading to transformation of the particle in 2 to 3 distinct domains.

4.3.3 Statistics of Heterogeneous Nucleation in Undoped VO_2

In order to quantify the densities of active nucleation sites at a given temperature, size-dependent transformation observations in individual particles (Fig. 4.3) are interpreted as the probability of observing at least one active site within a particular particle volume at some

thermodynamic driving force, ΔG (MJ m^{-3}). Here, ΔG represents the excess driving force at some temperature above (below) the bulk transformation temperature (T_c = 65.3 ^{o}C) for both heating and cooling transformations. Near equilibrium, ΔG is proportional to the temperature difference between T_c (equilibrium) and sample temperature [$\Delta G = \Delta S \cdot (T_c - T)$], with an entropy change of 69.2 kJ m^{-3} ^{o}C^{-1} [27].

The cumulative probability, P, of finding at least one active site within a particle volume, V (m^3), is given by:

$$P = 1 - \exp(-N) = 1 - \exp[-V \cdot \rho(\Delta G)], \qquad (4.1)$$

in which N is the mean number of potent sites, ρ is the density of active nucleation sites (sites·m^{-3}) in a given volume at a given thermodynamic driving force. To relate the activity of nucleation sites to the thermodynamic driving force, the density of nucleation sites is assumed to adopt a power-law relationship [16, 28], in which

$$\rho = \alpha \cdot (\Delta G)^{\beta}. \qquad (4.2)$$

Constants α [sites·(m·J^{-1})$^{\beta}$] and β (unit-less) provide acceptable empirical agreement with calculated nucleation densities. From extreme value statistical theory, Eq. 4.1 and Eq. 4.2 together take the form of a Weibull distribution approaching T_c (65.3 ^{o}C) as an upper/lower limit temperature. Thus, α and β derive from a parent distribution of the number of active nucleation sites over a given driving force range, and control the scaling and density of the tails, respectively, of this distribution. The shape and scale of this population of intrinsic defects can be understood to be synthesis and processing dependent. Furthermore, for intrinsic nucleation sites, since the mean number of active sites, N, within a particular volume is $V \cdot \rho$, the cumulative probability of a particle having transformed, P, is a function both of driving force and of particle volume (Fig.

4.5d). Because both modeled and experimentally calculated nucleation densities are dependent on particle volume, the majority of the rather large uncertainty comes from estimated particle volume, and some portion from the estimated population transformation fraction at each temperature.

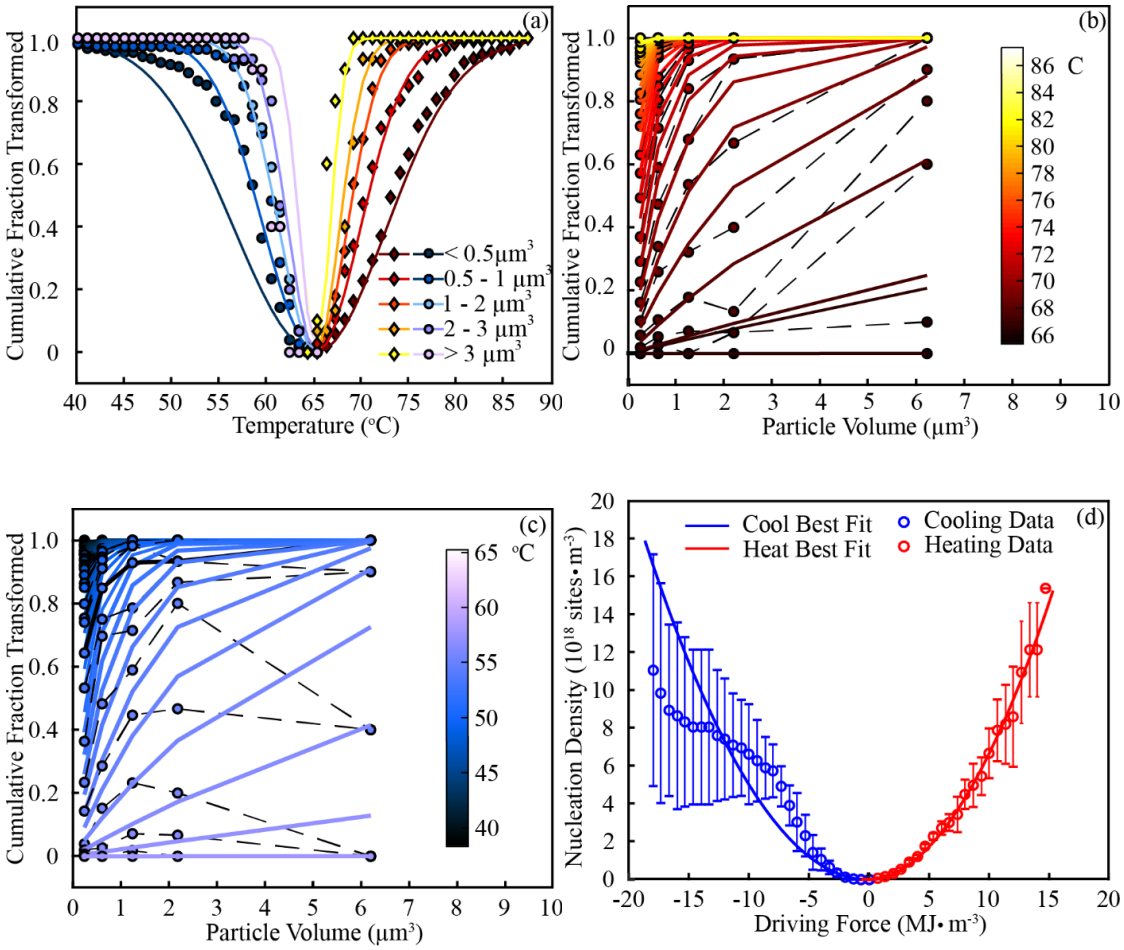

Figure 4.5. (a) Cumulative fraction of particles that have transformed for each volume bin as a function of temperature. (b) The opposite transect showing the dependence of the fraction of particles that have transformed at each given temperature on particle volume during the heating experiment, and (c) during the cooling experiment. In (a) – (c) solid lines represent the best fit of Eqn. 1 on heating (warm colors) or cooling (cool colors), and filled circles or diamonds represent experimentally obtained fractions of particles that have transformed. (d) The calculated potent nucleation site density as a function of driving force according to Eqn. 2. Solid lines represent the best fit to Eqn. 2 on heating (red) and cooling (blue). Open circles represent the solution to Eqn. 1 for ρ using experimentally obtained cumulative transformation fractions (*F*) and volumes (V). Error bars are calculated from error introduced from particle volume and transformation fractions in experimental data.

Fitting parameters are obtained from a least-squares linear regression fit of the entire population, and show little difference between heating and cooling transformations. The α and β parameters, respectively, for heating are (1.4×106 ± 5.6×105, 1.9 ± 0.2), and for cooling transitions are (1.7×104 ± 5.6×105, 2.0 ± 0.2) with 99% confidence intervals reported. A formal hypothesis test shows that there is no statistically significant difference between β on heating and β on cooling ($p = 0.036$, $\alpha = 0.01$). Any difference between obtained fitting parameters on heating and cooling could be interpreted as (1) a difference in both identity and density of the potent sites for each transition or (2) as a difference in potency activation rate with driving force due to the asymmetry of the activation energy barrier between heating and cooling reactions. The slight difference in fitting parameters (α, β) obtained on heating and cooling cannot conclusively distinguish between these scenarios.

Despite these similarities, a deviation between fitted results and experimentally calculated nucleation density values on cooling is observed (Fig. 4.5d), with only a small number of particles ($N = 35$) transforming below -10 $MJ \cdot m^{-3}$ (i.e., at larger undercoolings; C-8c). Fitting a separate function to this subpopulation could indicate two distinct populations of defects operating in different driving force regimes during cooling. However, given the poor counting statistics and large uncertainty on the calculated nucleation density, it seems questionable to interpret the findings of this study beyond an identification of a population of intrinsic defects operating in VO_2 particles, whose potency increases with driving force. Here, intrinsic nucleation sites are differentiated from extrinsic sites based upon the presence of particle volume dependence of transformation events, following conclusions of previous observations of martensitic transformations in small particle alloys and ceramics (FeNi [19], ZrO_2 [29], HfO_2 [28]). For both heating and cooling transitions, the volume dependence and scaling with driving force of the

transformation fraction, F, indicates a population of intrinsic defects sites, such as point defects or dislocations, which are assumed to be sparsely distributed through the particle volume, and whose absolute number therefore increases as the particle size increases.

The β parameters obtained on heating and on cooling are surprisingly similar to the results of Lopez et al for a similar study on ion implantation deposited VO_2 nano-particles [16]. In surface dominated nano-particles, it would be expected that the potent sites would be physically different than those in hydrothermally synthesized micro-particles, with a different rate of potency increase with driving force. In this study, the resulting calculated defect densities are on the order of ~1 x 10^{13} potent sites·cm^{-3} in comparison to the ~1 x 10^{15} sites·cm^{-3} obtained by Lopez et al for a given driving force. This result indicates that the hydrothermal particles used in this study have a much lower defect density than the nano-particles deposited by ion implantation, and could explain why volume dependence of hysteresis is observed far beyond the volume range that this behavior is predicted by studies on VO_2 nano-particles (Fig. 4.6).

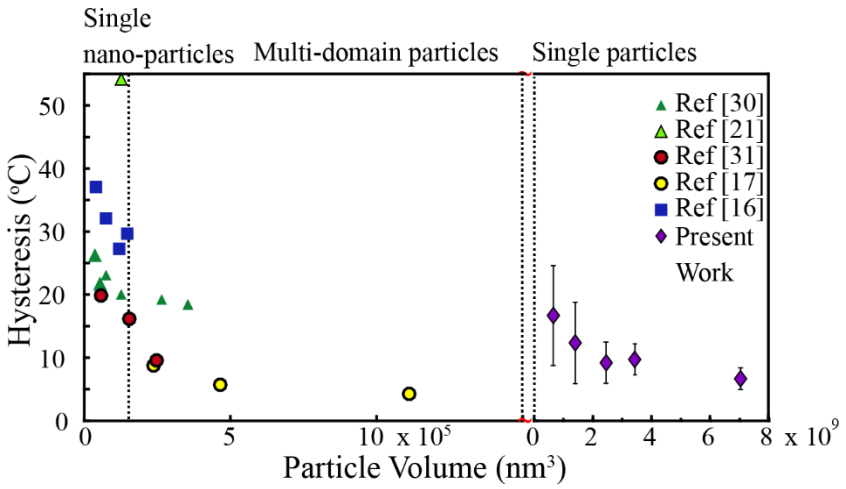

Figure 4.6. Dependence of hysteresis width on particle volume of present work as compared with studies in significantly smaller VO_2 volumes [16, 17, 21, 30, 31].

4.4 Broader Implications for Phase Transformation in VO_2

Undoped VO_2 particles that are elastically coupled to the substrate (e.g., grown by a chemical vapor deposition process) demonstrate significant phase coexistence and a rich diversity of microstructures due to the existence of transformation-induced local strain in those systems [3-6, 9-11, 13]. In contrast, the spontaneous, rapid, and complete transformations observed in most undoped VO_2 particles in this study occur because 1) particles are free to distort as they transform from one crystal structure to another, and 2) particles are small and have low defect densities, enabling a heterophase boundary to travel through a particle unimpeded. As particles grow in size, the likelihood that heterophase boundaries are impeded by internal defects or by some external defect will increase. In these cases, complete descriptions of transformation kinetics require consideration of energetic barriers limiting both nucleation and motion of heterophase boundaries past defects of varying barrier height. However, for the particle sizes investigated here, or within smaller volumes envisioned as the basis for two terminal electronic devices [32], temperature-

induced phase transformations can be well-described by a stochastic nucleation process caused by local fluctuations overcoming some energy barrier to transformation [16].

The hysteresis (or degree of volatility) of the phase transformation has implications for the ability to store some metastable state within the material, or to transform between two states while dissipating relatively small amounts of energy[32]. The entire assemblage of undoped VO_2 particles evidences an extraordinary variation of hysteresis widths (2.9 to 46.3 ^oC). It is reasonable to expect that this variation of hysteresis widths would increase as VO_2 volumes are scaled down to relevant length for microelectronics due to a similar probability of finding a potent nucleation site within a particular volume. This would be anticipated even in VO_2 synthesized by different approaches containing different overall densities of nucleation sites.

The implication for hysteresis engineering of coupled electronic-structural phase transformations in VO_2 is clear. To reduce the magnitude of hysteresis observed within a given volume requires introducing potent nucleation sites for both the M1 to R and R to M1 transformations. Defect (vacancies or interstitials) introduction, aside from by applying external stress, might occur up to a certain limit by α-particle bombardment [18], chemical-doping [23, 33], or electron-beam irradiation [29]. Thus, required temperatures or switching voltages might be reduced, and hysteresis widths systematically engineered.

4.5 Conclusions

In summary, we have directly shown that hysteresis width of the M1/R phase transition in un-doped, unstrained hydrothermally synthesized VO_2 particles is primarily controlled by the availability of nucleation sites in individual particles. Growth of daughter phases observed by optical microscopy is much faster than can be observed at experimental time-scales, and are not

kinetically limiting. Instead, a distribution of nucleation sites with variable nucleation barrier heights between individual particles, or domains separated by internal defects, reproduces the macroscopically observed transformation hysteresis width. Moreover, the transformation temperatures upon heating and cooling are not correlated, indicating separate distributions of nucleation sites upon heating and cooling, rather than any local thermodynamic variability. The implications for VO_2 based device engineering are that introduction of potent nucleation sites is necessary for ΔT_{cr} reduction, especially at high-density, scaled-down dimensions.

4.6 References

[1] Ladd L A and Paul W 1969 Optical and transport properties of high quality crystals of V2O4 near the metallic transition temperature *Solid State Communications* **7** 425-8

[2] Guiton B S, Gu Q, Prieto A L, Gudiksen M S and Park H 2005 Single-crystalline vanadium dioxide nanowires with rectangular cross sections *Journal of the American Chemical Society* **127** 498-9

[3] Cao J, Ertekin E, Srinivasan V, Fan W, Huang S, Zheng H, Yim J, Khanal D, Ogletree D and Grossman J 2009 Strain engineering and one-dimensional organization of metal–insulator domains in single-crystal vanadium dioxide beams *Nature nanotechnology* **4** 732-7

[4] Wu J, Gu Q, Guiton B S, de Leon N P, Ouyang L and Park H 2006 Strain-induced self organization of metal− insulator domains in single-crystalline VO2 nanobeams *Nano letters* **6** 2313-7

[5] Tselev A, Strelcov E, Luk'yanchuk I A, Budai J D, Tischler J Z, Ivanov I N, Jones K, Proksch R, Kalinin S V and Kolmakov A 2010 Interplay between Ferroelastic and Metal− Insulator Phase Transitions in Strained Quasi-Two-Dimensional VO2 Nanoplatelets *Nano letters* **10** 2003-11

[6] Cao J, Gu Y, Fan W, Chen L, Ogletree D, Chen K, Tamura N, Kunz M, Barrett C and Seidel J 2010 Extended mapping and exploration of the vanadium dioxide stress-temperature phase diagram *Nano letters* **10** 2667-73

[7] Qazilbash M, Brehm M, Andreev G, Frenzel A, Ho P-C, Chae B-G, Kim B-J, Yun S J, Kim H-T and Balatsky A 2009 Infrared spectroscopy and nano-imaging of the insulator-to-metal transition in vanadium dioxide *Physical Review B* **79** 075107

[8] Frenzel A, Qazilbash M M, Brehm M, Chae B-G, Kim B-J, Kim H-T, Balatsky A, Keilmann F and Basov D 2009 Inhomogeneous electronic state near the insulator-to-metal transition in the correlated oxide VO 2 *Physical Review B* **80** 115115

[9] Jones A C, Berweger S, Wei J, Cobden D and Raschke M B 2010 Nano-optical investigations of the metal− insulator phase behavior of individual VO2 microcrystals *Nano letters* **10** 1574-81

[10] O'Callahan B T, Atkin J M, Jones A C, Park J H, Cobden D and Raschke M B 2015 Inhomogeneity in the ultrafast insulator-to-metal transition dynamics in VO2 *Nature Communications* **6**

[11] Guo H, Chen K, Oh Y, Wang K, Dejoie C, Syed Asif S, Warren O, Shan Z, Wu J and Minor A 2011 Mechanics and dynamics of the strain-induced M1–M2 structural phase transition in individual VO2 nanowires *Nano letters* **11** 3207-13

[12] Chang Y, Yang J, Kim Y, Kim D, Noh T, Kim D-W, Oh E, Kahng B and Chung J-S 2007 Surface versus bulk characterizations of electronic inhomogeneity in a V O 2 thin film *Physical Review B* **76** 075118

[13] Tselev A, Luk'Yanchuk I, Ivanov I, Budai J, Tischler J, Strelcov E, Kolmakov A and Kalinin S 2010 Symmetry relationship and strain-induced transitions between insulating M1 and M2 and metallic R phases of vanadium dioxide *Nano letters* **10** 4409-16

[14] Vardi N, Anouchi E, Yamin T, Middey S, Kareev M, Chakhalian J, Dubi Y and Sharoni A 2017 Ramp-Reversal Memory and Phase-Boundary Scarring in Transition Metal Oxides *Advanced Materials* **29**

[15] Yoon J, Kim H, Chen X, Tamura N, Mun B S, Park C and Ju H 2016 Controlling the Temperature and Speed of the Phase Transition of VO2 Microcrystals *ACS applied materials & interfaces* **8** 2280-6

[16] Lopez R, Haynes T, Boatner L, Feldman L and Haglund Jr R 2002 Size effects in the structural phase transition of VO 2 nanoparticles *Physical Review B* **65** 224113

[17] Appavoo K, Lei D Y, Sonnefraud Y, Wang B, Pantelides S T, Maier S A and Haglund Jr R F 2012 Role of defects in the phase transition of VO2 nanoparticles probed by plasmon resonance spectroscopy *Nano letters* **12** 780-6

[18] Fan W, Cao J, Seidel J, Gu Y, Yim J, Barrett C, Yu K, Ji J, Ramesh R and Chen L 2011 Large kinetic asymmetry in the metal-insulator transition nucleated at localized and extended defects *Physical Review B* **83** 235102

[19] Olson G, Tsuzaki K and Cohen M 1985 Statistical aspects of martensitic nucleation *MRS Online Proceedings Library Archive* **57**

[20] Cech R and Turnbull D 1956 Heterogeneous nucleation of the martensite transformation *JOM* **8** 124-32

[21] Donev E, Ziegler J, Haglund Jr R and Feldman L 2009 Size effects in the structural phase transition of VO2 nanoparticles studied by surface-enhanced Raman scattering *Journal of optics A: pure and applied optics* **11** 125002

[22] Suh J Y, Lopez R, Feldman L C and Haglund Jr R 2004 Semiconductor to metal phase transition in the nucleation and growth of VO 2 nanoparticles and thin films *Journal of Applied Physics* **96** 1209-13

[23] Braham E J, Sellers D, Emmons E, Villarreal R, Asayesh-Ardakani H, Fleer N A, Farley K E, Shahbazian-Yassar R, Arròyave R and Shamberger P J 2017 Modulating the

Hysteresis of an Electronic Transition: Launching Alternative Transformation Pathways in the Metal—Insulator Transition of Vanadium (IV) Oxide *Chemistry of Materials* **30** 214-24

[24] O'Dwyer J J 1973 *The theory of electrical conduction and breakdown in solid dielectrics*: Clarendon Press)

[25] Barker Jr A, Verleur H and Guggenheim H 1966 Infrared optical properties of vanadium dioxide above and below the transition temperature *Physical Review Letters* **17** 1286

[26] Sharoni A, Ramírez J G and Schuller I K 2008 Multiple avalanches across the metal-insulator transition of vanadium oxide nanoscaled junctions *Physical review letters* **101** 026404

[27] Berglund C and Guggenheim H 1969 Electronic Properties of V O 2 near the Semiconductor-Metal Transition *Physical Review* **185** 1022

[28] Chen I-W, Chiao Y and Tsuzaki K 1985 Statistics of martensitic nucleation *Acta Metallurgica* **33** 1847-59

[29] Chen I-W and Chiao Y 1985 Theory and experiment of martensitic nucleation in ZrO2 containing ceramics and ferrous alloys *Acta Metallurgica* **33** 1827-45

[30] Donev E U, Lopez R, Feldman L C and Haglund Jr R F 2009 Confocal Raman Microscopy across the Metal− Insulator Transition of Single Vanadium Dioxide Nanoparticles *Nano letters* **9** 702-6

[31] Appavoo K and Haglund Jr R F 2011 Detecting nanoscale size dependence in VO2 phase transition using a split-ring resonator metamaterial *Nano letters* **11** 1025-31

[32] Zhou Y and Ramanathan S 2015 Mott memory and neuromorphic devices *Proceedings of the IEEE* **103** 1289-310

[33] Alivio T E, Sellers D G, Asayesh-Ardakani H, Braham E J, Horrocks G A, Pelcher K E, Villareal R, Zuin L, Shamberger P J and Arroyave R 2017 A Post-Synthetic Route for Modifying the Metal—Insulator Transition of VO2 by Interstitial Dopant Incorporation *Chemistry of Materials* **29** 5401-12

5. THERMAL PROGRAMMING OF BORON DOPED VO_2 METAL INSULATOR TRANSITION DEVICES

5.1 Introduction

The first order martensitic phase transition in the correlated-electron transition metal oxide VO_2 is accompanied by an orders of magnitude change in resistivity across the phase transition, making this material a promising candidate to enable functionality in neuromorphic computing architectures [1, 2]. Neuromorphic device integration and demonstration of critical functionalities including device resistance switching [3], action potential generation [4] and self-oscillations [5] have already been explored in the metal-insulator transition in NbO_2 at higher temperature (1080 K) [6]. In contrast to NbO_2, the structural transition of VO_2 occurs at much lower temperature (67 ^oC) from the low-temperature monoclinic ($P2_1/c$) semiconducting phase (E_g = 0.457 eV) to the high temperature rutile ($P4_2/mnm$) phase [2]. Furthermore, the phase transition can be driven not only thermally, but by application of optical pulses[7, 8], stress[9, 10], and crucially for device application, by current or voltage application [11, 12]. The latter drives the metal-insulator transition (MIT) indirectly, as application of current in constrained VO_2 volumes drives localized joule heating, which can locally raise the temperature in the structure above the critical transition temperature [11]. While some question as to the role of electric field in switching has been raised [13, 14], thermal imaging and modeling has conclusively attributed the current driven phase change to an indirect thermal mechanism at low electric fields [11]. Therefore, resistance switching of devices in which the transition is current driven should closely mirror resistance switching in thermally driven devices. Moreover, extensive work in VO_2 has demonstrated that introduction of point defects can alter key transition properties including transition temperature, hysteresis, and

width of the transition. In particular, interstitial doping with boron has demonstrated a unique dynamic component of the thermal hysteresis dependent on the thermal history. Taken together with indirect thermal driving of the MIT by current application, we anticipate that similar dynamical behavior as has been observed in bulk B-doped VO_2 powders should be faithfully recreated in electronically driven two-terminal devices.

Chemical doping of VO_2 is understood to modify the equilibrium crystal and electronic structure of the high and low-temperature phases, thereby modifying critical transformation temperatures in the system. In particular, substitutional W dopants have been shown to decrease the stability of the M1 phase relative to the R phase at lower temperatures via introduction of anisotropic strain gradients (due to its larger ionic radius) as well as by introduction of added electron density [15, 16]. Dopants such as Cr^{3+} and Al^{3+} lower the resistivity of the M1 phase [17], as well as stabilizing the M2 or T polymorphs [18, 19] . As is less commonly observed, Ti doping is proposed to increase the critical transformation temperature by suppression of Mott physics [20, 21]. At the same time, substitutional doping creates heterogeneous internal strain and is associated in some cases with a dramatic decrease in the size of nucleating daughter domains within a parent phase (< 10 nm) [22]. This internal strain is also associated with an extended range of phase coexistence, which translates into a broader transition and extended resistance loop over the transition temperature span [23, 24]. Therefore, substitutional dopants alter thermodynamic stabilities of the phases with respect to each other as well as activation energy barriers between the phases, providing the ability to tune phase transition parameters underlying device function, albeit in a static and non-reversible manner.

In contrast, the diffusive incorporation of interstitial boron dopants has been demonstrated not only to depress phase transition temperatures (~10 ^{o}C/ at. %) [25], but also to asymmetrically

alter the M1 to R transition temperature (T_h) depending on time and temperature spent below the transition point, while the R to M1 transition temperature (T_c) is unaltered [26]. The proposed mechanism indicates the trapping of boron in metastable interstitial lattice sites upon the symmetry breaking transition from R to M1, upon which boron dopants diffusively relax within the newly formed monoclinic lattice to a more thermodynamically stable coordination. Time and temperature allows for boron atoms to undergo this diffusive relaxation and alter the relative populations in metastable and stable M1 states, thereby altering the temperature of the subsequent M1 to R transition. This introduction of an additional kinetic diffusive barrier to the energy landscape of the martensitic phase transition promises the potential to create modulated resistance states depending not just on thermal history, but also on time dependent thermal history. The diffusive dynamics of such time dependent resistance modulation underlies the function of "second-order" memristors [27, 28], which more closely mimic the plasticity demonstrated by biological synapses [29] than the memory-optimized resistance switching demonstrated in other metal-oxide memristors [30].

Here, we demonstrate a 'proof-of-concept' for diffusive dynamics of resistance modulation in B-doped VO_2 by the fabrication and testing of two-terminal resistance switching devices. Current driven switching of devices is demonstrated and as the relaxation time and temperature increase, critical switching current also increases, consistent with results of relaxation experiments in thermally driven switching devices. Devices show repeatable and consistent switching, albeit with lowered resistance ratios (as compared to undoped VO_2 devices) of the insulating high resistance state to the metallic low resistance state, consistent with the extrinsic doping of the semiconducting M1 phase. Besides the evolution of the critical switching current as a function of relaxation time, the resistance state of the M1 phase itself increases gradually as a function of time

associated with changes in local electronic structure stemming from changes in boron interstitial site occupation. Thus, in addition to the current pulse amplitude, resistance states and critical switching parameters can be tuned by relaxation time and relaxation temperature. This introduction of additional variables with which to tune device resistance make B_xVO_2 a possible candidate for "plasticity" enabled memristor devices, and recommendations for further device programming sequences are posited.

5.2 Methods

5.2.1 VO_2 and B_xVO_2 Synthesis

Single crystal particles of VO_2 were synthesized hydrothermally from bulk V_2O_5 powder (Beantown Chemicals) a reducing agent of high purity acetone (Sigma Aldrich). Samples were prepared with 300 mg V_2O_5, 9 mL of acetone, and 7 mL of deionized water (ρ= 18.2 MΩ cm-1, Barnstead International NANOpure Diamond ultrapure water system). The mixtures were placed in 23 mL polytetrafluoroethylene cups and heated in a high pressure autoclave reactor at 250 °C for 72 hours. Samples were recovered by vacuum filtration and washed three times with deionized water and acetone. To relieve any strain from synthesis, samples were annealed under Ar (g) at 550°C for 3 hours.

B-doped VO_2 was produced by a post-synthesis diffusive process. 2-Allyl-4,4,5,5tetramethyl-1,3,2-dioxaborolane (97%) was purchased from SigmaAldrich (St. Louis, MO). In a typical reaction, 20 mg of VO_2 nanoparticles was dispersed in 1.00 mL of mesitylene by ultrasonication, and 200 μL of 2-allyl-4,4,5,5-tetramethyl-1,3,2-dioxaborolane was added to the reaction mixture. The reactants were allowed to stir for 2.5 h at 120 °C under an Ar ambient in a Schlenk flask. The VO_2 nanowires were then recovered by centrifugation and then rinsed with

toluene. Next, the nanowires were annealed using a 2 mL porcelain combustion boat (VWR, Sugar Land, TX) to a temperature of 900 to 950 °C for 1 min under an Ar ambient in a quartz tube furnace (rapidly ramping at a rate of ca. 45 °C/min).

5.2.2 Materials Characterization

DSC characterization was performed on a TA instruments Q2000 instrument with ramp rates of 1 to 10 ^{o}C/min using N_2 purge gas.

SEM images were obtained on a Tescan Lyra and Mira3 instrument with accelerating voltage of 20 kV after dispersing particles in ethanol and pipetting onto Al/Si substrates. Scanning electron micrographs demonstrated a noticeable difference in the size distributions and morphology of particles between undoped and B-doped samples (Fig. 1b). The morphology of undoped VO_2 particles consisted of a wire-like geometry, with lengths 4.0 ± 3.0 μm and widths 210 ± 70 nm [31]. Electrode spacing of 4 μm imposed a sampling selection on devices, with volumes of tested devices 3.7 μm^3 ± 2.4 μm^3, as measured by atomic force microscopy of individual devices (Fig. C-2). Boron-doped particles presented a more challenging morphology for device fabrication with particles 3 – 4 μm in length and 1 – 3 μm in width, for a final mean volume of 2.1 ± 1.8 μm^3, at the larger end of the size distribution for these samples.

Powder X-ray diffraction (XRD) patterns were acquired using a Bruker D8-Vario X-ray powder diffractometer equipped with a Cu Kα (λ = 1.5418Å) source and operated at an accelerating voltage of 40 kV. Powder XRD patterns were measured for $B_{0.05}VO_2$, $B_{0.02}VO_2$, and undoped VO_2 samples. At room temperature, indexing of patterns in the undoped sample and low-doped $B_{0.02}VO_2$ indicates that these samples are matched to VO_2's M1 monoclinic phase (space group $P2_1/c$) and while indexing of the $B_{0.05}VO_2$ matches with VO_2's rutile phase (space group $P4_2/mnm$; Fig. 5.1a). This difference in phase is consistent with the destabilization of the M1 phase at room

temperature in favor of the R phase (10 ^{o}C/at. % B) so that the more highly doped sample is predominately in the rutile phase even at room temperature. Comparison of XRD patterns between the undoped and $B_{0.02}VO_2$ sample in the monoclinic phase at 25 ^{o}C shows that in the $B_{0.02}VO_2$ sample several of the reflections are observed to be shifted to lower 2θ values as compared to the undoped sample. Because all peaks associated with the M1 phase are shifted, a marginal isotropic lattice expansion is associated with the incorporation of interstitial B atoms. Reflections derived from a minority V_8O_{15} Magneli phase are identified and are thought to arise from increased VO_2 reduction but do not contribute to the observed MIT behavior since the transition temperature for this phase is 70 K [32]. However, no evidence is observed for the presence other polymorphs of VO_2 (M2, T, VO_2(B), VO_2(A)). Thus boron dopant inclusion leads to only slight lattice expansion as expected from its' relatively small ionic radius and does not serve to stabilize alternate VO_2 phases associated with external strain [10] or large internal strain from substitutional doping with relatively large ionic radius cations [16, 19].

5.2.3 Two-terminal Device Fabrication:

Two terminal devices based on hydrothermally synthesized boron doped and undoped VO_2 particles were fabricated using standard photolithographic processes for resist patterning, followed by the e-beam evaporation deposition and lift-off of Cr (50 nm)/Ni (450 - 900 nm thick)/Au (50 nm) metal electrodes. Particles from samples with a range of boron dopant concentration which demonstrated significant ranges of transition temperature in bulk differential scanning calorimetry characterization were dispersed in high purity isopropanol at low concentrations by sonication. Solutions were subsequently pipetted onto an insulating SiO_2 film (500 - 600 nm thick) grown by plasma enhanced chemical vapor deposition on polished Si substrates (<100>, Nova Electronics), or directly onto polished fused quartz substrates (University Wafer). The resulting distribution of

particle orientations and concentrations on the substrate surface was random. On fused quartz substrates, particles which tended to congregate upon solvent evaporation were mechanically redistributed by gently passing another wafer over the surface several times. Enough particles were spatially separated from their neighbors and lay between electrode lines to make this a viable approach. Electrodes were laid out with a four probe pad geometry connected to interdigitated lines varying in width (2 μm – 4 μm) and spacing (2 μm – 4 μm). Standard photolithography using a dual resist profile (Microchemical LOR 10A/AZ5214) was employed for lift-off patterning with a combined profile of 2.4 μm being sufficient to cover the height of the particles and provide for lift-off of thick metal films. Dilute tetramethylammonium hydroxide (3%) solution (Microchemicals AZ726) was used as the resist developer and is not expected to participate in a detrimental chemical reaction with VO_2. Lift-off was performed in acetone and photoresist stripper (Microchemicals AZ400T) at 90 ^oC with the time of exposure to these chemicals minimized in order to prevent further oxidation of VO_2 particles.

5.2.4 Electrical Characterization:

In order to continuously measure resistance as function of temperature, electrical characterization was conducted on a Keithley 2450 Source Meter sourcing 20 mV across two terminals in conjunction with a Linkam 120-PE temperature stage. Ramp rates of 5 ^oC/min were used, with a temperature accuracy of ±0.1 ^oC. Electrical characterization was carried out only on particles that demonstrate a shift in reflected blue light under bright-field unpolarized optical microscopy, indicative of a particle that is confirmed to undergo a phase transition. Tested particles which do not exhibit this shift were found to be of lower resistivity and did not demonstrate a metal-insulator transition, likely due to an alternate oxide stoichiometry (V_4O_7, V_2O_5, V_6O_{13} etc).

The phase transition was also driven in B-doped devices by sweeping current in a quasi-4 point configuration using a Keithley 6221 current source and Keithely 2182A nano-voltmeter. Here, current densities on the order of (1 x 10^9 A m^{-2}) induced joule-heating within the oxide volume and increased the local temperature above the transition temperature, enabling a much quicker path for driving the heating transition [12]. The base temperature of the device and substrate were held constant by the Linkam temperature stage at incremented temperatures below the cooling transition temperature for a period of at least 5 minutes before a current sweep was initiated. Removal of the current source caused the device to return to the insulating M1 phase immediately (ns time scale) [12]. Current sweeps were carried out as pulsed IV sweeps using a pulse length of 2 ms with a measurement settle time of 0.2 ms and with ~83 ms between pulses (5 NPLC). Sweep timing ranged from 20 s to 50 s, dependent on the number of points measured.

5.3 Results & Discussion

5.3.1 Materials Characterization and Effect of Boron on Thermal Hysteresis

Doping of VO_2 with boron in interstitial sites was achieved through a post-synthetic diffusive method, the detailed results of which have been described elsewhere [33]. Moreover, detailed exploration of the impact of boron on kinetic hysteresis and support for a proposed mechanism is developed in another contribution [26]. A brief summary of the findings in bulk powders is reported here to give a background to which results in devices may be compared.

Differential scanning calorimetry (DSC) in bulk boron doped powders and in bulk undoped powder samples was employed to reveal differences wrought by boron doping in the phase transition, as previously reported in detail elsewhere [31]. DSC characterization of undoped powders showed relatively narrow peaks with peak transition temperatures (T_h on heating and T_c

on cooling) near reported values of the M1 to R transition (67 ^{o}C) and (62 ^{o}C) with a narrow hysteresis (ΔT = 5 ^{o}C). In contrast, B-doped samples showed broad peaks (related either to variations in incorporated B dopant concentration or to wider transition widths among or within individual particles), with peak transition temperatures varying as a function of boron dopant concentration (10 ^{o}C/at.% B) as previously reported [31] (Fig. 5.1c). The enthalpy change of the M1 to R transformation related to the structural rearrange of the lattice was 15.69 J/g in undoped samples (considerably less than the enthalpy 52.45 J/g reported by Cook *et al.* [34]), indicating that some fraction of the sample was composed of volumes that did not transform associated with the presence of the minor phases. Notably, in this electron-correlated oxide, changes in phonon entropy and conduction electron entropy due to charge ordering/delocalization resulting from the accompanying modulation of the bandgap could be further impacted by boron dopant inclusion[35, 36].

Most interestingly, remarkable changes in the dependence of ΔT on ramp-rate (or thermal history) were observed with DSC upon boron dopant inclusion. In undoped VO_2, as ramp-rate is decreased (equivalently more time is spent below the transition temperature) the transition temperature on both heating and cooling is decreased and increased respectively, leading to a kinetically derived degree of superheating or supercooling [37]. Such a shift is consistent with nucleation limited transformation kinetics, in which a nucleation barrier at volume distributed potent nucleation sites (oxygen vacancies [38]) must be overcome before propagation of the nascent phase front proceeds in a ‘burst’ often observed in other martensitic systems [39]. Arrhenian models predict that as more time is spent near (but still below) the transition temperature, a greater probability of certain nuclei growing past the critical nucleation radius is possible and the overall degree of supercooling or superheating is reduced. Moreover, the degree

of supercooling and superheating dependence on ramp rate is nearly symmetric in both heating and cooling transitions.

By contrast, the kinetic dependence of ΔT in B-doped samples is remarkably asymmetric, with the R to M1 transition temperature unchanged as a function of thermal history, while the M1 to R transition temperature is increased as a quasi-exponential function of time and temperature below the transition temperature [26]. Here, ramp-rate dependence of the cooling transition indicates that nucleation sites are suitably potent or dense in order to cause no dependence of Tc on ramp rate. In the heating transition, the kinetic situation is more complex. Three separate thermal profiles were applied to a $B_{0.02}VO_2$ sample allowing for increasing amounts of time spent below the transition temperature termed: unrelaxed, intermediate, and relaxed. For this sample, a 12 ^{o}C difference between the unrelaxed and relaxed *T*h transitions is observed (Fig. 5.1c). Extensive DFT modeling and x-ray absorption near edge structure (XANES) characterization points to a mechanism which posits the trapping of boron atoms in metastable states following the cooling transition from the high symmetry R phase to the low symmetry M1 phase [26]. Here, the M1 to R phase transition from this metastable state can occur at a much lower temperature than from the minimum energy state, in which boron atoms have thermally relaxed to energetically stable positions within the M1 unit cell. This observed kinetic relaxation has the potential to enable unique device state modulation by introducing controllable changes in the transition temperature, and by extension, a critical switching current.

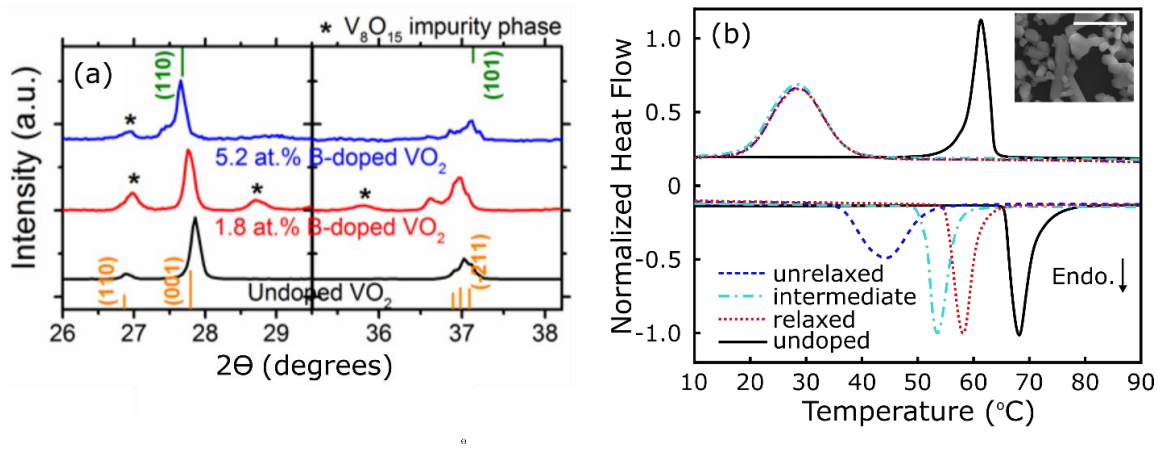

Figure 5.1. Characterization of both undoped VO_2 and B-doped samples with (a) powder XRD patterns measured for $B_{0.05}VO_2$ (blue), $B_{0.02}VO_2$ (red), and undoped VO_2 (black) samples in the 2Θ range from 26 to 38°. Reflections corresponding to the M1 phase of VO_2 are plotted as orange ticks on the bottom axis as per JCPDS/PDF card no. 043-1051, whereas reflections corresponding to the R phase of VO_2 are plotted as green ticks on the top axis as per JCPDS/PDF card no. JCPDS 79-1655. Reflections derived from a minority V_8O_{15} Magneli phase denoted with an asterisk [26]. DSC characterization of (b) $B_{0.02}VO_2$ samples in the unrelaxed state (blue dashed line), and after thermal relaxation at room temperature for 40 days, corresponding to an intermediate relaxed state (cyan dash-dot line) and after 323 days, corresponding to a relaxed structure (red dotted line). The obvious shift in T_h observed for these traces is in contrast with the relaxation independent undoped VO_2 trace (black line). All traces were run at a ramp rate of 10 °C/min [26]. Inset: SEM image of individual $B_{0.02}VO_2$ particles with scale bar representing 2 µm.

5.3.2 Effect of B doping on Electronic Transport and Phase Transition

To prove the efficacy of boron-doped VO_2 as a material for electronic resistance switches, devices are fabricated from samples of varying B-dopant concentration (B_xVO_2, $0 < x < 0.3$) and electrical transport measurements used to characterize device behavior. Fabricated devices were also cycled thermally with different isothermal conditions before use in current driven device studies to unambiguously demonstrate that boron doping, instead of another electric field created defect, is responsible for the unique kinetic control of switching parameters observed.

Undoped VO_2 particles (T_c ~ 67 ^oC) were used as a test case for device fabrication due to their well characterized transformation behavior (temperature, hysteresis, optical reflectance change, and changes in resistivity). Measured resistance ratios across the metal-insulator transition ranged from 10^2 - 10^5 within a sample of 8 particles, consistent with results from other studies on high-quality VO_2 single crystals [23]. In general, transitions were sharp, occurring over a temperature span (< 0.1 ^oC) and showed a thermal hysteresis (ΔT) of 5 – 8 ^oC, also consistent with previous optical and bulk powder characterization (Fig. 5.2a) [40]. Therefore, although particles are weakly bound to the substrate surface and the electrodes could limit contraction or elongation along the c-axis of the particle during phase transformation, these stresses are not high enough to introduce the patterned phase coexistence observed in VO_2 wires which are clamped to the substrate [41]. Interestingly, a small number of particles showed 2 or more step transitions, consistent with pinning of the transition front at large scale defects previously observed in optical microscopy [40]. However, this multi-step transition collapsed to a single transition upon repeated cycling (Fig D-1). Devices were shown to demonstrate stable switching after storage of 3 months under inert atmosphere (Ar) in a glove-box, although transitions showed greater inter-cycle deviation during the first 10 cycles before reaching a lower variability state during cycling (Fig. D-1). Thus, device fabrication and characterization of undoped VO_2 wires demonstrated stable resistance switching consistent with other reports [12], confirming that the device fabrication process did not introduce any chemical degradation or mechanical strain that might impact the phase transition.

In comparison to the phase transition in individual undoped VO_2 devices, the phase transition observed in B-doped VO_2 devices demonstrates several key differences. Transition temperatures are depressed in individual particles as in bulk powder samples as a function of B at.

% concentration [25]. Moreover, heating and cooling transitions often occurred over a series of steps, with the number of steps during the cooling transition (>5 on average) greater than the number of steps on heating (< 3) and transitions show some stochasticity in the number and magnitude of steps between cycles (Fig. D-1b). Transition widths thus range from < 0.1 ^{o}C to 20 ^{o}C in B-doped devices indicating a prolonged region of phase coexistence in some cases. While boron does not impose significant strain on the lattice [25], electronic instability and distortion of the local environment around the interstitial B atom could pin advancing phase fronts as well as introduce domain walls, consistent with observations of VO_2 doped with W in similar concentration ranges to those examined here [15, 22, 42]. Thermal hysteresis in B-doped VO_2 devices demonstrates the unique history dependence of the heating transition temperature, and therefore thermal hysteresis, observed in bulk powders. In general, ΔT of the phase transition in B-doped VO_2 particles ($\Delta T > 20$ ^{o}C) is much larger than that in undoped VO_2 devices ($\Delta T < 5$ ^{o}C), despite the similar volume of the particle which should provide for a great number of nucleation sites and therefore a lower hysteresis than in their undoped counterparts. Tested thermal cycles consisted of two conditions: “relaxed” and “unrelaxed”. In “relaxed” cycles, the device was maintained at room temperature for a long period of time (1 - 21 days) before ramping to 65 ^{o}C at 5 ^{o}C/min to observe T_h, and then to 10 ^{o}C to observe T_c. For “unrelaxed” cycles, temperature was ramped between 10 ^{o}C and 65 ^{o}C at 5 ^{o}C/min with no pause between the end of the last cycle and the beginning of the next. Between the two conditions, tested devices demonstrated an almost 4 - 10 ^{o}C difference in T_h (Fig. 5.2b). Peculiarly, the relaxed T_h is consistently around 60 ^{o}C dependent on time but irrespective of dopant concentration, while the unrelaxed T_h varies as a function of boron dopant concentration, as is concluded in bulk samples [26]. Thus, results at the individual device basis replicate bulk powder characterization results in the observation of a time dependent

component of the hysteresis, as well as in observed transition temperatures as a function of boron dopant concentration. Distinct from bulk powder characterization, electrical transport measurements of individual devices reveals multi-step transitions associated with internal defects upon dopant incorporation.

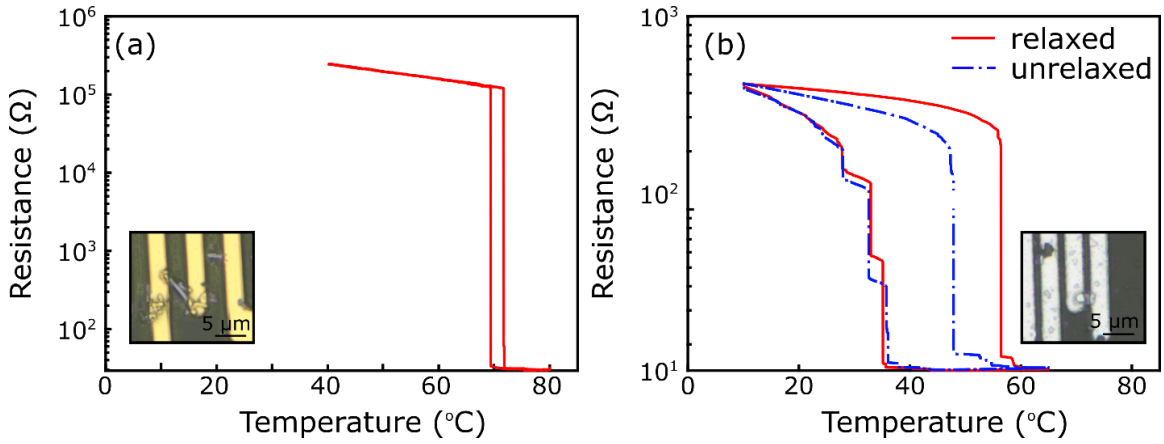

Figure 5.2. Electronic transport measurements showing resistance as a function of temperature for (a) a single cycle of an undoped VO_2 wire (inset) demonstrating an abrupt changes in resistance, as compared with (b) cycles for a $B_{0.02}VO_2$ device which demonstrates multi-step transitions with a much larger ΔT. This hysteresis can be modulated by relaxation time; the first 'relaxed' cycle (red) of the device ramped between 10 °C and 65 °C at 5 °C/min is preceded by 21 days spent at room temperature and shows a 10 °C increase in T_h with respect to the subsequent 'unrelaxed' cycle (dashed blue) with the same thermal programming. Inset: the tested $B_{0.02}VO_2$ device.

Finally, aliovalent doping is expected to change not only M1 phase stability and MIT transition temperatures [18], but the resistivity of the M1 phase by introduction of electronic defects as well [43]. In fabricated boron doped VO_2 devices, boron inclusion lowers the electrical resistivity of the semiconducting M1 phase but does not significantly impact the resistivity of the R phase (Fig. 5.3a). The resistivity of the M1 phase at T_{ref} = 20 °C in boron doped devices (0.001

± 0.001 Ω·m) is reduced by 3-4 orders of magnitude (Fig. 5.3) as compared to the resistivity of undoped VO_2 (7.5 ± 16 Ω·m), resulting in a proportional decrease in the device resistance ON/OFF ratio to ~10 X (Fig. 5.3). At the relatively high concentrations of dopants examined in this study (0.5 – 2.0 at. %), the dependence of the resistivity of the M1 phase on boron dopant concentration seems to have saturated, although dopant concentrations are still below the approximately >8% at which breakdown of electron-correlation effects are expected to return the M1 phase to the metallic conduction [44]. In contrast, the resistivity of the R phase is not significantly changed with the exception of the devices fabricated from the $B_{0.01}VO_2$ sample. Resistivity in these samples was anomalously high when compared with the R phase resistivity of other doped sample sets (Fig. 5.3), indicating another source of scattering sites perhaps related to extended defects created during synthesis or doping thermal treatments. The presence of extended defects is supported by the increased number of transition steps in this sample set as compared to other boron doped sample sets.

Additionally, the temperature coefficient of resistance (*TCR*) shows strong scaling with B-dopant concentration ($TCR = -0.0002M_s - 0.0011$, $R^2 = 0.30$). Here, *TCR* was calculated from the equation,

$$TCR = \frac{1}{R_0}\frac{dR}{dT}$$

with *dR/dT* fit from the linear portion of the heating trace between 20 °C and 30 °C, and with R_o representing the resistance at the reference temperature 20 °C. In both undoped and B-doped devices, *TCR* is negative and demonstrates semiconducting behavior as expected for the M1 phase (Fig. 5.3). As boron dopant addition increases (correlated to the decrease in Martensite start (M_s) temperature) *TCR* increases (becomes less negative), which is again consistent with an increased

number of extrinsic charge carriers. Therefore, although the overall resistivity of the M1 phase is reduced due to B-dopant inclusion, |*TCR*| is decreased as the B-dopant concentration increases.

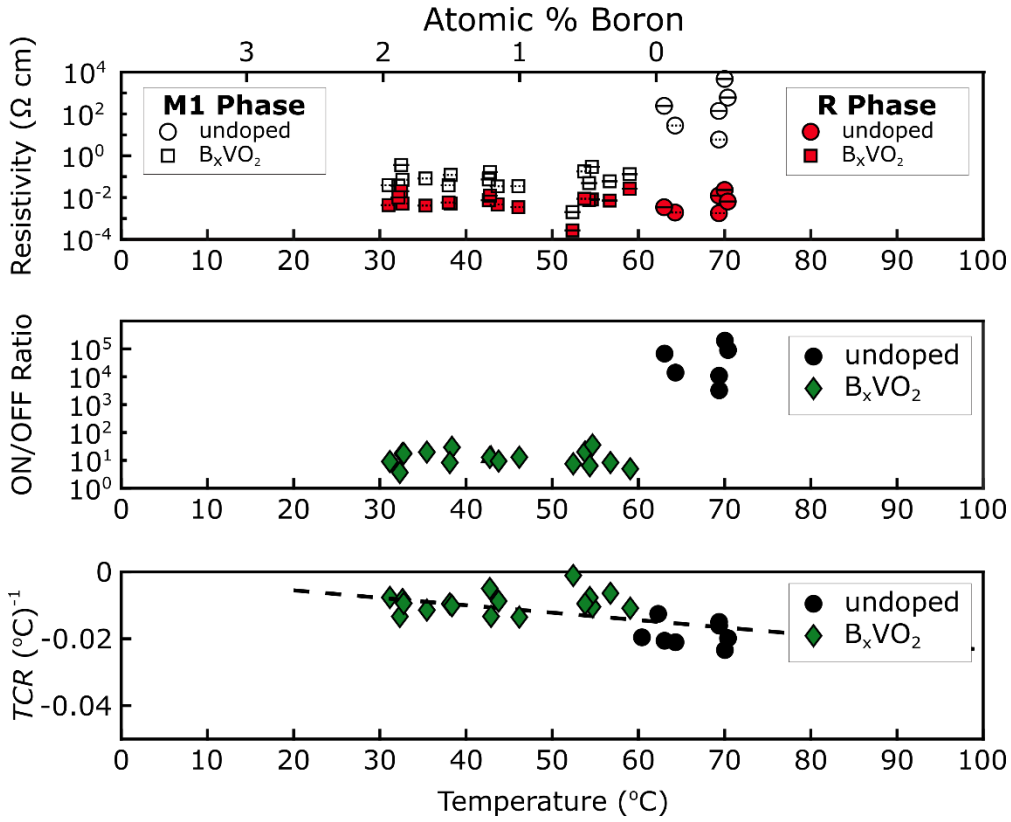

Figure 5.3. (Top) Resistivity of monoclinic VO_2 (white) and tetragonal VO_2 (red) as a function of the M_s temperature for both undoped (circles) and B-doped samples (squares). The top axis, atomic % B is inferred from the relation (M_s = -15.5[B] + 62) [25]. Error bars are denoted with a solid line and are derived from uncertainty (1σ) on device dimensions obtained by atomic force microscopy measurements. Error denoted with a black dashed line are obtained from error of optical microscopy measurements of length and width, with particle height estimated from mean device height. (Middle) The ON/OFF ratio for both doped and B-doped samples is calculated by the resistance in the M1 phase at 20 °C divided by the resistance in the R phase at 80 °C. (Bottom) *TCR* of the M1 phase (T_{ref} = 20 °C) shows a linear trend with M_s temperature or boron dopant concentration (R^2 = 0.31).

5.3.3 Current driven phase transition in B-doped devices

In order to enable device functionality, the phase transition was driven by application of electric current induced joule-heating in boron doped devices. M1 to R transitions only were studied in this method by holding the temperature of the device at a set-point below the R to M1 transition temperature, so that the cooling transition occurred immediately upon removal of the current source i.e. in a volatile switching scheme. As current is swept upwards, resistance of the device decreases smoothly, consistent with induced self-heating, until discontinuously dropping to a lower resistance state, indicating the monoclinic to tetragonal phase transition. Here, current at which the maximum change in resistance per change in current (dR/dI) occurs is extracted as the critical switching current, I_{crit}. Variability in I_{crit} over the course of 10 cycles is relatively low (σ = 22 uA; Fig. D-2b). Switching occurs at increasing values from ~ 400 μA to 1 mA depending linearly on the base temperature of the device (I_{crit}= -0.0087·T + 0.86, R^2 = 0.91; Fig. 5.4), demonstrating that as the base temperature is lowered a higher degree of joule heating is required to raise the temperature of the device above T_h. The temperature dependence of the voltage required to drive the phase transition explored in W_xVO_{1-x} nanowires was found to be non-linear, with an exponential dependence on heating and a square root dependence on cooling [23]. Although joule heating depends on dissipated power of an applied square pulse ($P = I^2R$), calculation of temperature increases inside the device are complicated by convection losses in the testing stage (open to lab air) as well as by non-trivial heat transport through the device. Therefore, some deviation from previously observed trends is not unexpected. In comparison with thermally driven switching of the same device, the resistance values at a given base temperature in the M1 phase are slightly lower, perhaps due to device degradation after repeated cycling (Fig. D-2a). However, the two-step nature of the transition observed during thermal cycling is also observed

during the current-induced transition (Fig. 5.4a). Thus, because the current driven cycle recreates the features of the thermally driven cycles, I_{crit} scales with base temperature, and because the device returns to the tetragonal phase upon removal of the current source we can attribute current driven switching exclusively to the metal-insulator transition instead of any sort of filament driven switching observed in other metal oxides (NiO, HfO_2, CuO) at high electric fields [45].

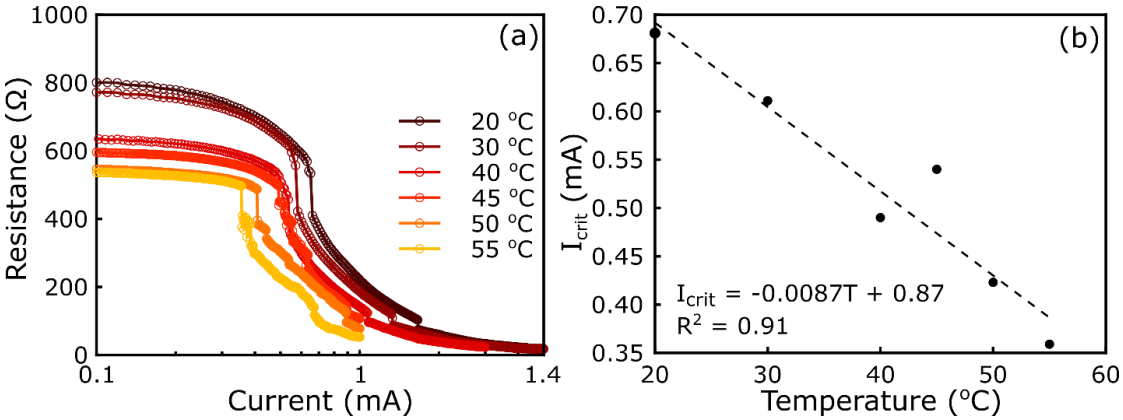

Figure 5.4. Current-driven heating transitions in (a) a single $B_{0.01}VO_2$ device held at incremented base temperatures with current swept between (0 – 3 mA). (b) Extracted switching current shows a linear dependence on base temperature of the device (R^2 = 0.91).

To test kinetic relaxation in current driven transitions, a series of isothermal experiments were designed in which the device was held at a base temperature on a temperature stage or in a water bath and allowed to "relax" for an incremented amount of time between current driven switching cycles. In a single more highly doped device (B at. % ~ 2.0), which demonstrates an increase in T_h as a function of hold time and temperature during thermally driven experiments, an increase in I_{crit} as a quasi-exponential function of time for a given temperature is observed (Fig. 5.5b). While differences in I_{crit} with relaxation times between 1 – 1,000 s may not be significant

for a given base temperature, the differences in I_{crit} between 1 s and longer time scales (15 hours) at 20 ^{o}C= demonstrate an approximately 100 µA increase in I_{crit}. Further collection of data points from relaxation holds on longer time scales (t = 3 days to t = 15 days) is required to further elucidate the trend at other temperatures. Several tested devices do not show any systematic trend with I_{crit} and relaxation time, perhaps as a result of low boron dopant concentration producing a heating transition temperature relatively close to the fully relaxed transition temperature (i.e. 57 ^{o}C vs 60 ^{o}C). Differences in transition temperature of this magnitude would relate to relatively small differences in $I_{crit,}$ that might fall below the level of significant difference. Therefore, a minimum concentration of boron dopants likely exists in order to alter I_{crit} as a function of relaxation time in order to add functionality to resistance switching devices based on B-doped VO_2. However, further investigation of larger numbers of devices is required to fully map the kinetic relaxation and determine the relaxation rate as a function of boron concentration, as well as the variability and repeatability of this effect.

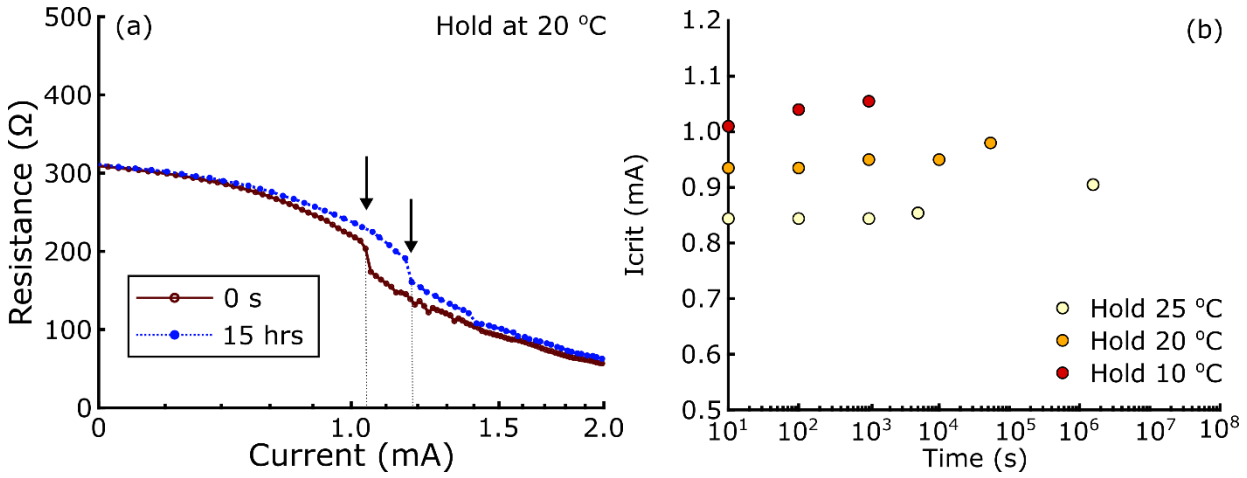

Figure 5.5. (a) Resistance as a function of current traces for $B_{0.02}VO_2$ device relaxed at 20 °C for a period of 0 s (red solid line) or 15 hrs (blue dashed line). (b) Extracted I_{crit} versus relaxation time for three hold temperatures with exponentially increasing relaxation times from the same device.

5.3.4 Internal Loops

A distinct advantage of electronic transport measurements are their extreme sensitivity to local atomic order. In all cases of electronic transport measurements of B-doped devices, open transformation loops were observed as a result of mismatch of the M1 resistivity and *TCR* between cooling and heating operations, especially in the 15 °C – 20 °C regions (Fig. 5.6a). To test the origin of this mismatch, smaller temperature loops (15 cycles) were tested ramping between 15 °C and 25 °C at 5 °C/min after completion of the first "relaxed" transformation cycle. Over a period of one hour, an increase in resistance measured at 15 °C, as well as decrease in TCR is observed as the number of smaller temperature loops progresses. The evolution of the M1 resistivity and *TCR* is indicative of the evolution of local atomic environments that could alter electronic carrier density or mobility. Moreover, the evolution of resistivity within these smaller temperature loops is gradual and does not show any sharp discontinuities. Here, we interpret these gradual changes

in resistivity in light of the short range diffusion of boron atoms from metastable to stable coordination sites. As time progresses, the relative populations of boron occupying these sites is altered at a constant rate, so that resistivity increases toward the outer envelope value of the first "fully relaxed" cycle. Moreover, subsequent internal loops heating between 15 ^{o}C and 40 ^{o}C at 5 ^{o}C/min demonstrate an additional modulation of M1 resistivity related to the M1 to R phase transition. Upon ramping between 15 ^{o}C and 40 ^{o}C, a 4 Ω decrease in resistance upon returning to 15 ^{o}C was observed (Fig. 5.6b), after which resistance measured at 15 ^{o}C began to steadily increase as function of time. Because the metal insulator transition in boron doped devices occurs over a series of steps, phase coexistence within the intermediate temperature loops is possible. Upon ramping to 40 ^{o}C, it is possible either than a small volume has transformed back to the R phase, resetting the boron dopant site populations, or that a phase boundary has moved back and forth, with the same effect on B site populations. Therefore, electrical transport experiments demonstrate the two major routes toward resistance modulation in the boron doped VO_2 system, (1) the phase transition accompanied by mesoscopic domain formation, and (2) the local rearrangement of boron dopant configurations in the lattice.

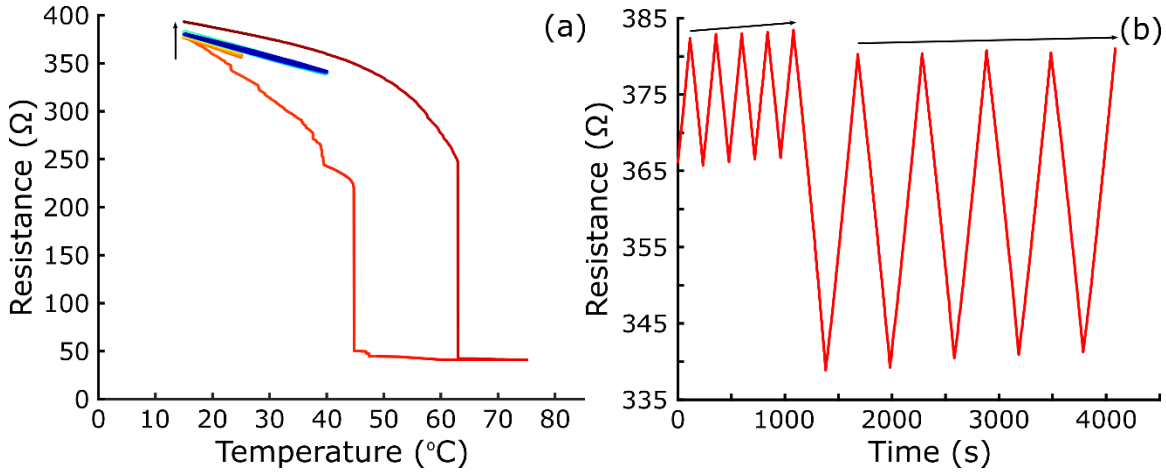

Figure 5.6. (a) Transformation loop of a single device from a "fully relaxed" state, followed by 15 cycles of internal loops from 15 ºC to 25 ºC at 5 ºC/min, and 5 cycles of internal loops between 15 oC and 40 oC at 5 oC/min. Color of the line is scaled with time transitioning from red, to yellow, to blue. (b) Resistance as a function of time for 5 cycles of internal loops between 15 ºC to 25 ºC at 5 ºC/min and 5 cycles of internal loops between 15 ºC and 40 ºC at 5 ºC/min.

5.3.5 Device Level Implications

The introduction of a time dependent modulation of resistance via boron dopant diffusive relaxation may permit a higher fidelity mimicry of the short term and long term plasticity inherent in biological synaptic dynamics. In the biological counterpart, the transmission of a neuron spiking signal is weighted by its passage through the synapse. Within the plasma of a synaptic cell, the accumulation of Ca^{2+} and decay over time of this concentration (by enzyme mediated migration) is responsible for modulation of this weighting function [29]. So while the non-volatile two state operation of memristors has been able to replicate the basic functionality of a biological synapse optimized for memory, the plasticity of the synapse remains unaddressed. The critical feature of this behavior is the ability to increase or decrease the resistance of the device as a function of pulse frequency i.e. state plasticity. More recently, Ta_2O_{5-x} "second-order memristors" in which pulse frequency controls internal temperature and oxygen vacancy diffusion rates have been

demonstrated [27]. Additionally, HfO_x:Ag devices demonstrate plasticity by the field assisted formation of Ag conductive filaments (low resistance) and surface energy minimization driven diffusional formation of Ag nanoclusters (high resistance) [28]. In contrast, the volatile nature of undoped VO_2's resistance switching behavior (associated with the low hysteresis of the MIT) has confined application of VO_2 based devices to integration as the "selector" in neuromorphic architectures [46]. However, the incorporation of the time access and wide hysteresis introduced by interstitial boron doping is a promising avenue for the extension of VO_2's applications in neuromorphic computing. Here, boron dopant diffusion is analogous to the time dependent decay of Ca^{2+}, increasing the resistance/weight of the synapse (device) as a function of time so that additional information might be encoded as a function of pulse frequency. Presently, the thermal relaxation times observed here (hours) are much longer than the times scales (ns) needed for this (or any) application. A logical extension of this "proof-of-concept" would then involve the demonstration of shortened boron diffusion dynamics driven by current pulses rather than isothermal holds.

5.4 Conclusions

In conclusion, we have demonstrated that boron doping of VO_2 introduces diffusive dynamics into the resistance switching behavior of current driven devices. The changes in resistance and I_{crit} as a function of relaxation time are shown to exclusively derive from boron dopant addition, as changes in critical switching current are commensurate with the increase in M1 to R transition temperature in thermally cycled boron doped devices. Investigation of changes in I_{crit} as a function of B dopant concentration are planned in order to demonstrate large, useful changes in critical switching parameters. Furthermore, because relaxation rates are slow

(noticeable shifts in T_h or I_{crit} are observed only after several hours), further exploration of current driven relaxation is suggested in order to understand whether boron diffusion can be coupled with applied electric field. Dependent on these results, frequency and pulse amplitude studies might be used to determine whether realistic plasticity enabled memristive behavior can be achieved in this system.

5.5 References

[1] Ladd L A and Paul W 1969 Optical and transport properties of high quality crystals of V2O4 near the metallic transition temperature *Solid State Communications* **7** 425-8

[2] Morin F 1959 Oxides which show a metal-to-insulator transition at the Neel temperature *Physical review letters* **3** 34

[3] Pickett M D and Williams R S 2012 Sub-100 fJ and sub-nanosecond thermally driven threshold switching in niobium oxide crosspoint nanodevices *Nanotechnology* **23** 215202

[4] Pickett M D, Medeiros-Ribeiro G and Williams R S 2013 A scalable neuristor built with Mott memristors *Nature materials* **12** 114-7

[5] Kumar S, Strachan J P and Williams R S 2017 Chaotic dynamics in nanoscale NbO 2 Mott memristors for analogue computing *Nature* **548** 318

[6] Seta K and Naito K 1982 Calorimetric study of the phase transition in NbO2 *The Journal of Chemical Thermodynamics* **14** 921-35

[7] Cavalleri A, Dekorsy T, Chong H H, Kieffer J-C and Schoenlein R W 2004 Evidence for a structurally-driven insulator-to-metal transition in VO 2: A view from the ultrafast timescale *Physical Review B* **70** 161102

[8] Li W, Yu Q, Liang J, Jiang K, Hu Z, Liu J, Chen H and Chu J 2011 Intrinsic evolutions of optical functions, band gap, and higher-energy electronic transitions in VO2 film near the metal-insulator transition region *Applied Physics Letters* **99** 241903

[9] Cao J, Gu Y, Fan W, Chen L-Q, Ogletree D, Chen K, Tamura N, Kunz M, Barrett C and Seidel J 2010 Extended mapping and exploration of the vanadium dioxide stress-temperature phase diagram *Nano Letters* **10** 2667-73

[10] Wu J, Gu Q, Guiton B S, de Leon N P, Ouyang L and Park H 2006 Strain-induced self organization of metal− insulator domains in single-crystalline VO2 nanobeams *Nano letters* **6** 2313-7

[11] Kumar S, Pickett M D, Strachan J P, Gibson G, Nishi Y and Williams R S 2013 Local Temperature Redistribution and Structural Transition During Joule-Heating-Driven Conductance Switching in VO2 *Advanced Materials* **25** 6128-32

[12] Stefanovich G, Pergament A and Stefanovich D 2000 Electrical switching and Mott transition in VO2 *Journal of Physics: Condensed Matter* **12** 8837

[13] Gopalakrishnan G, Ruzmetov D and Ramanathan S 2009 On the triggering mechanism for the metal–insulator transition in thin film VO2 devices: electric field versus thermal effects *Journal of Materials Science* **44** 5345-53

[14] Wu B, Zimmers A, Aubin H, Ghosh R, Liu Y and Lopez R 2011 Electric-field-driven phase transition in vanadium dioxide *Physical Review B* **84** 241410

[15] Booth J M and Casey P S 2009 Anisotropic structure deformation in the VO 2 metal-insulator transition *Physical review letters* **103** 086402

[16] Braham E J, Sellers D, Emmons E, Villarreal R, Asayesh-Ardakani H, Fleer N A, Farley K E, Shahbazian-Yassar R, Arròyave R and Shamberger P J 2017 Modulating the Hysteresis of an Electronic Transition: Launching Alternative Transformation Pathways in the Metal—Insulator Transition of Vanadium (IV) Oxide *Chemistry of Materials*

[17] Kittiwatanakul S, Sauber N, Cyberey M, Lichtenberger A, Weikle R and Lu J 2018 Tuning of temperature coefficient of resistivity in poly-crystalline VO 2 via chemical doping(vol 10656): International Society for Optics and Photonics) p 106560A

[18] Pouget J and Launois H 1976 Metal-insulator phase transition in VO2 *Le Journal de Physique Colloques* **37** C4-49-C4-57

[19] Strelcov E, Tselev A, Ivanov I, Budai J D, Zhang J, Tischler J Z, Kravchenko I, Kalinin S V and Kolmakov A 2012 Doping-based stabilization of the M2 phase in free-standing VO2 nanostructures at room temperature *Nano letters* **12** 6198-205

[20] Huang K, Meng Y, Xu X, Chen P, Lu A, Li H, Wu B, Wang C and Chen X 2017 Orbital electronic occupation effect on metal–insulator transition in Ti x V1− x O2 *Journal of Physics: Condensed Matter* **29** 355402

[21] Hu Y, Shi Q, Huang W, Zhu H, Yue F, Xiao Y, Liang S and Lu T 2016 Preparation and phase transition properties of Ti-doped VO 2 films by sol–gel process *Journal of Sol-Gel Science and Technology* **78** 19-25

[22] Asayesh-Ardakani H, Yao W, Nie A, Marley P M, Braham E, Klie R F, Banerjee S and Shahbazian-Yassar R 2017 Direct evidence of M2 phase during the monoclinic-tetragonal (rutile) phase transition of W-doped VO2 nanowires *Applied Physics Letters* **110** 053107

[23] Wu T-L, Whittaker L, Banerjee S and Sambandamurthy G 2011 Temperature and voltage driven tunable metal-insulator transition in individual W x V 1− x O 2 nanowires *Physical Review B* **83** 073101

[24] Lee S, Cheng C, Guo H, Hippalgaonkar K, Wang K, Suh J, Liu K and Wu J 2013 Axially engineered metal–insulator phase transition by graded doping VO2 nanowires *Journal of the American Chemical Society* **135** 4850-5

[25] Alivio T E, Sellers D G, Asayesh-Ardakani H, Braham E J, Horrocks G A, Pelcher K E, Villareal R, Zuin L, Shamberger P J and Arróyave R 2017 Postsynthetic Route for

Modifying the Metal ▪ Insulator Transition of VO2 by Interstitial Dopant Incorporation *Chemistry of Materials* **29** 5401-12

[26] Diane G. Sellers E J B, Ruben Villareal, Timothy D. Brown, Theodore E.G. Alivio, Luis R. De Jesus, Lucia Zuin, Raymundo Arroyave, Patrick J. Shamberger, Sarbajit Banerjee 2019 Dynamically Evolving Metastability in an Atomic Hourglass: Temporal Control of the Metal-Insulator Transition of VO2 upon Introduction of a Mobile Dopant

[27] Kim S, Du C, Sheridan P, Ma W, Choi S and Lu W D 2015 Experimental demonstration of a second-order memristor and its ability to biorealistically implement synaptic plasticity *Nano letters* **15** 2203-11

[28] Wang Z, Joshi S, Savel'ev S E, Jiang H, Midya R, Lin P, Hu M, Ge N, Strachan J P and Li Z 2017 Memristors with diffusive dynamics as synaptic emulators for neuromorphic computing *Nature materials* **16** 101

[29] Bi G-q and Poo M-m 1998 Synaptic modifications in cultured hippocampal neurons: dependence on spike timing, synaptic strength, and postsynaptic cell type *Journal of neuroscience* **18** 10464-72

[30] Yang J J, Strukov D B and Stewart D R 2013 Memristive devices for computing *Nature nanotechnology* **8** 13-24

[31] Alivio T E, Sellers D G, Asayesh-Ardakani H, Braham E J, Horrocks G A, Pelcher K E, Villareal R, Zuin L, Shamberger P J and Arroyave R 2017 A Post-Synthetic Route for Modifying the Metal—Insulator Transition of VO2 by Interstitial Dopant Incorporation *Chemistry of Materials*

[32] Kachi S, Kosuge K and Okinaka H 1973 Metal-insulator transition in VnO2n− 1 *Journal of Solid State Chemistry* **6** 258-70

[33] Alivio T E, Sellers D G, Asayesh-Ardakani H, Braham E J, Horrocks G A, Pelcher K E, Villareal R, Zuin L, Shamberger P J and Arroyave R 2017 A Post-Synthetic Route for Modifying the Metal—Insulator Transition of VO2 by Interstitial Dopant Incorporation *Chemistry of Materials* **29** 5401-12

[34] Cook O 1947 High-Temperature Heat Contents of V2O3, V2O4 and V2O51 *Journal of the American Chemical Society* **69** 331-3

[35] Budai J D, Hong J, Manley M E, Specht E D, Li C W, Tischler J Z, Abernathy D L, Said A H, Leu B M and Boatner L A 2014 Metallization of vanadium dioxide driven by large phonon entropy *Nature* **515** 535

[36] Berglund C and Guggenheim H 1969 Electronic Properties of V O 2 near the Semiconductor-Metal Transition *Physical Review* **185** 1022

[37] Braham E J, Sellers D, Emmons E, Villarreal R, Asayesh-Ardakani H, Fleer N A, Farley K E, Shahbazian-Yassar R, Arròyave R and Shamberger P J 2017 Modulating the Hysteresis of an Electronic Transition: Launching Alternative Transformation Pathways in the Metal–Insulator Transition of Vanadium (IV) Oxide *Chemistry of Materials* **30** 214-24

[38] Fan W, Cao J, Seidel J, Gu Y, Yim J, Barrett C, Yu K, Ji J, Ramesh R and Chen L 2011 Large kinetic asymmetry in the metal-insulator transition nucleated at localized and extended defects *Physical Review B* **83** 235102

[39] Ortin J and Planes A 1991 Thermodynamics and hysteresis behaviour of thermoelastic martensitic transformations *Le Journal de Physique IV* **1** C4-13-C4-23

[40] Clarke H, Caraway B D, Sellers D G, Braham E J, Banerjee S, Arróyave R and Shamberger P J 2018 Nucleation-controlled hysteresis in unstrained hydrothermal V O 2 particles *Physical Review Materials* **2** 103402

[41] Cao J, Ertekin E, Srinivasan V, Fan W, Huang S, Zheng H, Yim J, Khanal D, Ogletree D and Grossman J 2009 Strain engineering and one-dimensional organization of metal–insulator domains in single-crystal vanadium dioxide beams *Nature nanotechnology* **4** 732-7

[42] Braham E J, Sellers D, Emmons E, Villarreal R, Asayesh-Ardakani H, Fleer N A, Farley K E, Shahbazian-Yassar R, Arròyave R and Shamberger P J 2017 Modulating the Hysteresis of an Electronic Transition: Launching Alternative Transformation Pathways in the Metal–Insulator Transition of Vanadium (IV) Oxide *Chemistry of Materials* **30** 214-24

[43] Brückner W, Moldenhauer W, Wich H, Wolf E, Oppermann H, Gerlach U and Reichelt W 1975 The range of homogeneity of VO2 and the influence of the composition on the physical properties. II. The change of the physical properties in the range of homogeneity *physica status solidi (a)* **29** 63-70

[44] Shibuya K, Kawasaki M and Tokura Y 2010 Metal-insulator transition in epitaxial V 1− x W x O 2 (0≤ x≤ 0.33) thin films *Applied Physics Letters* **96** 022102

[45] Janod E, Tranchant J, Corraze B, Querré M, Stoliar P, Rozenberg M, Cren T, Roditchev D, Phuoc V T and Besland M P 2015 Resistive switching in Mott insulators and correlated systems *Advanced Functional Materials* **25** 6287-305

[46] Zhou Y and Ramanathan S 2015 Mott memory and neuromorphic devices *Proceedings of the IEEE* **103** 1289-310

6. CONCLUSION

6.1 Summary

This dissertation examines the role of microstructural defects and point defects on local resistance switching structures in two representative materials: HfO_2 thin films and hydrothermally synthesized VO_2 single crystals. In each material, observations as to the size and shape of metal or insulating domain and how the evolution of these domains is impacted by intentionally introduced defects is studied. The goal of these studies was to provide clarification of and possible routes of control over the mechanisms that underlie key resistance switching behaviors. Resistance switching in HfO_2 thin films is addressed in Sections 2 – 3. In Section 2, the impact of grain boundaries on resistance switching kinetics is examined and we find that introduction of grain boundaries in polycrystalline HfO_2 films creates fast ionic migration pathways which allow for lower forming voltages to drive filament formation in HfO_2 thin films without any degradation of electrical properties. Ionic migration was found to be rate-limiting in filament forming kinetics, with possible implications for the shape of the conductive filament. In Section 3, the 3D shape of conductive filaments is explored with a developed c-AFM tomography technique. Results demonstrated that under the forming conditions commonly utilized in resistance switching literature, filament shape deviates from the exclusively inverted-cone shape predicted by the widely-adopted phenomenological model as we have observed a cone, a cylinder, and a bottom-branched filament. Joule heating is implicated as the source of filament broadening and is shown to produce increasing levels of damage to HfO_2 films as forming voltage is increased. In these cases, the role of microstructure is relegated to determining the site of filament forming, rather than the dimensions of the filaments or breakdown structures themselves.

Sections 3 and 4 primarily concern the thermal hysteresis of metal-insulator transition in undoped and boron doped VO_2, respectively. The kinetic component of thermal hysteresis in undoped VO_2 is demonstrated to be a result of a volume distributed population of potent nucleation sites (oxygen vacancy point defects) in which site potency increases as a function of undercooling or superheating (Section 3). Upon doping with boron in interstitial sites, a kinetic asymmetry is introduced into cooling and heating transition temperatures, with T_h (and thermal hysteresis) changing as a function of relaxation time in the M1 phase while T_c is invariant. This relaxation is associated with short-range B interstitial diffusion between metastable and stable interstitial lattice sites [1]. Section 4 examines the application of this kinetic relaxation in current driven two terminal B_xVO_2 devices. Electrical transport measurements show that current driven switching mirrors thermally driven switching in these devices, and that the critical switching current can be modulated as a function of relaxation time. As expected, B dopants also introduce several transitions steps associated with interface pinning or heterogeneous strain gradients, as well as a lowered resistivity of the M1 phase consistent with extrinsic semiconductor doping. A few extensions of the work presented in this thesis in each material are described below.

6.2 Outlook

6.2.1 Conductive Filaments in HfO_2 Resistance Switches

6.2.1.1 Minimization of Structural Deformation accompanying Filament Forming

We have shown that conductive filament formation in HfO_2 based devices is accompanied by significant disruption of the oxide layer and copper top electrode under typical forming bias conditions (Section 3). In this study, uncontrolled thermal gradients were largely responsible for the extent of disruption observed, and need to be mitigated in order to examine the impact of other.

In order to minimize thermal pulses upon forming, the following are suggested: (1) proper integration of current overshoot by fabrication of a transistor structure in-line with the device, (2) adoption of thick, thermally conductive bottom and top electrodes with the metal layer as well as incorporation of lateral heat sinks in scaled devices, (3) use of polycrystalline microstructure (as demonstrated in Section 2) to minimize applied forming and switching voltages.

6.2.1.2 Impact of Microstructure on Filament shape in Low Voltage Limits

Once the above steps are taken, it may be possible to isolate the effect of oxide microstructure on filament shape from thermal broadening considerations. Section 2 demonstrated that oxide microstructure determines vertical ion migration rates during initial filament forming, and the extent to which microstructure controls final filament shape is still an open question. It may also be the case that after the initial forming event the local oxide surrounding the conductive filament is irreversibly altered in composition and structure, so that no lasting effects of the oxide microstructure have any bearing on the variability of subsequent switching cycles. In order to answer this question, the c-AFM tomography technique could be a applied to conductive filaments formed in devices under equivalent forming bias and compliance current, but in either an amorphous or polycrystalline oxide layer.

6.2.2 Metal Insulator Transition in VO_2

6.2.2.1 Diffusive Dynamics in VO_2 Based Memristors

Scaling of ΔI_{crit} with boron dopant concentration:

The extent of T_h and consequently I_{crit} modulation by relaxation time observed in Section 5 was relatively low (< 10 ^oC and < 150 µA respectively) in comparison to bulk powder studies, which suggest that an up to 40 ^oC modulation can be achieved at 5.2 at. % B [1]. Ultimately, the ΔI_{crit} observed as a function of relaxation time is a function of T_h*-T_h, where T_h* is the unrelaxed

heating transition temperature. Moreover, because T_h* is very nearly constant with boron concentration while T_h shows a linear dependence on boron concentration, the quantity T_h*-T_h is expected to increase as a function of boron concentration. Therefore, it is likely that for a given relaxation time in more highly doped VO_2 devices, the ΔI_{crit} achieved as a function of relaxation time would be larger. Furthermore, extended mapping of I_{crit} dependence on relaxation time and relaxation temperature is an ongoing effort that might aid in examination of boron dopant diffusion activation energy barriers. Already, some fitting of kinetic data from DSC cycling of bulk B_xVO_2 powders has been attempted with a single activation energy [Sellers et al, in prep], the results of which reveal a quasi-exponential function. Although a few boron dopant migration pathways have been explored using DFT and NEB (Villareal et al, in prep), it is likely that several relaxation pathways are accessed in the material, leading to a distribution of activation barriers. With additional kinetic data obtained more rapidly in current driven devices, a more sophisticated model involving a distribution of activation energies might be attempted.

Current Driven Relaxation:

Furthermore, thermal relaxation in boron doped devices occurs over a period of several hours rather than the ms time scales of biological synapse function [2], or ns switching times generally desirable in device operation. However, boron dopant diffusivities might also be coupled to the applied electric field (~1 kV/cm) so that even at the relatively low local temperatures induced by joule-heating, boron atoms could then be expected to migrate the less than one unit cell distance needed to populate another interstitial site at a faster rate. Here, application of an average electric field across the VO_2 particle might alter the slope of the potential energy wells of adjacent boron interstitial sites, therefore lowering the effective activation energy barrier and increasing the diffusivity. Moreover, XANES characterization has demonstrated that the covalency of the lattice

is reduced upon boron dopant inclusion, so that the anion lattice might be polarized by the local electric field, and the activation energy for diffusion reduced. While extrinsic dopants are usually considered immobile, Li diffusivity has been extensively studied in Si and Ge at a relatively low temperature range (25 – 125 ^{o}C) and electric fields [3, 4], with the observation that dopant profiles are established during electric field application and do not decay upon removal of the field i.e. thermal diffusivity is much lower[5]. Therefore, testing of current driven relaxation (which creates an electric field across the device) at constant pulse amplitude with the number of pulses varied is proposed. Evidence of electric field enhanced boron dopant relaxation would be obtained from an increase in I_{crit} as a function of increasing pulse amplitude, duration, and or number increase.

Finally, other mobile dopants with a small ionic radius (including Li) could show similar diffusive behaviors as boron, albeit with different diffusivities and overall impact on thermal equilibria. For example, at high boron dopant concentrations, transition temperatures are depressed far below practical device operation temperatures to below room temperature. It is conceivable that co-doping with another element might allow for diffusive boron dynamics to effect thermal hysteresis, while changes in phase stability are predominantly controlled by the other dopant species which raise the MIT temperature (e.g. Ti) [6].

6.2.2.2 Observations of Phase Boundary Motion and Phase Coexistence in Doped VO_2

Chemical control of the coupled electronic-structural transformation in correlated oxide systems is a vigorously investigated area, due to fundamental interest in the role chemical dopants play in stabilizing different crystal structures and altering electronic band structure, as well as practical interest in being able to tune the critical transformation temperature and the degree of volatility of the transformation [7]. While chemical doping has shown dramatic effects in changing the thermodynamic stability of different doped VO_2 phases, including increasing or depressing

phase transformations by up to ~20 ºC [8], and stabilizing phases that are not typically observed in undoped VO_2 upon simple heating and cooling [9, 10], very little is known regarding the impact of chemical doping on transformation mechanisms in this system. Doping could potentially modify the behavior of the electronic-structural phase transformation by at least three mechanisms: 1) by altering the energy landscape of the system, including the magnitude of energy barriers limiting forward and reverse transformation, 2) by stabilizing intermediate phases, which may introduce alternative transformation paths, or 3) by introducing localized regions of strain surrounding chemical dopants, which could affect local thermodynamic equilibria heterogeneously throughout a sample. Importantly, all three of these effects could potentially impact either the energy barriers limiting incipient nucleation of a new daughter phase within a parent phase, or the mobility of heterophase boundaries, impacting the rate of growth of domains of a daughter phase. However, local strain heterogeneity as well as the introduction of point defects could pin propagating boundaries. Clarifying changes in phase transformation mechanisms requires microscopic investigation of domain nucleation and growth in both undoped and doped systems. Resolving these questions can expose important underlying clues in understanding transformation mechanisms in both undoped and chemically doped systems, and can reveal new approaches to engineering metal-insulator transitions with desired transformation behavior.

Initial optical microscopy observations of transitions in $W_xV_{1-x}O_2$ have been made following the protocols developed in Section 4. In contrast to phase transformations in undoped VO_2, transformations in W-doped VO_2 show two distinct characteristics: 1) a gradual transformation over multiple temperature intervals, with clearly defined abrupt transitions in only a fraction of the particles imaged, and 2) a uniform transformation throughout a particle, with no domains that are distinguishable on the length scale of optical observations in most particles. The

exact start and finish temperatures (T_s, T_f) are difficult to clearly define due to the gradational nature of the transformation, however transformation loops for individual particles were able to be extracted from summed pixel values within a predefined area outlining only the considered particle (Fig. 6.1). Assuming that red intensity properly estimates transformed phase fraction, T_c is considered the temperature corresponding to the half-way point of normalized red intensity value. $T_{s.}$ and T_f are then defined as the temperatures at which the transformation fraction increases 25% and 75% respectively above the mean baseline. While optical observations are unable to discern clear domains of low temperature (M1) and high temperature (R) phases, the gradational nature of the transition is consistent with phase coexistence at sub-micron length scales, smaller than discernable by optical microscopy. This claim is supported by high-resolution TEM observations of W-doped hydrothermal VO_2 particles which illustrate phase coexistence on length scales < 10 nm [9]. Furthermore, TEM observations suggest existence of the M2 phase at the interface between M1 and R phases, which is also not observable at optical length scales [9].

Interestingly, there is a distinguishable asymmetry between heating and cooling cycles in the transition width ($T_f - T_s$) for a large proportion of sampled particles. In these cases, the heating transition width is large ($T_w > 5\ ^oC$) indicating a very gradual phase transition (Fig. 6.1 a-b), while the corresponding cooling transition is sharp ($T_w < 5\ ^0$ C, Fig. 6.1 c-d). While this asymmetric relation is observed for over half of the particle sampled, the other particles show a range of symmetric behaviors including sharp transitions both on heating and cooling as well as gradual transitions during both heating and cooling. The width (T_w) of the heating or cooling transition does not seem to be correlated with T_c, which scales linearly with doping concentration in bulk samples. Such a correlation would suggest that increased doping concentration leads to a large temperature range of phase coexistence, either by increasing the local strain surrounding individual

W atoms, or by impeding the motion of a phase interface until sufficient thermal energy is gained, and the phase front propagates rapidly across the untransformed volume once more. With the current optical microscopy observations, distinguishing between the two scenarios is impossible.

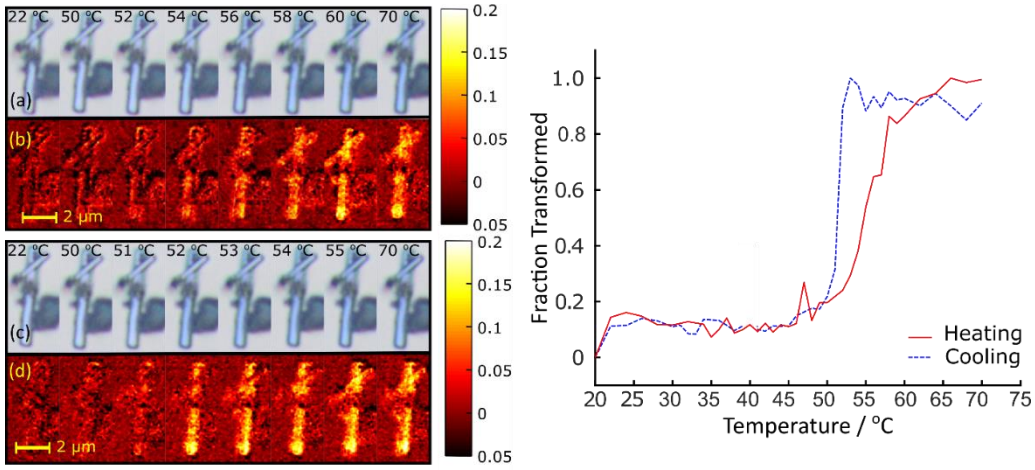

Figure 6.1 (a) Heating images of a selected $W_xV_{1-x}O_2$ particle at 2 °C increments under unpolarized reflected white light showing a gradual transition and (b) difference plots from red portion of image pixels on heating. (c) Cooling images of the same particle 1 °C showing a sharp transition and (d) associated difference plots from red portion of image pixels on cooling. Difference plots were created by extracting normalized red pixel values, and calculating the difference between a low temperature "base-line" image (20 ^{o}C) and the high temperature image at each pixel. These values are then extracted to calculate the (e) cumulative fraction transformed as a function of temperature at 1 ^{o}C increments on heating (red line) and cooling (blue dashed line).

However, distinguishing between the two scenarios might be accomplished by imaging at smaller length scales using scanning near-field optical microscopy (s-SNOM; Fig. 6.2), and is important by virtue of the solution taken to eliminate these hysteresis sources. SNOM is an atomic force microscopy based technique which has been previously used to identify M1/R domain

ordering in strained VO_2 [11]. For growth limited transformations, observations of phase boundary evolution from a single site across the volume of the particle, with some pinning and then release of the interface could be expected. In the case of local strain gradients, appearance of domains at disconnected areas of the particle as temperature is increased/decreased might be expected. Moreover, the device fabrication techniques developed in Section 5 might be applied to $W_xV_{1-x}O_2$ particles in order to simultaneously image domain evolution and measure electrical transport. As shown previously (Section 5), electrical transport is extremely sensitive to local structure evolution both on mesoscopic and local scales, and has previously been used to distinguish between the M1 and M2 VO_2 polymorphs [12]. During ramping from low temperature to high temperature, appearance of M1, M2, and R domains (the resistivity of the M2 phase is twice that of the M1 phase) might be registered as sharp steps upwards or downwards in resistivity, but be below the observation scale visible in either SNOM or optical microscopy. Therefore, the simultaneous use of electrical transport could be used to unambiguously track the domain structure evolution over the course of the heating or cooling phase transition.

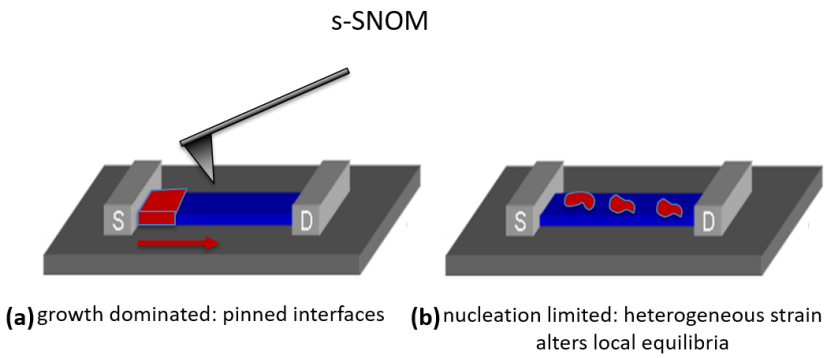

Figure 6.2 Schematic of proposed s-SNOM experiment showing possible observations that distinguish between the pinned growth of a phase front and nucleation with rapid growth in separate locations with different equilibria.

2.2.3 Nucleation Statistics in Doped VO_2 and Relationship to ΔT

Nucleation statistics describing a volume distributed population of potent nucleation sites (oxygen defects) in small volumes of VO_2 nanowires showed a particular dependence of site potency on particle volume and degree of undercooling/superheating unique to that site population (Section 4). Upon dopant introduction, it is possible that these dependencies of the potent nucleation site distribution is altered leading to an overall reduction or increase in kinetic hysteresis. Doped nanowires of VO_2 synthesized hydrothermally present the ideal case in which to exclusively study nucleation site statistics in the absence of extended defects, and below a critical volume at which elastic strain energy of the daughter phase within the parent matrix balance the chemical driving force.

Bulk studies of transitions in $W_xV_{1-x}O_2$ suggest that the kinetic portion of the hysteresis is due mainly to point defect mediated cooling transition, while the heating transition encounters a more facile nucleation pathway at the boundary of M1/M2 interfaces or M1 twin boundaries [9]. However, W doping also introduces regions of phase coexistence which complicates the origins

of the observed kinetic asymmetry. On the individual particle basis, deconvolution of the nucleation related (some distribution of M_s or A_s temperatures among individual particles) versus growth related (some distribution of T_w among individual particles) contributions to the transformed volume for a given applied temperature can be accomplished by imaging of a statistically relevant number of individual particles over the course of the phase transformation. Ensemble measurements of individual transitions could then be integrated to reproduce the overall DSC traces obtained for a given sample, and by extension, the fraction of the overall hysteresis stemming from the sluggish interface motion in a single particle or the paucity of nucleation sites within another particle.

At the bulk level, the observation that hysteresis widths measured at slow ramp rates are very similar in both undoped and W-doped particles suggests that while dopants introduce heterogeneous strain distributions within individual particles, they do not significantly alter the populations of nucleation sites within those domains. On the other hand, ensemble measurements of $W_xV_{1-x}O_2$ particles demonstrate a mean hysteresis (5 ± 3 ^oC) slightly less than the (12 ± 7 ^oC) ^oC hysteresis obtained in undoped VO_2 (Fig. 6.3a). Differences in the hysteresis of equivalent volumes between W-doped and undoped particles is also informative. The max hysteresis achieved for a single particle in undoped VO_2 is > 40 ^oC, and is < 25 ^oC in all cases for $W_xV_{1-x}O_2$, indicating subtle differences in nucleation site potencies or densities between doped and undoped particles, which could also be imagined to have a difference in driving force dependence (Fig. 6.3b).

Unfortunately, clear identification of M_s and A_s temperatures in individual particles is precluded by the sub-optical wavelength size of domains (< 10 nm) and limits development of a statistical description of nucleation in these crystals. Although T_w (the number of transition steps) does not scale with T_c in the composition range investigated (likely because the size of domains

<< size of particle), synthesis of $W_xV_{1-x}O_2$ particles in which x << 0.01 might result in low enough concentrations of W dopants such that domains on the order of the particle length can be identified and M_s/A_s temperatures clearly defined above a mean baseline. Synthesis of these samples is currently an ongoing effort.

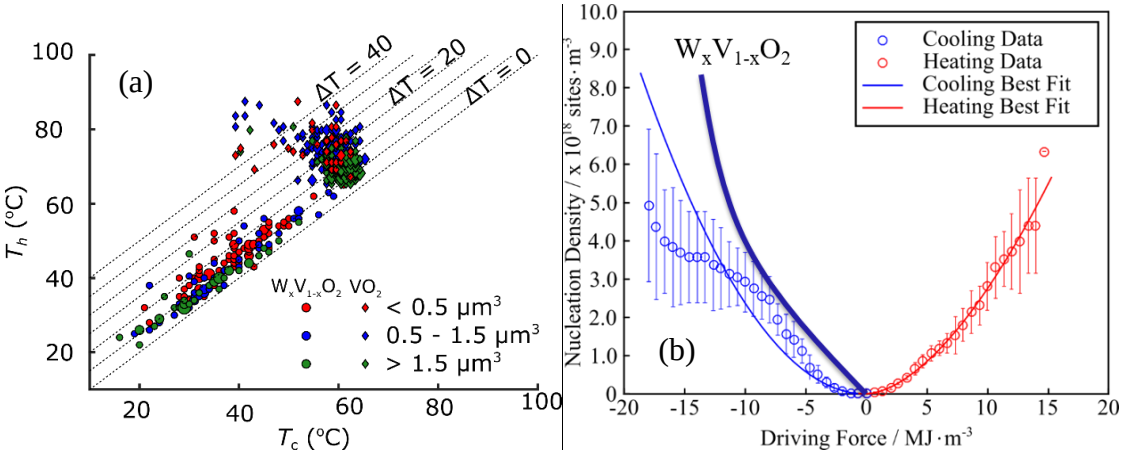

Figure 6.3. (a) Heating and cooling transition temperatures of an ensemble of $W_xV_{1-x}O_2$ particles (N = 170; circles) measured optically show a distribution in transition temperatures as result of compositional heterogeneity. Particles are binned by volume, where area of the particle is measured optically and height is estimated at an average of 800 nm. ΔT is slightly lower in doped particles, in contrast to results in undoped particles (N = 373; diamonds) which are also delineated by volume. These differences may arise from different concentrations of potent sites within particle volumes, and (b) different scalings of that potency with excess chemical driving force.

Similar observations of transformation asymmetry have also been made in individual B_xVO_2 particles by optical microscopy (Fig. 6.4). The majority of B_xVO_2 particles transition with fewer than two intermediate steps, and in these cases T_s and T_f are clearly discernible above the mean baseline. Again, some asymmetry in domain number is observed between heating and cooling transitions, with the fraction of particles showing a single step on heating (67 %) greater

than the fraction of particles showing a single step on cooling (27 %). Moreover, the impact of dopant occupation of metastable and stable interstitial sites on nucleation activation energy barriers is yet to be identified, and may be evaluated with optical particle transformation statistics.

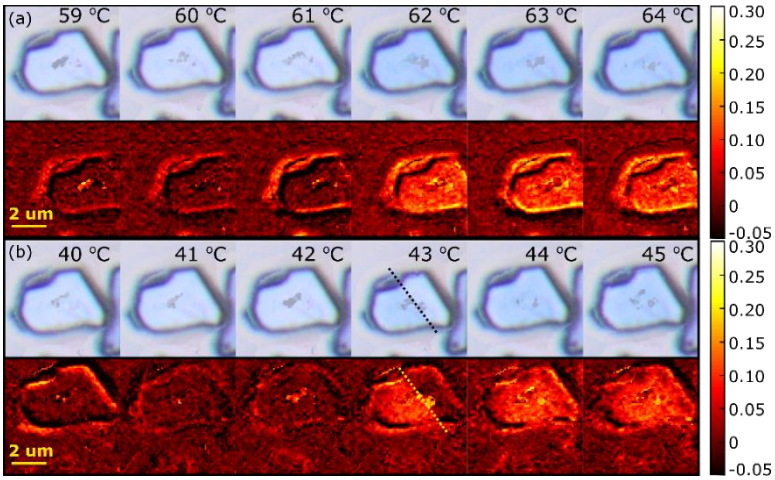

Figure 6.4 Reflected white light optical microscopy (top) and red difference images (bottom) of a selected B_xVO_2 particle during (a) the heating transition at 1 ^oC increments (b) the cooling transition at 1 ^oC increments showing sharp, in a two-step transformation. Associated red difference images are generated from the difference in the red intensity at each pixel between the image at stated temperature and image at a base temperature (58 ^oC on heating and 39 ^oC on cooling).

6.3 References

[1] Diane G. Sellers E J B, Ruben Villareal, Timothy D. Brown, Theodore E.G. Alivio, Luis R. De Jesus, Lucia Zuin, Raymundo Arroyave, Patrick J. Shamberger, Sarbajit Banerjee 2019 Dynamically Evolving Metastability in an Atomic Hourglass: Temporal Control of the Metal-Insulator Transition of VO2 upon Introduction of a Mobile Dopant

[2] Bi G-q and Poo M-m 1998 Synaptic modifications in cultured hippocampal neurons: dependence on spike timing, synaptic strength, and postsynaptic cell type *Journal of neuroscience* **18** 10464-72

[3] Pell E 1960 Diffusion rate of Li in Si at low temperatures *Physical Review* **119** 1222

[4] Cahen D and Chernyak L 1997 Dopant electromigration in semiconductors *Advanced Materials* **9** 861-76

[5] Chernyak L, Gartsman K, Cahen D and Stafsudd O M 1995 Electronic effects of ion mobility in semiconductors: Semionic behaviour of CuInSe2 *Journal of Physics and Chemistry of Solids* **56** 1165-91

[6] Huang K, Meng Y, Xu X, Chen P, Lu A, Li H, Wu B, Wang C and Chen X 2017 Orbital electronic occupation effect on metal–insulator transition in Ti x V1− x O2 *Journal of Physics: Condensed Matter* **29** 355402

[7] Zhou Y and Ramanathan S 2015 Mott memory and neuromorphic devices *Proceedings of the IEEE* **103** 1289-310

[8] Pouget J and Launois H 1976 Metal-insulator phase transition in VO2 *Le Journal de Physique Colloques* **37** C4-49-C4-57

[9] Braham E J, Sellers D, Emmons E, Villarreal R, Asayesh-Ardakani H, Fleer N A, Farley K E, Shahbazian-Yassar R, Arròyave R and Shamberger P J 2017 Modulating the

Hysteresis of an Electronic Transition: Launching Alternative Transformation Pathways in the Metal—Insulator Transition of Vanadium (IV) Oxide *Chemistry of Materials*

[10] Strelcov E, Tselev A, Ivanov I, Budai J D, Zhang J, Tischler J Z, Kravchenko I, Kalinin S V and Kolmakov A 2012 Doping-based stabilization of the M2 phase in free-standing VO2 nanostructures at room temperature *Nano letters* **12** 6198-205

[11] O'callahan B T, Jones A C, Park J H, Cobden D H, Atkin J M and Raschke M B 2015 Inhomogeneity of the ultrafast insulator-to-metal transition dynamics of VO 2 *Nature communications* **6** 6849

[12] Brückner W, Gerlach U, Moldenhauer W, Brückner H, Mattern N, Oppermann H and Wolf E 1976 Phase transitions and semiconductor-metal transition in V1− xGaxO2 Single Crystals *physica status solidi (a)* **38** 93-102

APPENDIX A

SECTION 2 SUPPLEMENTARY FIGURES

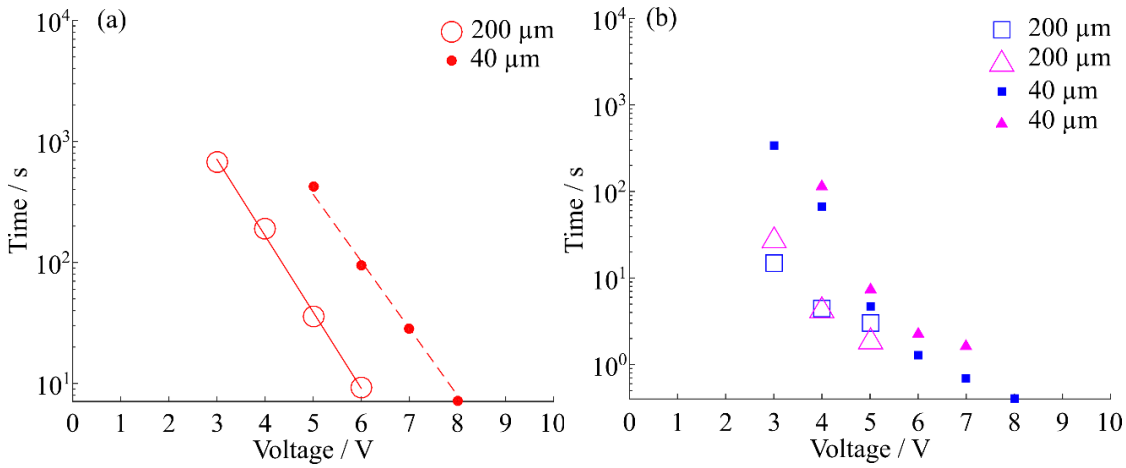

Figure A-1. Area scaling of median t_{form} as a function of constant positive applied voltage in 200 µm edge length and 40 µm edge devices for (a) amorphous TiN/HfO_2/Cu devices grown/annealed at 100 °C/400 °C, and (b) polycrystalline TiN/HfO_2/Cu devices grown/annealed at 250 °C/400 °C (blue squares) or 250 °C/600 °C (pink triangles).

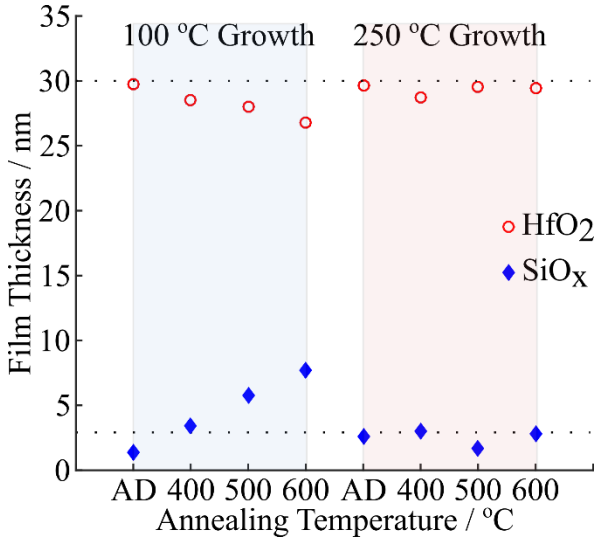

Figure A-2. Thicknesses of HfO_2 and native oxide SiO_x layers in initial set of ALD Si/SiO_x/HfO_2 films extracted from XRR analysis.

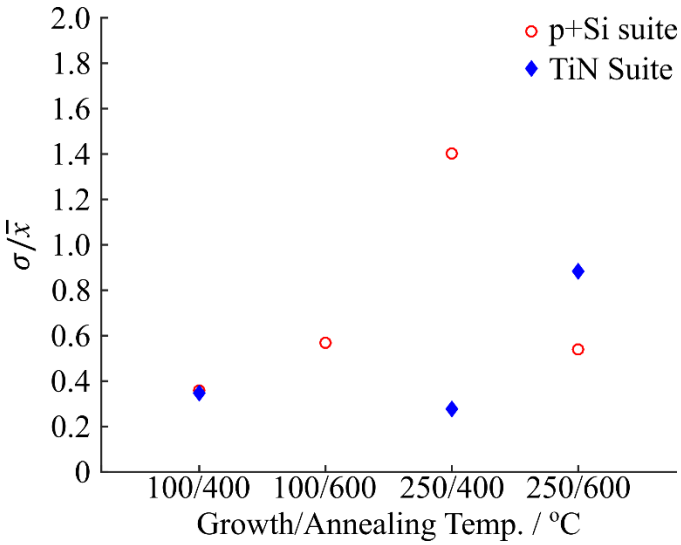

Figure A-3. (a) Relative standard deviation ($\sigma/\bar{x}$) of t_{form} data for p+ Si/HfO_2/Cu devices (red open circles) and TiN/HfO_2/Cu devices (solid blue diamonds) according to HfO_2 film growth/anneal temperature.

APPENDIX B

SECTION 3 SUPPLEMENTARY FIGURES

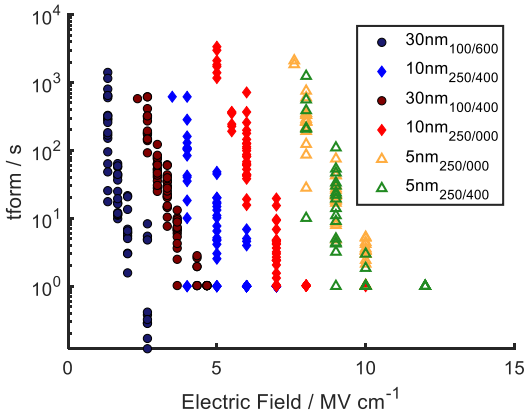

Figure B-1. Forming time as a function of electric field for Cu/HfO_2/p+Si devices with thickness of HfO_2 films designated along with deposition/annealing temperatures.

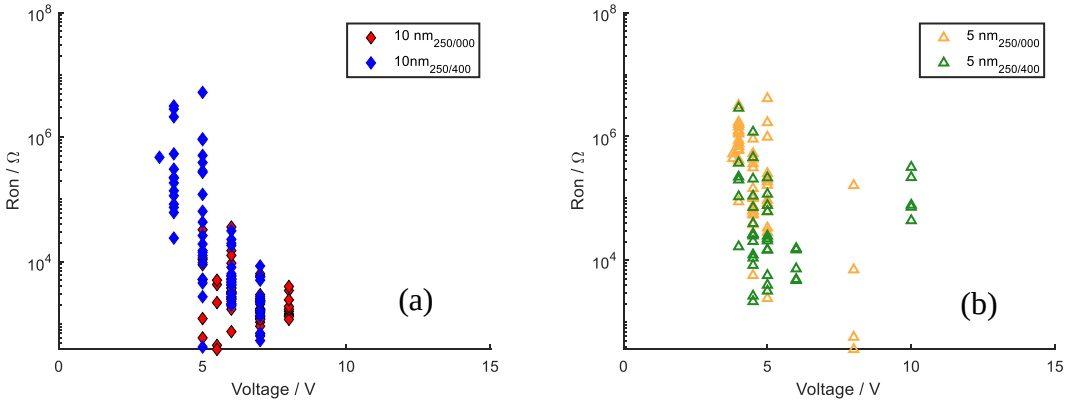

Figure B-2. On state resistance (Ron) as a function of forming voltage for (a) devices based on 10 nm HfO_2 films varied by microstructure with amorphous (250/000 ºC) films designated by red diamonds and polycrystalline films (250/400 ºC) designated by blue diamonds. The differences observed as a function of deposition/growth conditions in not observed in (b) devices based on 5 nm thick HfO_2 films with nominally amorphous films (250/000 ºC) designated by yellow triangles and polycrystalline films (250/400 ºC) designated by green triangles.

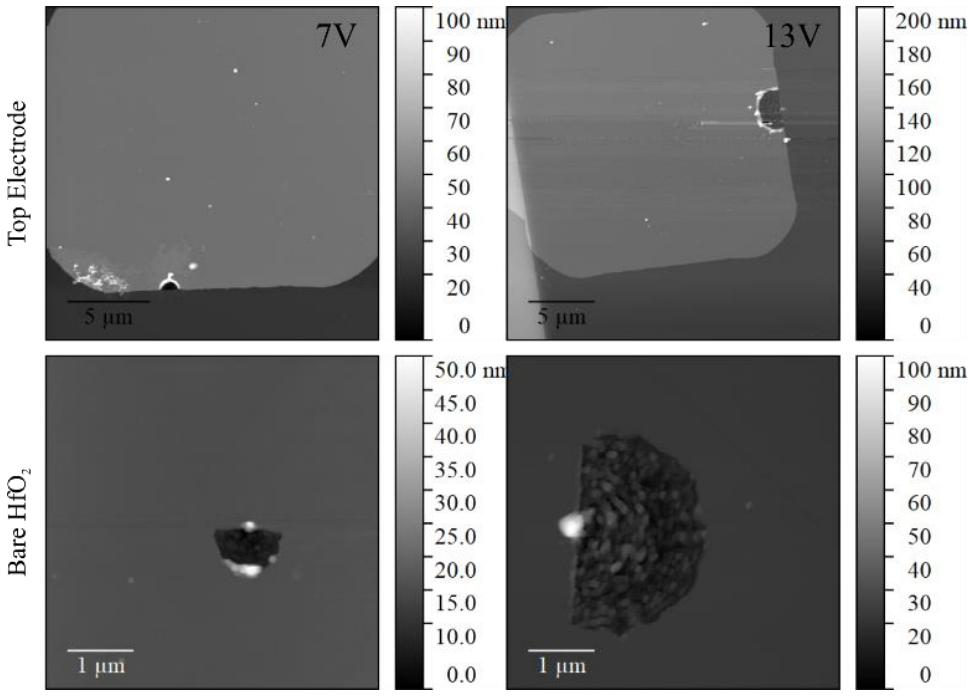

Figure B-3. AFM topographic characterization of devices based on 300 nm thick amorphous (100/400 ºC) HfO_2 with (Top) the top electrode retained as forming voltage is increased between 7 V and 13 V and (Bottom) with the top electrode removed for the same devices between 7 V and 13 V.

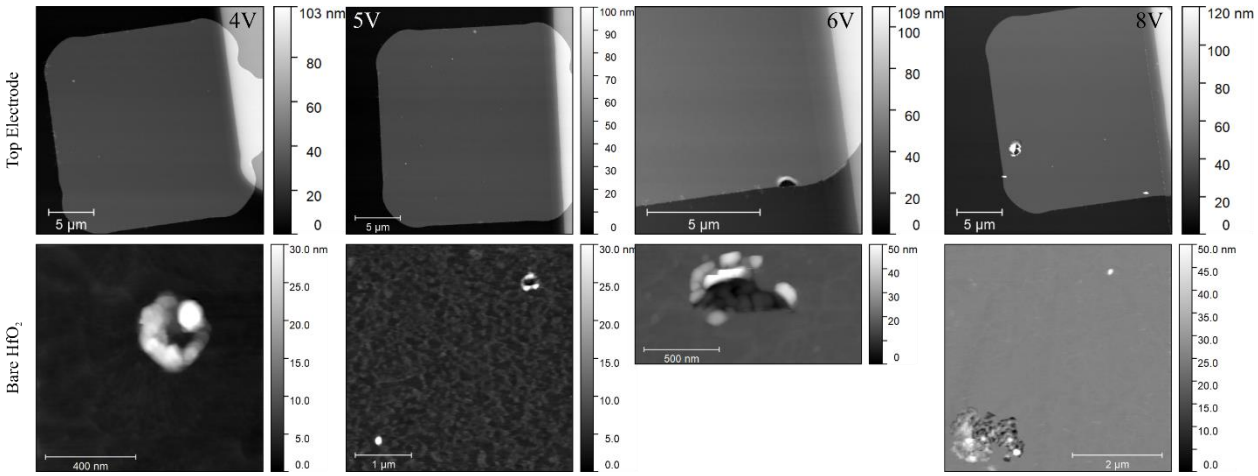

Figure B-4. AFM topographic characterization of devices based on 300 nm thick polycrystalline (100/600 ºC) HfO_2 with (Top) the top electrode retained as forming voltage is increased between 4 V and 8 V and (Bottom) with the top electrode removed for the same devices between 4 V and 10 V.

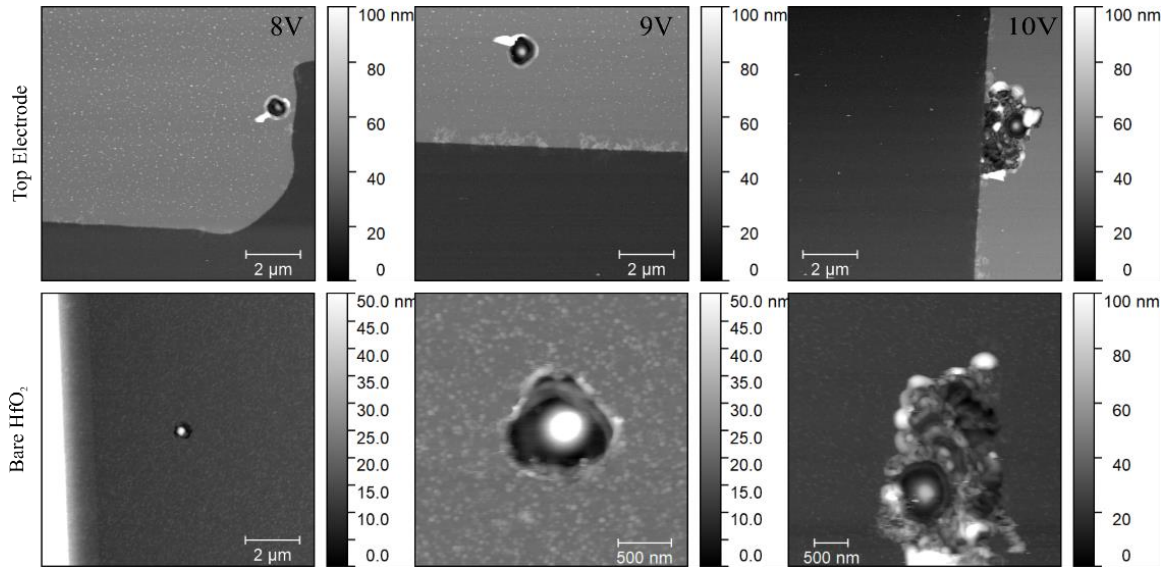

Figure B-5. AFM topographic characterization of devices based on 300 nm thick polycrystalline (250/000 ºC) HfO_2 with (Top) the top electrode retained as forming voltage is increased between 8 V and 10 V and (Bottom) with the top electrode removed for the same devices between 8 V and 10 V.

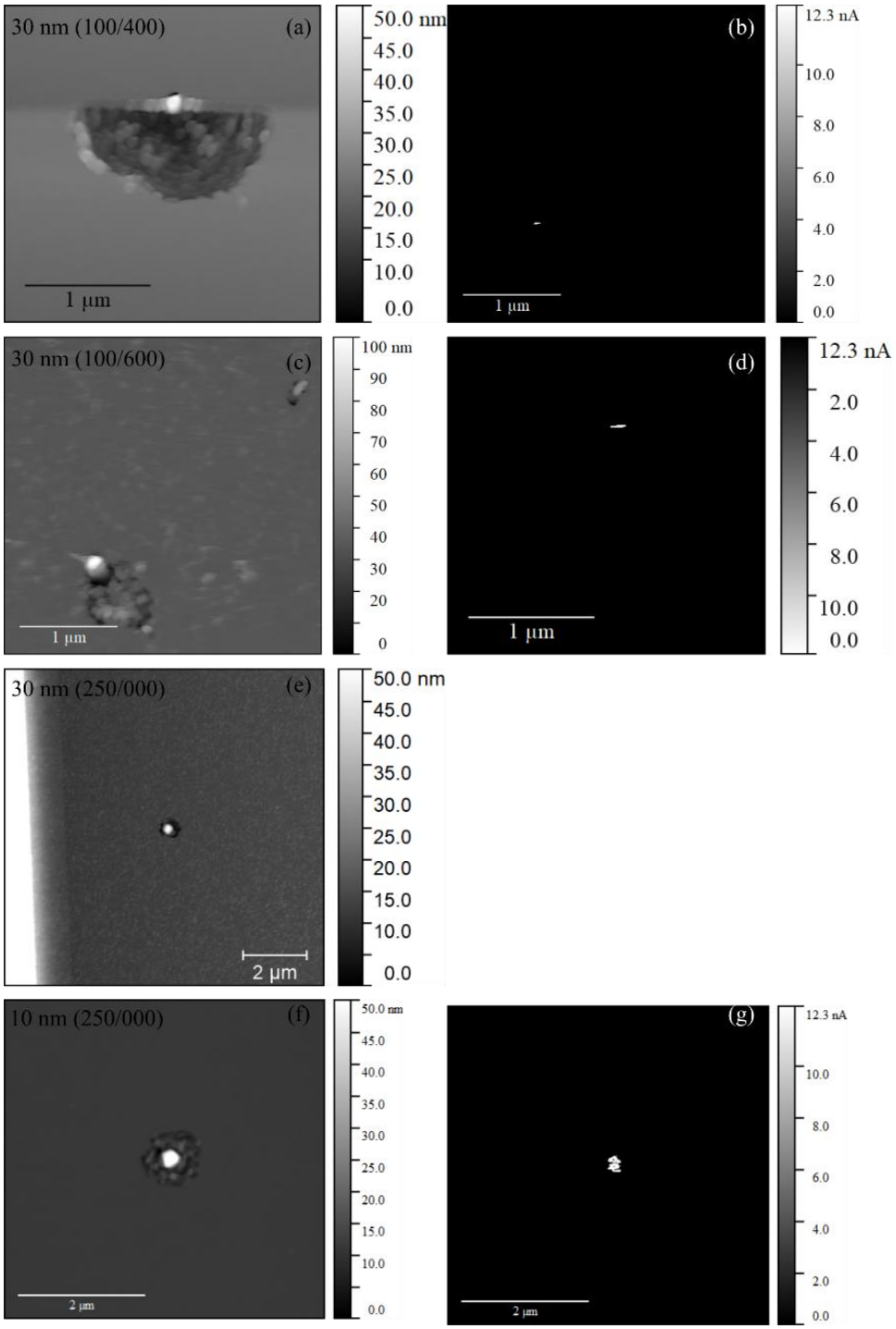

Figure B-5. AFM topographic characterization of devices based on 300 nm thick polycrystalline (250/000 ^{o}C) HfO_2 with (Top) the top electrode retained as forming voltage is increased between 8 V and 10 V and (Bottom) with the top electrode removed for the same devices between 8 V and 10 V.

APPENDIX C

SECTION 4 SUPPLEMENTARY FIGURES

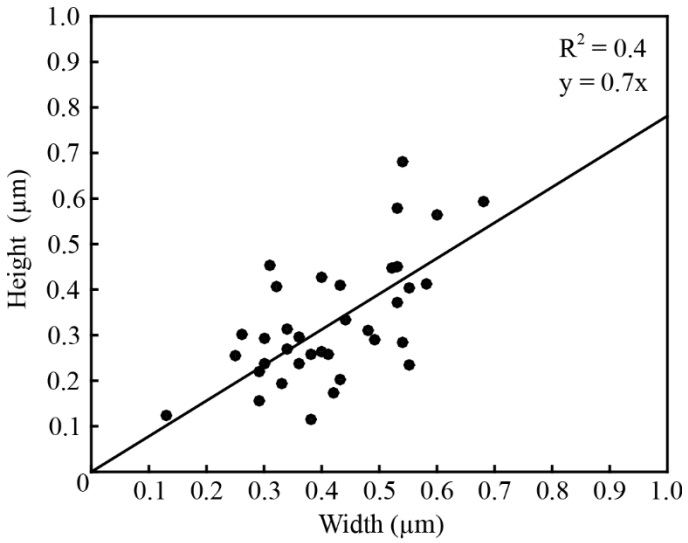

Figure C-1. Extracted particle height and width from AFM of several particles (N = 35).

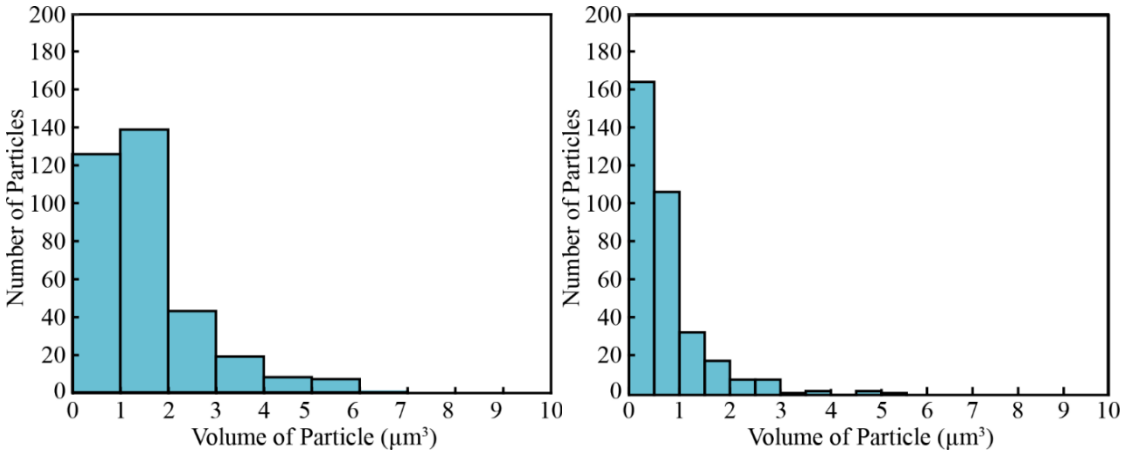

Figure C-2. Histogram of particle volume's measured by optical microscopy, binned by 1 μm^3 as used in data fitting using an estimated based (a) an average particle height of 0.8 μm, and (b) height calculated from the regression function y = 0.7x (Fig. S1).

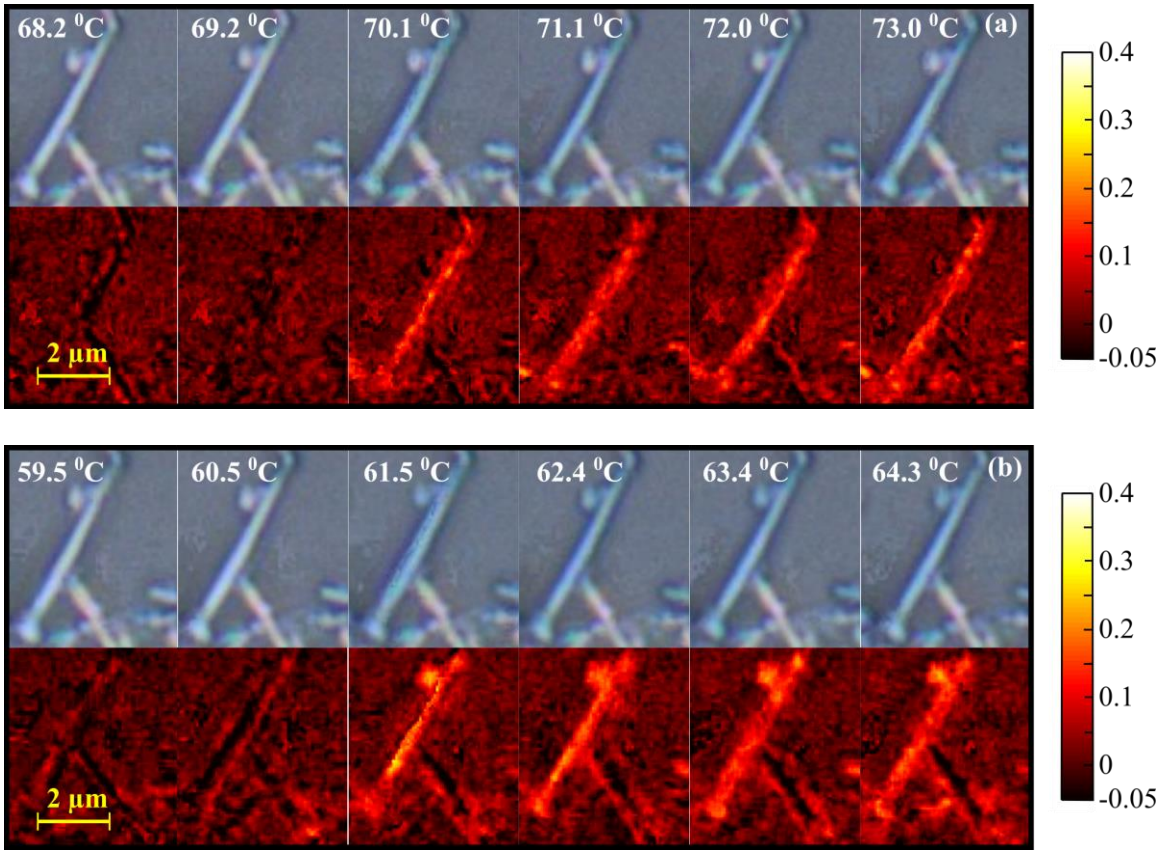

Figure C-3. Red difference plots of a single VO_2 wire showing a blue-shift upon undergoing the M1/R phase transformation upon (a) heating with a reference temperature of 63.4 ºC and (b) upon cooling with a reference temperature of 58.6 ºC.

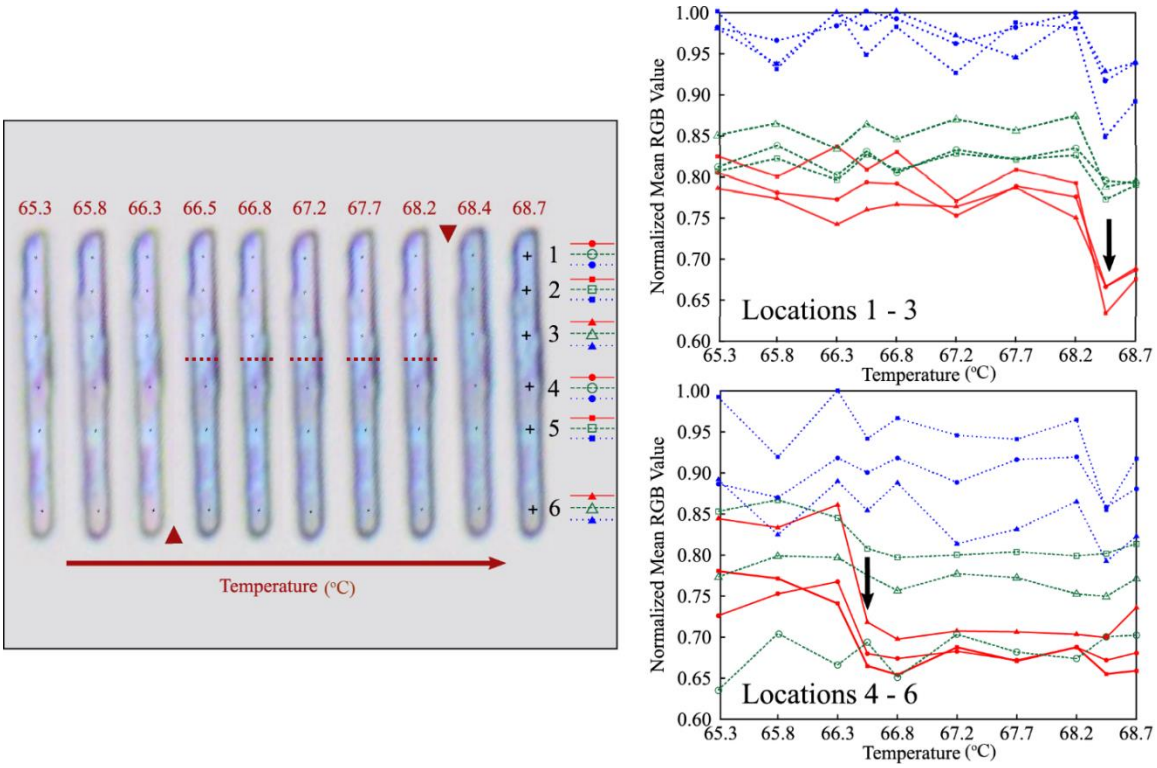

Figure C-4. Pixel RBG values for six locations marked by black crosses along a single particle (particle shown in Fig. 2) upon heating in 1 ^{o}C increments. Arrows indicate a dramatic blue-shift, due to a decrease in the intensity of the red component of reflected light, as indicated by red filled circles and red solid lines.

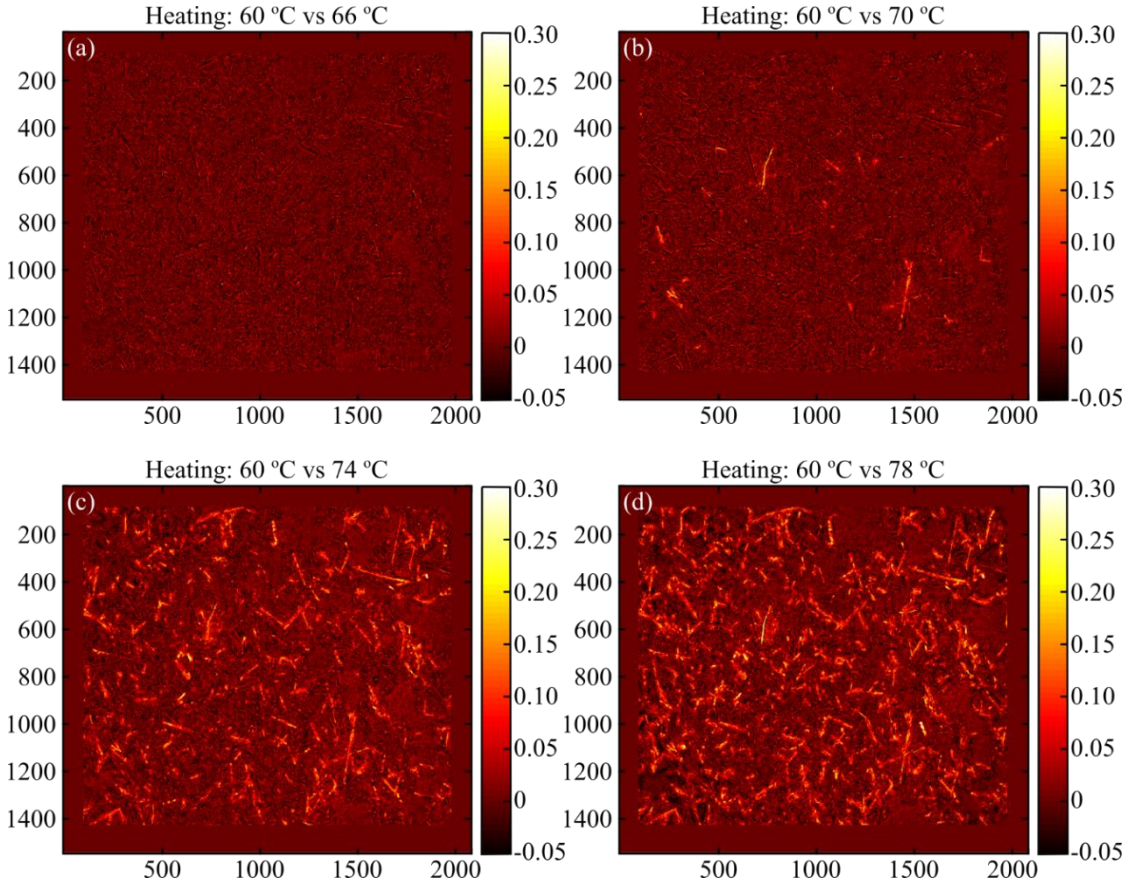

Figure C-5. Red value difference plots for undoped VO_2 from a single location imaged on a glass cover-slip on heating between 60 ºC (below T_{cr} = 68 ºC) and (a) 66 ºC, (b) 70 ºC, (c) 74 ºC, and (d) 78 ºC. Orange-yellow particles are clearly distinguishable from the background and are shown to have undergone a blue-shift in reflected light intensity and have transformed from the M1 to the R phase.

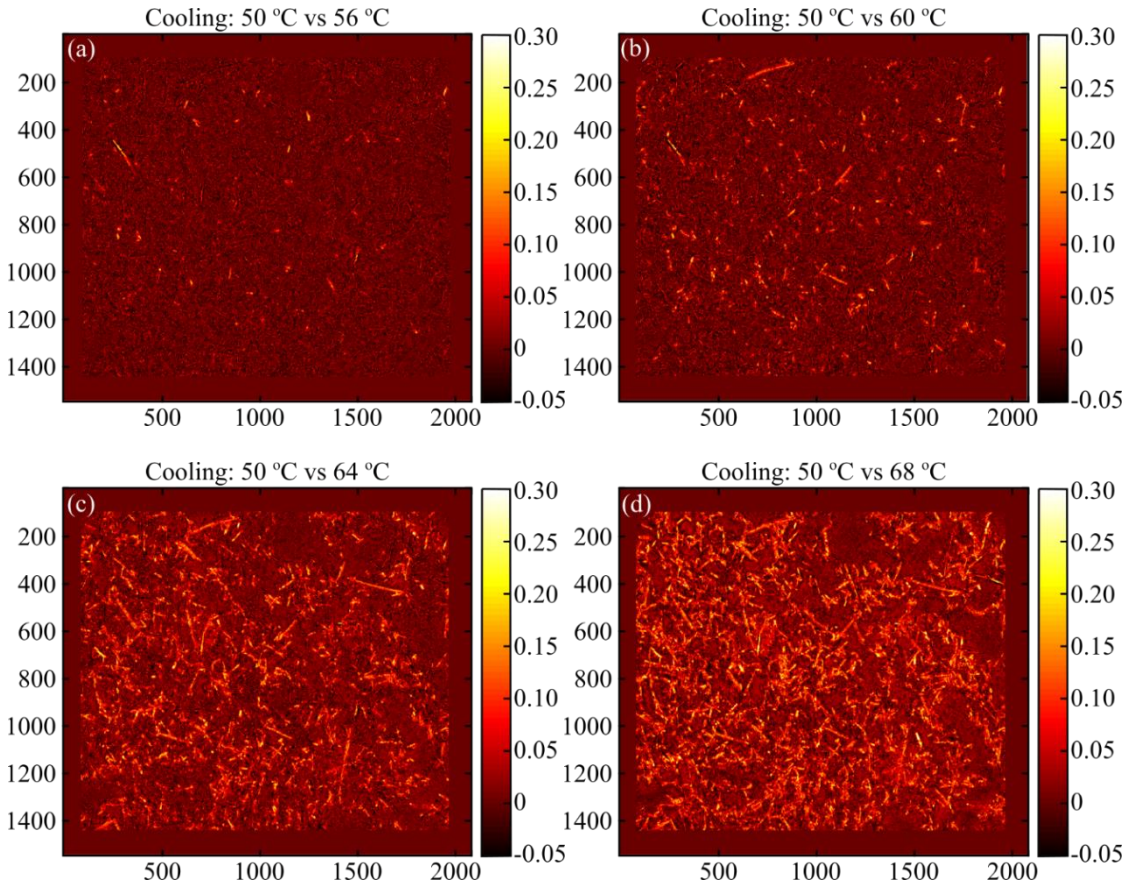

Figure C-6. Red value difference plots for undoped VO_2 from a single location imaged on a glass cover-slip on cooling between 50 ºC and (a) 56 ºC, (b) 60 ºC, (c) 64 ºC, and (d) 68 ºC. Orange-yellow particles are clearly distinguishable from the background and are shown to have undergone a blue-shift in reflected light intensity and are in the R phase.

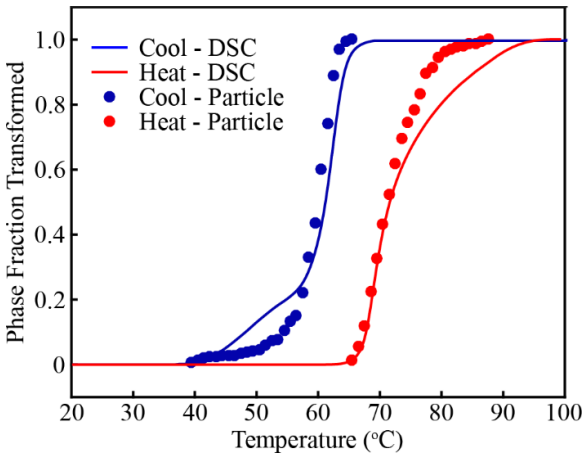

Figure C-7. Cumulative normalized fraction of particles (solid filled circles) transitioned and fraction transformed measured in the DSC at a rate of 1 °C/min upon heating (red solid lines) and cooling (blue solid lines).

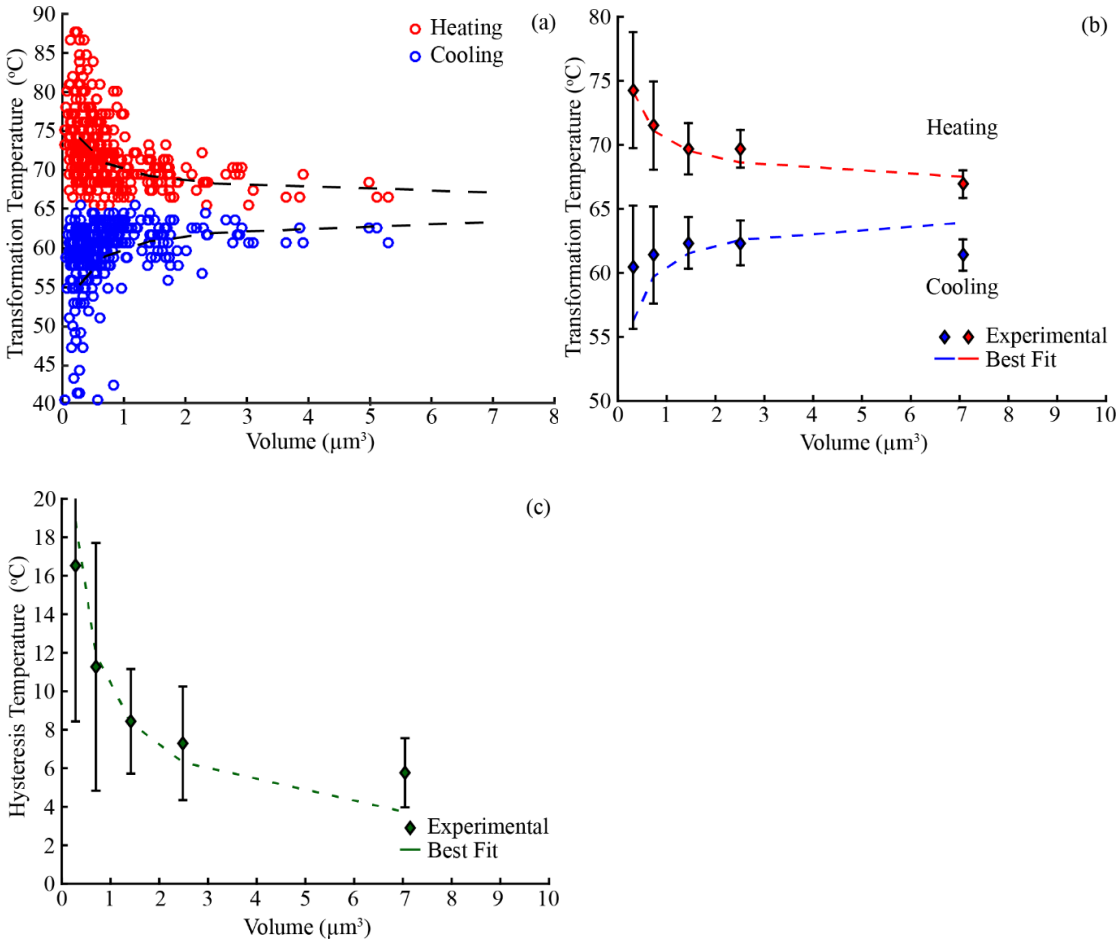

Figure C-8. (a) Transition temperatures on heating and cooling of individual particles as a function of estimated particle volume. (b) Median transition temperature on heating and cooling as a function of estimated particle volume showing best fit to the solution of F = 0.5 from Eq. 1, and (c) the calculated median hysteresis as a function of estimated particle volume with a best fit line to Eq. 1.

APPENDIX D

SECTION 5 SUPPLEMENTARY FIGURES

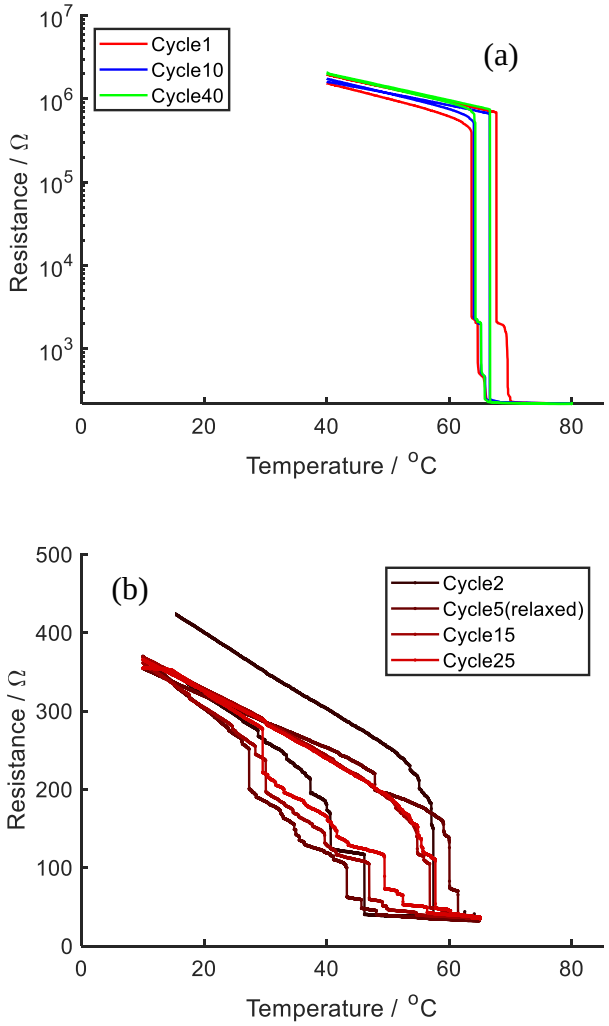

Figure D-1. (a) Several cycles of a single undoped VO_2 device showing the evolution of a two step transition to a single transition, and (b) several cycles of a $B_{0.01}VO_2$ device showing a greater degree of stochasticity among cycles.

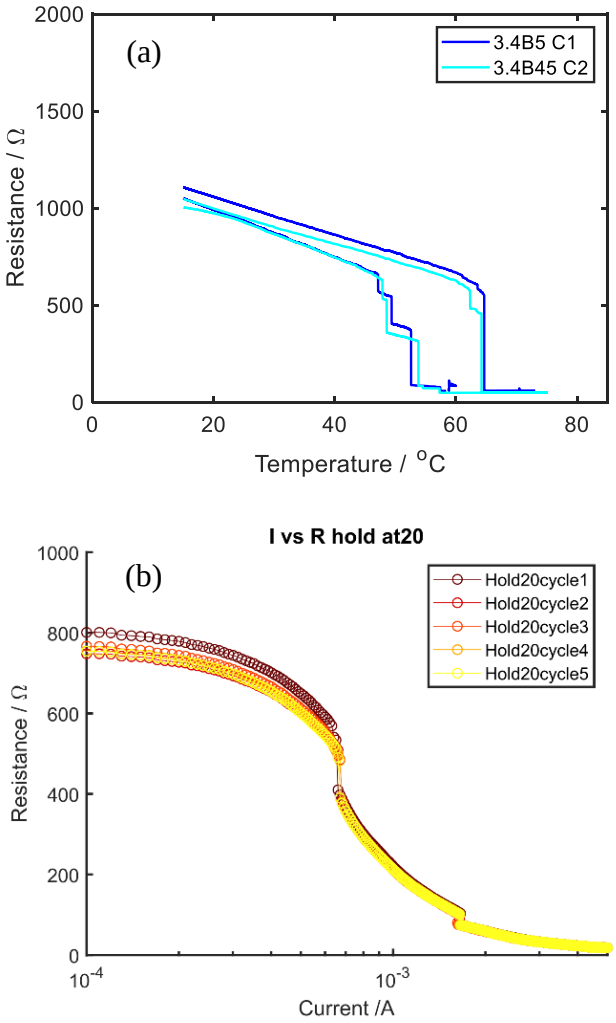

Figure D-2. (a) Two subsequent thermally driven cycles for a single $B_{0.01}VO_2$ device as compared with (b) five current driven cycles for the same device held at a base temperature of 20 °C.